POLITECNICO DI TORINO

DEPARTMENT OF APPLIED SCIENCES

AND TECHNOLOGY

Doctorate in electronic devices

(ciclo XXVII)

Nano-materials employment in energy harvesting and storage devices.

Scientific supervisor:

Dr. Daniele Pullini (Fiat research centre)

Academic advisor:

Prof. Giancarlo Cicero (Politecnico di Torino)

Candidate:

Dimitrios Tamvakos

Contents

Dedicated to my parents.

List of Figures

List of Tables

Abstract

The present thesis focuses on the development of a new generation of miniature electronic devices by employing nano-scale materials. Specifically, ZnO nanowire arrays were investigated to increase the conversion efficiency of energy harvesting devices and graphene nano-platelets employed to enhance supercapacitors' energy storage capability. The results obtained in this work pave the way to the possibility of conceiving novel autonomous devices integrating both energy units. The present thesis has been structured in five chapters.

A first introduction chapter reviews the *pros* and *cons* of renewable energies against the conventional ones produced from fossil fuels as well as their impact on the modern societies. The theoretical background on vibration energy harvesting and electrochemical energy storage is provided. Vibration energy harvesting mechanism relies on piezoelectric phenomena, where a pressure applied on a piezoelectric material turns ultimately into energy. Instead, supercapacitors store large quantity of energy for time unit by high surface material dielectric polarization. In this chapter, the reasons why ZnO nanowire arrays and graphene nano-platelets were considered are introduced.

The second chapter presents promising methods to synthesize piezoelectric ZnO nano-materials prior their integration into energy harvesting devices. Since the highest piezoelectric properties of the ZnO-crystal are along its c-axis, the most suitable growing methods were selected to tailor the crystal's unit-cell best orientation. In this chapter physical and chemical growing methods are reported. Physical vapor deposition (PVD) was used to grow ZnO thin film, then employed as a seed layer for the growth of 1D-ZnO nanowires by chemical methods in a second step. ZnO nanowires were synthesized either with or without a nanoporous template by: i) electrochemical deposition (ECD), and ii) hydrothermal technique. The fundamental process parameters to tailor the chemical growth are reported as well as the morphological and microstructural characterization of the structures fabricated.

In the third chapter, the characteristics of the energy harvesting device fabricated from the piezoelectric ZnO nanostructures are reported. Piezoresponse force microscopy was initially used to measure the d_{33} piezoelectric coefficient of the ZnO nanostructures fabricated fairly matching the theoretical expectations. Finally, this chapter reports the energy harvested by the devices fabricated, measured by connecting an external resistive load to it: a maximum energy harvested equal to 2 $\mu J/cm^2$ was found.

The fourth chapter focuses on nano-scale graphene based materials for supercapacitors' electrodes. Specifically, the synthesis and the characterization of the graphene nano-platelets used in this work is described. XRD and Raman spectroscopy were used to distinguish pure graphite from graphene, BET and SEM to measure its specific surface area and morphology. To determine the graphene's properties functional to the application thermogravimetric analysis (TGA) was carried out. To identify the types of oxygen groups present in the graphene materials, the corresponding Fourier Transform Infrared spectra (FTIR) were recorded and their contribution in rGO was examined by X-Ray photoelectron spectroscopy (XPS) analysis. Overall this

chapter reviews the relevant analysis to be performed in candidate materials for fabrication of supercapacitor electrodes.

The fifth chapter discusses the fabrication of supercapacitor electrodes made with the graphene nano-platelets previously described as well as the methods for their electrochemical characterization. As being the standard of the energy storage industry, cyclic voltammetry (CV) and constant current charge and discharge experiments were carried out for capacitance estimation. The electrochemical characteristics of the device were then linked to the properties of the graphene nano-materials employed. All measurements were done in a full-scale electrochemical cell mimicking a real supercapacitor device. The results suggest that mechanically exfoliated graphene nano-platelets (GNP) best perform among the variety of materials investigated.

Chapter 1

Energy harvesting and storage, background and motivation

1.1 Energy production and use

The forward technological passage over the last decades has created a massive increase in the available energy demand among societies. Our current standard of living is based on a colossal use of electrical energy, without of which the modern way of life would have been unconceivable. Fossil fuels are until nowadays the main energy provider [1], as shown in Figure 1.1 from Europe's gross inland consumption. Only from the beginning of the new millennium there has been an increase in the percentage use of alternative energies. Commission's ultimate goal, of deteriorating the fossil fuels dependence in energy production by 20% until the end of 2020 can be fulfilled by the shift towards the renewable energies.

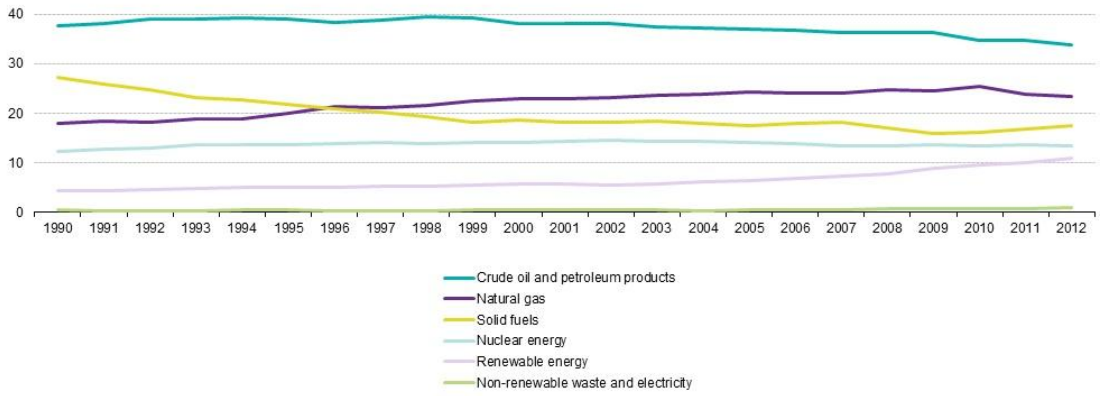

Figure 0.1 European gross inland energy consumption in % (1990-2012), Source: Eurostat.

Migration to renewable energies includes solar, wind and geothermal which are only few of the many possibilities towards fossil fuels reduction [2]. Other options include energy recovery which usually goes to waste like vibration and thermal [3]. Nevertheless being adequate numbered, these energy forms should be in immediate exploitation right after their generation. The previous factor deteriorates their use, due to their absence while needed. Besides, solar light is found only during the day and wind flow is not always present [4]. It is clearly understood that any kind of produced energy in order to be worthwhile should be stored properly

and being available for future utilization. The so called 'energy storage devices' address this specific need, allowing conservation, transformation and finally exploitation of the stored energy by the end user.

The aforementioned alternative energies' ultimate goal is the generation and production of electricity. Electrical energy is a good of utmost importance and its storage was found to be among the greatest technological interests over the last decades. In literature numerous concepts for efficient energy storage are reported. Namely, from the simple ones: Hydro-pump [5] and Compressed air [6], to the more technologically advanced like Hydrogen [7] and the Superconducting magnetic energy storage [8] all require the transformation of one amount of energy in electricity for the appropriate use. During that transformation, energy losses usually range from 5% to 35% or more depending on the method employed [5][6][7][8]. In this study, direct electrical energy harvesting is investigated and an alternative storage system is suggested.

1.2 ZnO in mechanical energy harvesting

Energy recovery from waste has received much attention over the last decades, towards efficiency advancement of electrical systems. As previously mentioned mechanical and thermal energies could be converted to electrical by means of piezoelectric and thermoelectric materials respectively. In the context of the present thesis the implementation of 1D ZnO nanostructures, named nanowires (NW) is studied for mechanical energy exploitation. ZnO is a direct wide band-gap, n-type semiconductor (~3.3 eV) material with large exciton binding energy. These properties turn ZnO to be promising candidate for numerous applications including sensing and actuation, optoelectronics, light-emitting diodes piezoelectric and pyroelectric devices [9].

ZnO's physical properties along with technological device miniaturization have shifted its nano-material synthesis to the forefront. A notable assortment of ZnO nanostructures has been reported to date, suitable for device applications. Nano-materials research relies on physical properties alteration by size and shape contraction. Habitually, nanostructured materials exhibit superior performances, desirable in modern electronic devices [10], compared to their bulk counterparts. ZnO with its wutzite (WZ) hexagonal crystal structure demonstrates excellent piezoelectric properties, possessing eminent electromechanical coupling [11].

Energy harvesters made by ZnO nanostructures are often found in the literature by the term 'nano-generators' which was firstly introduced by Prof. Z.L.Wang and his group who are among the first to studied the piezoelectric phenomena in ZnO nanostructures. The need of harvesting mechanical vibrations from the environment and convert them in electricity could be addressed by ZnO nano-generators. Typical uses of energy harvesting devices can be found on every industrial machine, where mechanical vibrations are present or even in bio implanted devices such as pacemakers and hearing aids as an alternative power source. They could be also used in powering wireless sensors/transmitters in areas inaccessible by cables (high temperature combustion chambers) or hazardous locations.

Within the literature two main competing topologies were proposed for energy harvesting and exploitation. The first one is called 'VING' (Figure 1.2) which stands for vertically intergraded nano-generator and the second 'LING' (Figure 1.3) for linearly integrated nano-generator. The VING configuration consists of numerous vertically aligned ZnO nanowires, grown on a conductive substrate. A resistive layer is usually added within the wires to enhance their mechanical support and prevent any short-circuit formation. A second metal electrode is then deposited on the top (Au or Pt) for circuit completion. Previous studies have shown that an applied stress of 6.25 MPa could generate a voltage of 90 mV [12]. Oppositely the LING configuration (Figure 1.3) was realized by photolithographically patterned stripes on Kapton films, within which, ZnO NWs were positioned. Flexing of the device by 0.19% was reported to produce 1.26 V of potential across its two ends. Although the voltage is larger, the authors calculated much smaller power densities in the LING compared to the VING configuration, promoting the use of the later as more promising candidate for energy harvesting applications. Apart from this use, ZnO NW based devices could be considered in strain and pressure sensing applications, humidity sensors [13], and gas sensors [14][15] (ethanol, carbon monoxide).

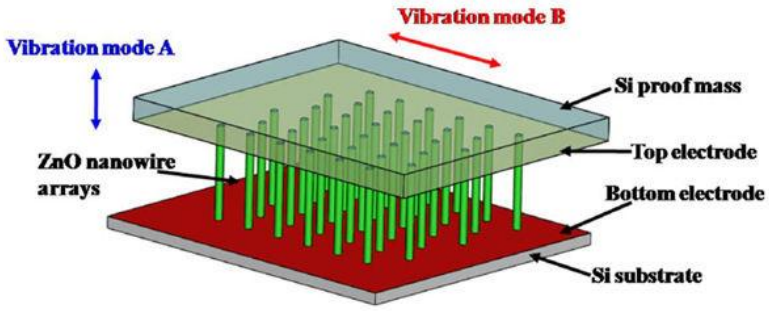

Figure 0.2 ***Vertically integrated ZnO based nano-generator*** **[16].**

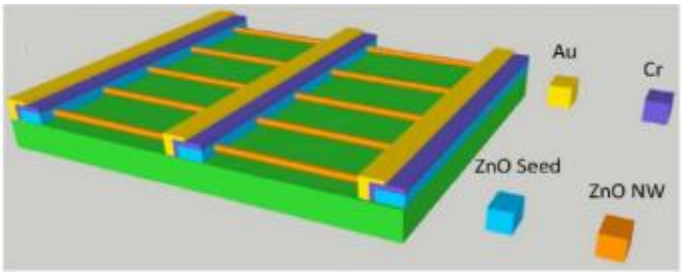

Figure 0.3 ***Linearly integrated ZnO based nano-generator*** **[17].**

1.3 Piezoelectric effect and ZnO

ZnO nanowire arrays' use in mechanical energy harvesting [18] has its origins in the direct piezoelectric effect, an intrinsic property of ZnO. The term 'piezoelectric' is derived from the Greek work 'piezo' which means to squeeze. From an external view point, an applied stress stimulates changes in the material's polarization according to the direction of its piezoelectric axes. The strength of piezoelectric polarization depends on the material's properties related to defects, oxygen vacancies and doping [19].

From a microstructural point of view, the essential condition for a material to be piezoelectric is not to possess a center of inversion symmetry. This means that its crystal structure should not be symmetric when reflected across the center of the unit cell, normal to the direction of applied stress. Internally, when a piezoelectric material is deformed, an electric dipole is formed within the unit cell. Macroscopically, this results in an electric field generation along the piezoelectric layer. In Figure 1.4, a quartz unit crystal is shown exhibiting its polarization under different stresses.

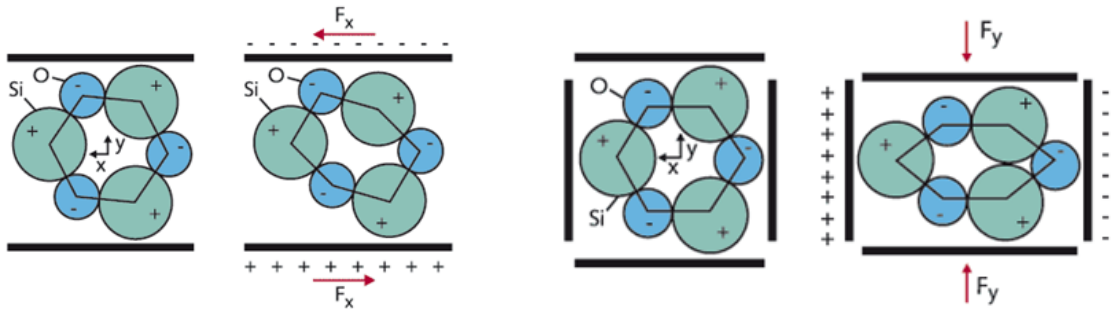

Figure 0.4 ***Dipole formation mechanism due to piezoelectric effect in quartz crystal.***

In the neutral case, when the unit cell remains unstrained both positive and negative atoms are balanced and no dipole formation is observed. However in the case of y-axis compression or shear stress implementation the atoms are displaced from their neutral position, allowing net dipole creation. In piezoelectric materials, these dipole moments are positioned accordingly and lead to the overall polarization of the piezoelectric crystal. Quartz was the earliest piezoelectric material to be discovered and is widely used in piezoelectric devices because it's particularly amenable. It can responsive to compression, tension, and shear stresses, depending on how the crystal is cut, permit the tuning of the angle between the applied mechanical stress and the direction of the dipole formed. The previously described mechanism takes place in all piezoelectric materials (case for ZnO as well), while the polarization magnitude and direction depends on their own intrinsic properties.

The piezoelectric effect is divided in two operating modes. The direct piezoelectric effect refers to the case when a mechanical work is employed to deform and polarize the material, while the converse

piezoelectric effect performs exactly in the opposite way. In the later mode, an external electrical field is used in order to polarize and finally deform the material. The former two piezoelectric modes are described by the Eq.1.1 for inverse and Eq.1.2 for direct piezoelectric effects respectively.

$$\mathbf{S} = \mathbf{s^E T} + \mathbf{d^t E} \quad [1.1]$$

$$\mathbf{D} = \mathbf{dT} + \boldsymbol{\varepsilon}^{\mathbf{T}}\mathbf{E} \quad [1.2]$$

Where S is the strain vector, s^E is the compliance matrix at constant or zero electric field, T is the stress matrix, d^t is the transposed piezoelectric coefficient matrix, E is the electric field matrix, D is the electric displacement vector and ε^T is the dielectric permittivity matrix at constant or zero stress. The set of [1.1] and [1.2] is used to describe the piezoelectric phenomena and is usually found as strain-charge equation forms since they relate these two physical terms.

The magnitude of a material's piezoelectricity is described by the piezoelectric coefficient d. This is a material-dependent constant which relates either the charge generated to the force applied (Coulombs per Newton) or the amount of displacement in response to an applied voltage (meters per Volt). Since the piezoelectric effect depends on the material's crystal structure, it is highly anisotropic. The constitutive equations are therefore expressed in tensor notation, with the matrix elements of each term representing different directions. For example, d is commonly written as dij, where i is the direction of electric displacement and j the direction of applied stress. Consequently the previous two equations are more often encountered in a matrix form, shown in [1.3] and [1.4].

$$\{\mathbf{S}\} = [\mathbf{s^E}]\{\mathbf{T}\} + [\mathbf{d^t}]\{\mathbf{E}\} \quad [1.3]$$

$$\{\mathbf{D}\} = [\mathbf{d}]\{\mathbf{T}\} + [\boldsymbol{\varepsilon}^{\mathbf{T}}]\{\mathbf{E}\} \quad [1.4]$$

1.4 Electrical energy storage

In electrical energy storage there are found two fundamentally different concepts and their main representatives are batteries and capacitors [20].

- Batteries store electrical energy in an indirect way, as potentially available chemical energy requiring Faradaic oxidation and reduction of the electrochemically active reagents in order to release charges that perform electrical work when they flow between two electrodes possessing different potentials.
- Capacitors store the electrical energy in an electrostatic way as positive and negative electric charges on their two parallel plates. This process, in contrast with the previous one, does not involve any chemical reaction during their operation. In this category, Supercapacitor is a specific type of capacitor which exhibits considerably higher capacitance properties than a normal capacitor does (typically 10^6 times higher). In literature, supercapacitors are also found as ultracapacitors or electrochemical capacitors (EC) as well.

Storage systems like batteries and capacitors have the advantage of eliminating the need for energy transformation from its initial form to electricity, as happens with the systems mentioned before (page 5). Thus, offering increased efficiencies and performances. Both these main competitors belong to the category of electrochemical energy storage devices. An insight between their perspective performances is given by the Ragone plot which demonstrates the specific energy density (Wh/Kg) versus the specific power density (W/Kg) in such kind of devices. A comparison between electrochemical capacitors (EC) or supercapacitors as they are often found and Li-ion batteries (standard technology) is shown in Figure 1.5 [21].

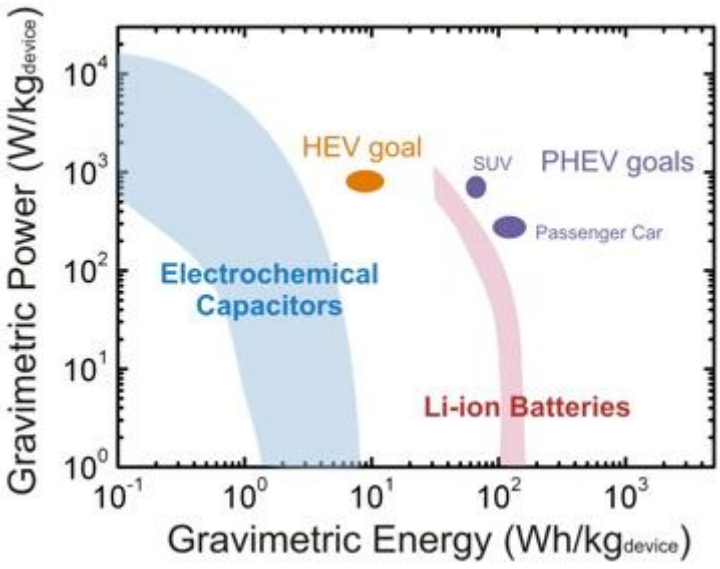

Figure 0.5 ***Energy vs. Power densities represented in Ragone plots for EC capacitors and batteries. Basic automotive industry needs are depicted in purple. Reprinted from*** **[21].**

Nowadays, batteries are the most popular choice for high portable energy storage applications. From Figure 1.5 the reason is straightforwardly understood, as Li-ion batteries demonstrate considerably high specific energy densities, which are needed in most commercial applications. However, the Faradaic storage mechanism includes chemical reactions which come along with irreversible phase changes of the electrode

materials during the charge and discharge cycle that limits their life expectancy. The appropriate time needed for these reactions to occur deteriorates batteries use in high power applications where fast charge and discharge (phase changes) is needed. On the other hand supercapacitors do not retain so high energy densities, but are capable of exhibiting much better power densities compared to batteries. Typically their power density ranges from 0.5 to 20 KW/Kg and their energy density from 15 to 80 Wh/Kg. The operation of charge and discharge in a supercapacitor is quite fast. Oppositely to batteries, it involves only the movement of the carriers in the electrolyte [20]. This allows their use for numerous cycles, without significant degradation of their performance. A commercial supercapacitor usually arrives to 10^6 cycles of deep charge and discharge (CD).

In order to level differences in power and energy densities between them and expand their use for future applications, hybrid systems consisting of batteries and supercapacitors, which function in a synergic way, have been proposed [22]. Another approach for the previous scope lies on novel types of materials used in supercapacitors. Innovative nano-materials research like graphene is expected to lead the way towards supercapacitor devices of higher energy densities.

The scope of the present thesis is the investigation of novel nano-based materials as EC electrodes, which can render devices of high energy densities conceivable. Prior to that, a background on supercapacitor types and operating principles is reviewed. Furthermore, electrochemical techniques along with the appropriate cell construction used for capacitance, energy and power density determination are discussed.

1.5 Supercapacitors

The story of supercapacitors dates back to 1957 [23] when General Electric patented a device, in the form of a capacitor, which had the ability to develop a capacitive charge at the interface between an electrode and an electrolyte. That electrostatic charge mechanism was described by the Electrochemical double-layer capacitance (EDLC) [24] and the device was employing porous carbon as electrodes and sulfuric acid as electrolyte. Supercapacitors have been used as energy storage devices since mid-seventies. Their potential applications can be anticipated from the large number of companies activated in the field [25]. Later, in the same decade a new type of supercapacitor was proposed by Conway. In that approach apart from EDLC there was inserted a pseudo-capacitance element. This addition turns the transferred charge to be voltage dependent because the electrode/electrolyte interaction faradaic reactions which are activated at specific potential values [26]. Although pseudo-capacitance tends to increase the overall device's capacitance properties, it frequently suffers a similar instability and life cycle drop as the one mentioned for batteries.

Supercapacitors consist of a two electrodes immersed in an electrolyte (aqueous or organic based) with a separator membrane placed between them. The electrodes are fabricated by materials possessing relatively high surface areas. Usually porous materials, having pores in the micro/nano-meter range are employed for the scope. In this way their surface areas can easily range from 500 to 2000 m^2/g. The charge is stored electrostatically, on the surface of these nanoscale pores at electrode/electrolyte interface. Figure 1.6 shows in micro-scale the layout of a supercapacitor, whose electrodes are made by activated carbons.

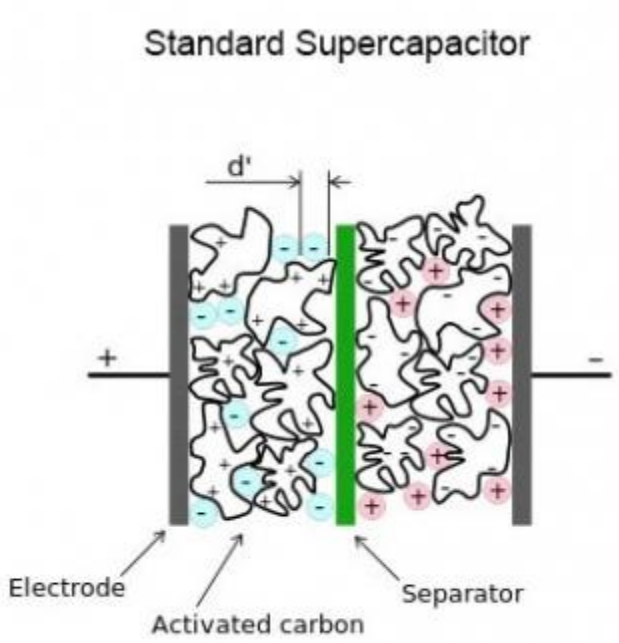

Figure 0.6 ***Micro-scale representation of an activated carbon supercapacitor (source Maxwell technologies).***

The capacitance value of an ultracapacitor is given by Eq. 1.5. As in the case of a dielectric capacitor, it depends on the dielectric constant (K), the thickness of the dielectric material (th) and its area (A). Even if the formula is known, the determination of the dielectric constant k and the thickness of the double layer are quite a complex task [27]. The energy stored in the capacitor is given by Eq. 1.6.

$$C = KA/th \quad [1.5]$$

$$E = \frac{1}{2}CV^2 \quad [1.6]$$

The capacitance of the final device depends mainly on the characteristics of the electrode material as well as the used electrolyte. Characteristics of the electrodes include the surface area and the conductivity. The surface area is referred to the active area inside the pores, where the double layer is formed, while the conductivity determines the ability of the electrodes to attract the electrolyte's ions for the double layer formation. The thickness of this double layer is fairly small (less than some nm), which results in extraordinary capacitance values [28] (Eq. 1.5). Often, for research comparison purposes instead of capacitance it is demonstrated the gravimetric specific capacitance, which is the fraction of its absolute value (F) with the overall mass, involved (grams). Stated in this way, common specific capacitance values range from 150 to 200

F/g for an electrode material with specific surface of 1000 m^2/g. However the measured capacitance for materials being used in actual devices is less than that because for most carbon materials a relatively large portion of the surface area is found in non-accessible pores from the electrolyte.

The voltage limit, at which a supercapacitor operates, depends mainly on the electrolyte employed. Typically, aqueous solutions offer potentials of about 1 V, organic solutions range from 2.5-2.7V [29] and ionic liquids can reach even more, 3 to 3.5V [30]. As seen from Eq. 1.6 the energy stored in a capacitor increases with the square of the voltage which explains why the majority of commercial EC so far make use of organic based electrolytes.

1.6 Types of supercapacitors

1.6.1 Electric Double-Layer Capacitors (EDLC)

As mentioned earlier, this category contains the devices on which the charge storage mechanism is described electrostatically. More specifically, the charge is stored in the capacitor by means of an electrochemical double layer. The double layer is formed at the interface between the electrode and the electrolyte. An external applied potential on the device, guides the accumulation and the depletion of electrons across its two edges. The freely moving ions inside the electrolyte solution are positioned accordingly close to electrodes' surface in order to screen the accumulated charge as seen in Figure 1.6. This process forms an electrical double layer of positive and negative charges, which in theory remains electrostatic. The 'double' term comes from the creation of two layers, each one on the surface of each electrode. The main factors determining the EDLC creation are:

- Electrodes possessing large surface areas, which lead to bigger interaction with the electrolyte. A bigger active area allows more ions to participate in the charge storage mechanism, exhibiting larger capacitance.
- Fairly good electrical conductivity is needed in order for the power losses to be reduced. Caution on designing an electrode is needed as the porous like structure is keen on increasing the overall resistance of a material.
- Electrolyte's ion size should be matched with individual pore size from the electrodes, allowing the highest possible ion diffusion.
- Surface wettability could enhance the pore flooding, which indicates higher surface area utilization.

In current commercial ECs carbon based materials are used for electrical double layer charging and discharging similar to that of dielectric capacitors. The main reasons are its accessibility, low cost and easy process-ability [31]. The properties of carbon materials are strongly affected by the preparation method [32]. The most popular electrode material is activated carbon (AC), which stands for carbon having followed a thermal treatment (2500 ^{0}C) in a controlled gas atmosphere (N_2). Despite activated

carbon's benefits, technological advancements are focused in the development of novel materials to deliver higher amounts of power and energy. A noticeable number of nano-structured materials have been proposed for the scope. The most noteworthy of them are carbon nanotubes (CNTs) [33] and graphene [29].

1.6.2 Pseudo-capacitors

In this type of capacitors, faradaic reactions take place during the cycling operation. As mentioned in the previous section in EDLC the capacitance remains constant and is independent of the voltage. In the case of pseudo-capacitor the interaction between the solid electrode and the electrolyte involves a faradaic reaction additionally to EDLC formation. In this case the charge being transferred is voltage dependent. The concept of pseudo-capacitance is better envisioned in Figure 1.7 [34]. As can be seen, for an ideal EDLC a perfect rectangle expresses its charge and discharge characteristics. However, electrode materials with pseudo-capacitive behavior deviate a lot from the rectangular shape. They exhibit redox peaks which are connected with the faradaic reactions involved (Fig. 1.7, line 4). An important point in the graph is the delay in the potential's phase change during the reversing of the current, connected to kinetically slow charging processes.

Even if the specific capacity of pseudo-capacitors surpasses the one of the carbon based EDLCs, their commercial development was not so rapid. It is addressed to the inferior charge and discharge characteristics as well as the cycle lifetime than those of EDLC. Apart from that, their operating voltage is often lower than EDLCs, so as the stored energy Eq. 1.6. Pseudo-capacitors involve three main types of physical processes.

I. Surface adsorption of ions from the electrolyte to the electrode.
II. Redox reactions involving ions from the electrolyte and the electrode.
III. Doping and un-doping of active conducting polymer material in the electrode.

A large variety of materials have been reported for pseudo-capacitor operation, with more popular the use of 'oxides'. Namely, IrO_2, SnO_2, and MnO_2 are the more frequently found [35]. MnO_2 has proven to be the most promising candidate among them, to be used as electrode, offering specific capacitances in the range of 450 F/g [36]. Albeit ruthenium and tantalum oxides (RuO2, Ta_2O_5) can deliver really high capacitance values close to 900 F/g [35], their use though is inhibited due to their cost and toxic impact to the environment.

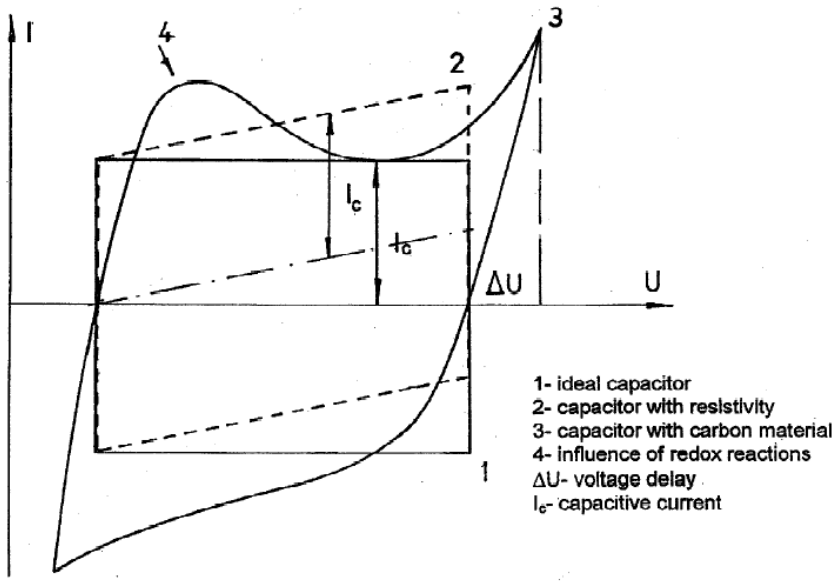

Figure 0.7 ***Theoretical cyclic voltammetry characteristics in various capacitor types.***

1.6.3 Asymmetric or hybrid capacitors

The last category of supercapacitor devices owes its name to the asymmetric fabrication of the two electrodes used in the cell. Literally, one electrode is made of materials offering the double layer effect (carbon), while the second being of pseudo-capacitive or faradaic or battery type materials. In terms of capacitive storage, these devices exhibit a combination of the advantages offered by EDLCs and batteries. Their charge/discharge characteristics depend on the thickness of the positive (battery type) electrodes. An increase in electrode's thickness leads to a shift from capacitive-like to battery-like performance [37]. A suitable engineering design for a hybrid capacitor, as well as an appropriate selection of electrode materials is favorable to lead at really high capacitance values.

1.7 Conclusion

This chapter is an introduction to the research study performed in this thesis. Energy harvesting from waste represents one of the main challenges in green energy research. Undoubtedly among the most prominent ways of harvesting energy from the ambient are found solar and thermal energies. However, here it is proposed an emerging technology that can be used in converting vibrational mechanical energy to electricity. The abovementioned transformation is done by means of piezoelectric materials. In the first part of the present study ZnO nano-structured materials are investigated for their piezoelectric properties and evaluation of their use in miniaturized energy harvesting devices.

An energy harvesting system is usually employed in two cases. The first includes the energy supply to the power grid while the second requires the use of the produced energy in standalone systems. From the second case it is conceivable that an energy harvester cannot be used by itself if not accompanied by a storage system where the energy could be stored for future use. The second part of this research is attributed to a recent concept of energy storage by means of electrochemical supercapacitors. The devices reviewed in the present study store the charge by an electrochemical double layer formation.

EDLC use mainly carbon based electrodes; however by the emergence of graphene many researchers have suggested this material as possible substitution of current technology. Graphene was proposed, as it both fulfills two of the basic demands for a supercapacitor electrode. It has one of the highest surface area densities (2600 m^2/g) and in the same time offers elevated conductivities (10^6 S/cm) due to its sp^2 conjugated network. For evaluating the performance of graphene based materials when used in supercapacitors, thick electrodes have been prepared following the standard industrial procedures. Electrochemical storage measurements like cyclic voltammetry and charge and discharge, as well as material analysis revealed their performance when used for the aforementioned scope.

Chapter 2

ZnO nanostructures for mechanical energy harvesting

In the context of the present thesis, ZnO was employed in mechanical to electrical energy conversion. The major property offered by ZnO with respect to the abovementioned application is the piezoelectricity. Although ZnO is a well-known piezoelectric material in bulk shape, exhibiting piezoelectric coefficients that range from 9.9 pC/N to 12.4 pC/N, the scientific interest combined with the miniaturization of electronics was shifted in implementing its nanostructures in devices for the aforementioned scope. In the present chapter there are reviewed the relevant physical and chemical methods studied in order to synthesize ZnO nanostructured materials. At the chapter's opening it is presented ZnO's unit cell, which acts as the fundamental building block for further growth. The piezoelectric properties of the whole crystal strictly depend on the crystal's growth direction. From theoretical point of view, it is well known that ZnO offers its piezoelectric properties along its c-axis. According to these criteria, the most suitable growing methods will be selected for further piezoelectric experiments. In the search of the most efficient c-axis growth technique, physical vapor deposition (PVD) for ZnO thin films, electrochemical deposition and hydrothermal growth for 1D ZnO nanowires were introduced. The most promising result regarding the growth was acquired by the chemical growth techniques, rather than physical. The nanowires (1D) came from the electrochemical growth experiments were further used to precisely quantify the d_{33} piezoelectric coefficient (with PFM) since they exhibit the highest c-axis orientation in combination with vertical growth. The hydrothermal nanowires were used to fabricate piezoelectric energy harvesters. However exhibiting lower degree of verticality (important factor for piezoelectric applications) compared with the electrochemical ones, their relatively facile handling and preparation make them more suitable in fabrication of large scale devices. Additionally to free standing 1D nanowires template approaches were inserted in an attempt to precisely control the crystal dimensions. Although leading to successful growth, problems related to the membrane dissolution were inhibiting the use of this method for further experimentation.

2.1 Zinc Oxide nano-structures

Zinc Oxide is a wide band gap semiconductor of (~3.3 eV), exhibiting Wurtzite crystal structure of hexagonal shape (also crystalizes in zincblende, more unstable form). Its crystal is composed of alternating zinc and oxygen planes, forming the final ZnO structure. The key prerequisite for any crystal to be piezoelectric is not to express crystal inversion symmetry in its unit cell. ZnO's piezoelectric as well as pyroelectric properties, both origin from its unit cell's non crystal inversion symmetry. In Figure 2.1 it is shown the wurtzite crystal

structure of ZnO. ZnO's basal plane (0001) is a polar surface, which is terminated at one end by positively charged zinc ions and at the other end by negatively charged oxygen ions. The rest of the crystal surfaces, shown in the left side of Fig. 2.1 are non-polar.

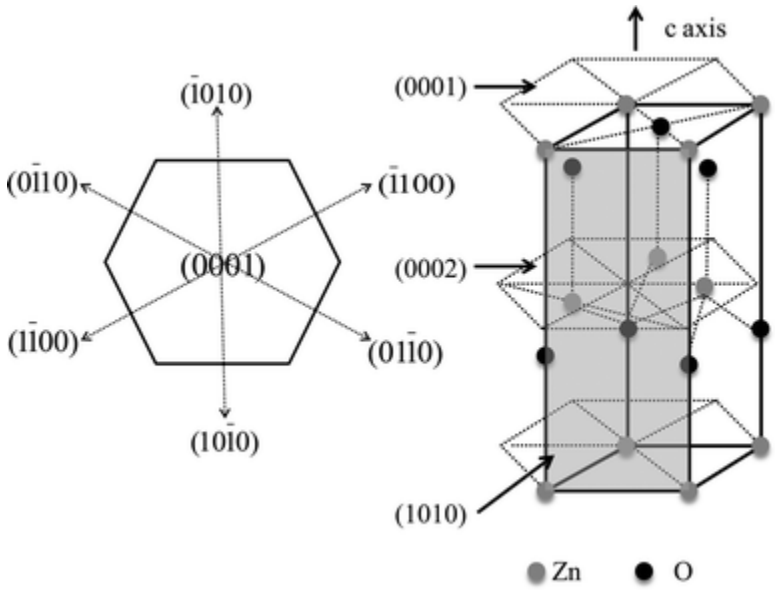

Figure 0.1 ***Wurtzite crystal structure of ZnO unit cell*** **[38].**

As mentioned in the introduction, the miniaturization of modern electronics, as well as the low power consumption needs, has paved the way of implementing nanostructrured materials for fabrication of novel devices. In literature a great variety of ZnO nanostructures can be found including nanowires (NW) [39], nanorods (NR) [40], nano-flowers [41] and nanobelts [42]. The discrepancies in the shape of these structures are dictated by the different growth rates along different crystal planes. Addition of catalysts or rate inhibitors during the growth process could take place in order to further control the growth ratio between different crystal planes. In the general case, a crystal forms its structure in such a way as to maximize the surface area of low energy surfaces, as the non-polar surfaces. As understood from Fig. 2.1, the side walls geometry of ZnO (non-polar phases) is maximized, while the polar ends follow a rapid grow at (0001) direction. Consecutively, the nanowire form is the most favored one for ZnO when stating self-assembly nano-structure synthesis.

The forms of ZnO nano-structures developed in the present thesis are:

- Thin Films by Physical Vapor Deposition (PVD).
- Nanowires/Nanorods by Electrochemical deposition.
- Nanowires by Hydrothermal growth.

The growth of ZnO nano-structures (PVD and electrochemical deposition) in CRF's labs has started in 2009 from Dr. Pruna. The present work is a passage from her initial contribution of the bare ZnO nano-material to its proper use as a functional building block in energy harvesting devices.

2.2 ZnO Thin films by RF magnetron sputtering

Till date, a wide variety of deposition techniques for ZnO thin films have been reported [43]. In general, RF magnetron sputtering yields the best piezoelectric [44] layers, as it offers highly oriented and dense layer growth. Sputtered ZnO films are regarded as one of the most useful, eco-friendly piezoelectric thin film materials [45]. Sputtered ZnO films are mainly polycrystalline, and their individual crystals grow in different orientations.

The ZnO film growth in this study was performed by a RF magnetron sputtering (Edwards Auto 306). Sputtering is a physical process whereby atoms from a solid target are ejected into the gas phase, due to material bombardment with energetic ions (Figure 2.2). The following phase includes the deposition of these particles on the surface of a substrate, which finally leads to a whole substrate covering with the desired material. This procedure is commonly used for thin-film deposition and functional coatings as well as integrated circuit processing. The outcome of this process is a new film containing several layers of the target, like metals or metal oxides such as zinc oxide, tin oxide, or titanium dioxide.

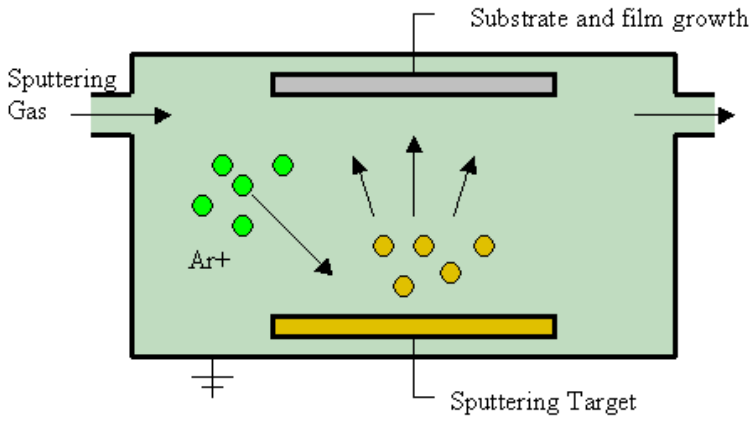

Figure 0.2 ***Schematic representation of RF magnetron sputtering working principle.***

According to sputtering deposition, the formation of thin films takes place in two different stages, the initial (nucleation and coalescence), and the final (actual growth) stage. As initial stage, it is considered the period from the beginning of the sputtering till the moment the first ZnO cell has been formed on the substrate. The most important parameters during initial growth are the chemical and physical properties of the substrate, and the interaction between substrate and the arriving particles. Once the initial stage is over, actual growth begins, during which interaction only occurs between the particles of the sputtered material. The parameters to determine the shape, the geometry and the texture of the film are the energy of the particles

arriving at film's surface, energy absorption at the time of collision, and chemical and physical interactions between adatoms and the substrate-film surface as well as its temperature.

A detailed growth model for metal oxide thin films formation by RF sputtering has been proposed by Movchan and Demchichin [46], which was later extended by Thornton [47]. As shown in Figure 2.3, the film is divided in four different zones. Zone 1 allows the formation of rough surfaces due to low adatom mobility (slow surface diffusion) and the "shadow effect". Passing to zone 2 the adatom mobility increases, and finally overcomes the shadow effect in order to grow dense layers with more columnar grains. Finally, in zone 3 small grains coalescence to form larger, not necessarily columnar. The last zone is called T zone, where grain outlines are difficult to be identified. ZnO sputtering procedure is shown in the next figure.

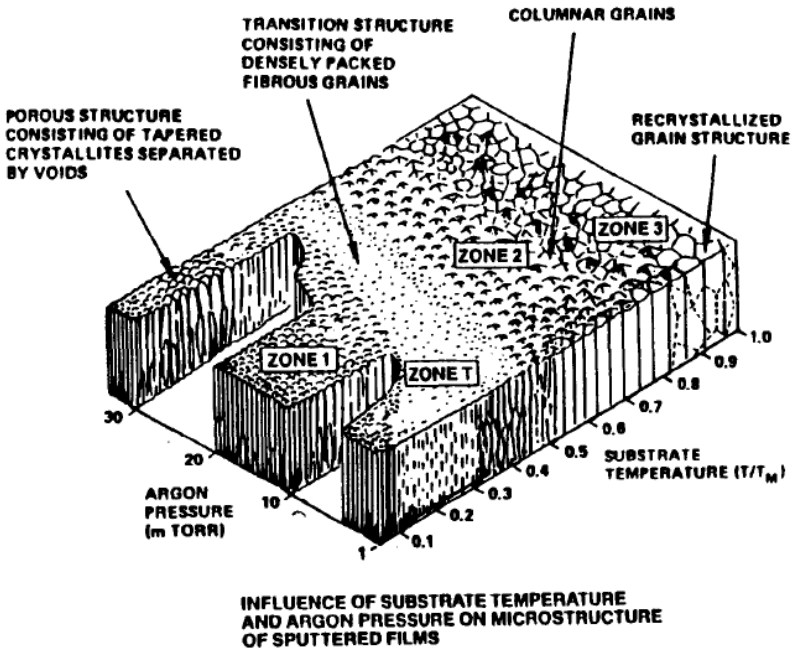

Figure 0.3 ***Synthesis model for thin films growth, by RF magnetron sputtering*** **[47].**

ZnO films were prepared by RF sputtering in the following layout as shown in Figure 2.4. The target used for this scope, is a 2 inches diameter ZnO target of 99.99% pure (2" diameter x. 250" thickness) which was set at 9 cm apart from the chosen substrate. High purity Argon gas (Ar) was introduced in the vacuum chamber at 2x10-6 Torr. The deposition is performed at various sputtering powers and different deposition times, typically from 70W to 150W and from 18 to 50 minutes respectively. The final film thickness depends on the appropriate selection of the previous two parameters.

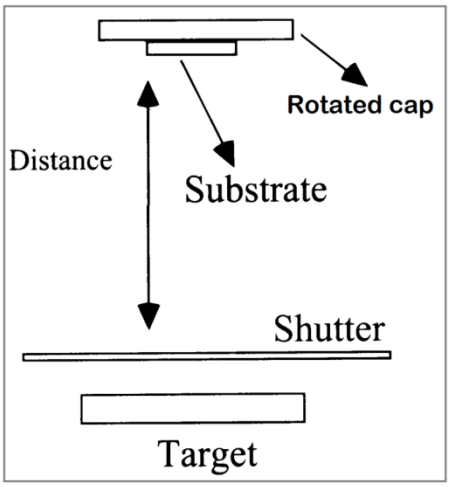

Figure 0.4 ***Common setup of the sputtering process inside the vacuum chamber. The target to substrate distance was selected to favor uniform film formation.***

Morphological and structural analysis was performed in order to characterize the ZnO thin films. The morphological analysis was done by Atomic Force Microscope measurements (Dimention 3100 AFM) and the structural analysis by X-Ray diffraction (XRD). Scanning Electron Microscopy (SEM) measurements have been carried out as well but gave insufficient information about the surface structure.

In order to investigate the influence of the sputtering power to the final material, two differently grown ZnO films (200nm thickness) were analysed by XRD and are depicted in Figures 2.5 and 2.6. The sputtering power was regulated at 70 W in the first case and 150 W in the second and the deposition took place room temperature. The morphological analysis indicated the presence of all known (theoretical) peaks for ZnO material, in both circumstances. No preferential growth was observed during the thin film synthesis and a polycrystalline material was formed. The deposition time was controlled in order to allow the ZnO films formation of equal thickness. Table 2.1 presents the overall deposition parameters for the two aforementioned ZnO films.

Table 2. 1 ***Deposition parameters of ZnO thin films grown by different sputtering power.***

Sputtering Power (W)	*70*	*150*
Thickness (nm)	*200*	*200*
Deposition time (min)	*48.2*	*25.1*
Growth rate (nm/min)	*4.15*	*7.96*

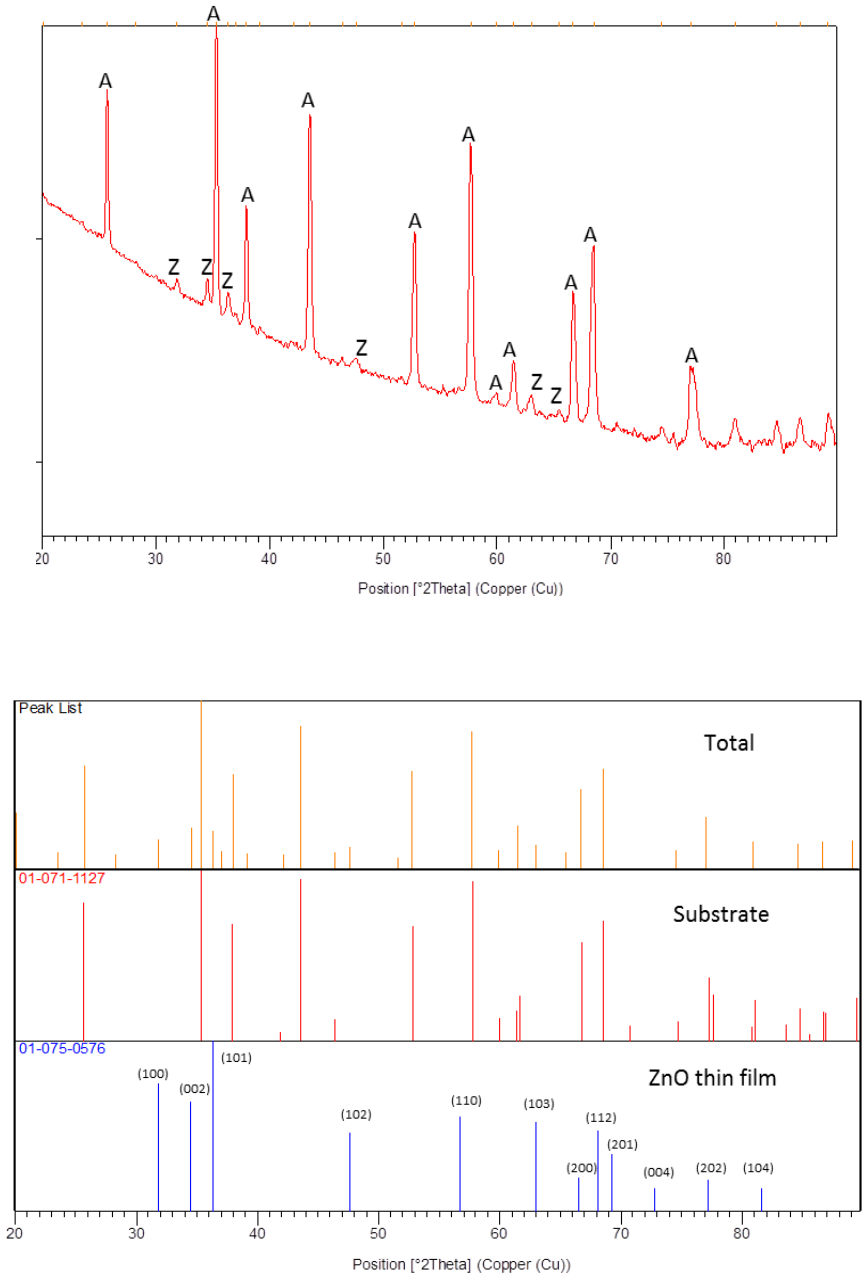

Figure 0.5 ***Upper image: X-Ray diffraction pattern of a 200nm thickness ZnO thin film by RF sputtering at 70W. A, marked peaks, come from the Alumina substrate, while Z peaks from ZnO. Lower image: Separate peak analysis clearly demonstrates a polycrystalline material.***

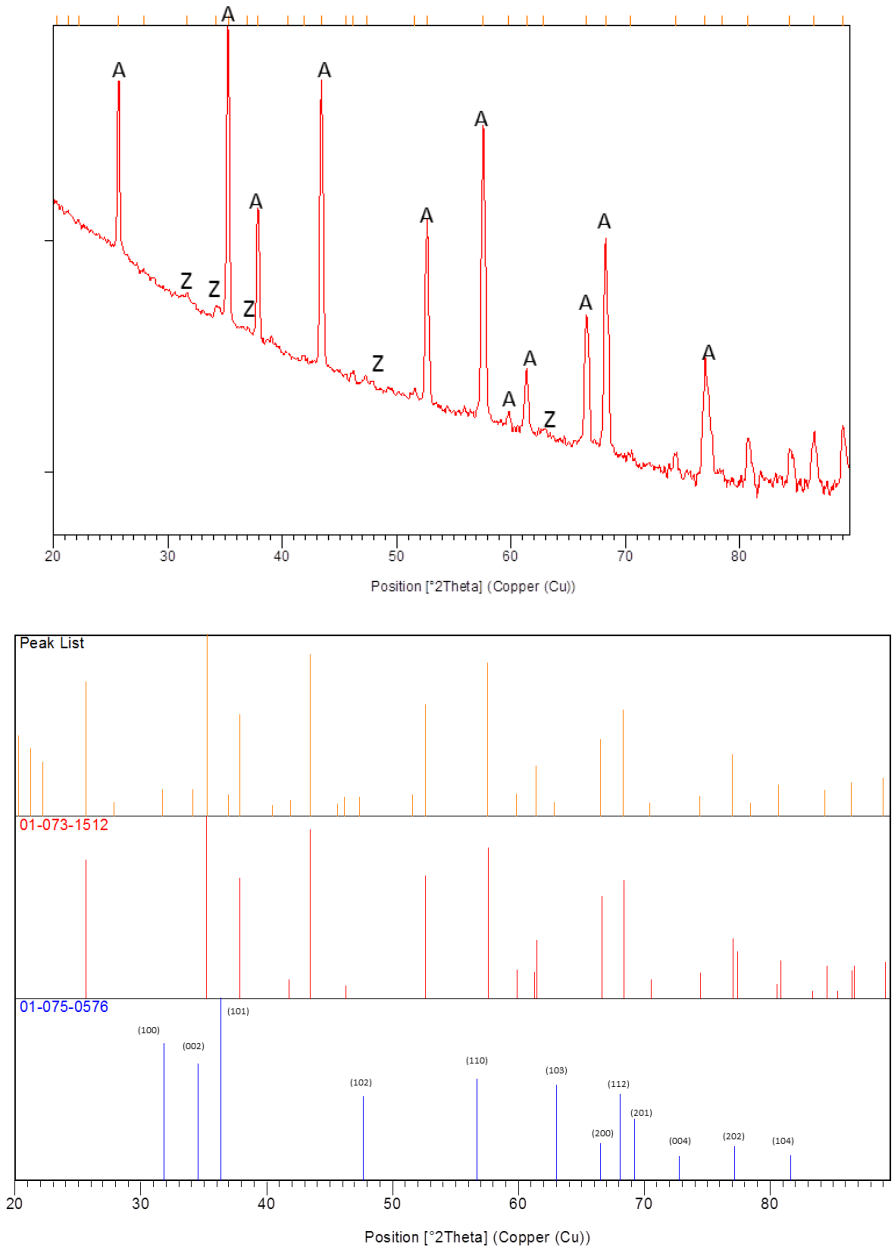

Figure 0.6 ***Upper image: X-Ray diffraction pattern of a 200nm thickness ZnO thin film by RF sputtering at 150W. A, marked peaks, come from the Alumina substrate, while Z peaks from ZnO. Lower image: Separate peak analysis clearly demonstrates a polycrystalline material for this case as well.***

AFM (non-contact mode) morphological analysis was introduced to reveal ZnO's grain sizes and surface roughness. The effect of thermal annealing was investigated in order to determine its influence on the previously grown films. As presented in Figures 2.7, 2.8, 2.9 and 2.10, annealing treatment results in an increase of the grain size, in agreement with other previous reports. The comparison between annealed and not-annealed samples allows the determination of the surface planarity which is crucial for the growth of ZnO nanowires found in the next sub-chapter, using ZnO thin films as nucleation centers.

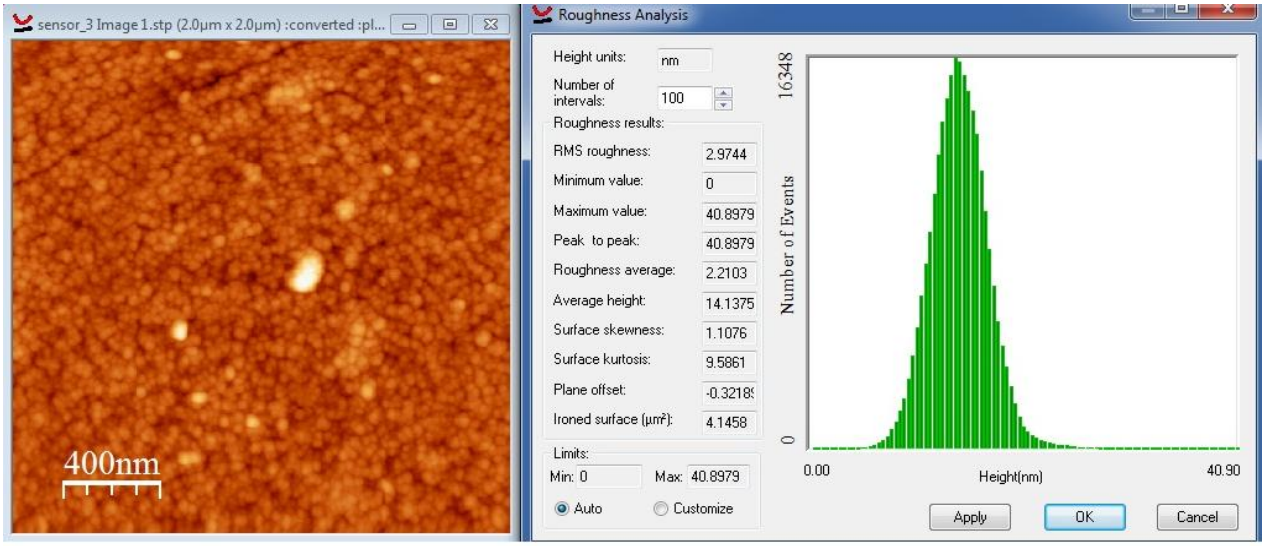

Figure 0.7 ***Left image: ZnO thin film at 70 W, AFM analysis in tapping mode. Right image: surface roughness analysis.***

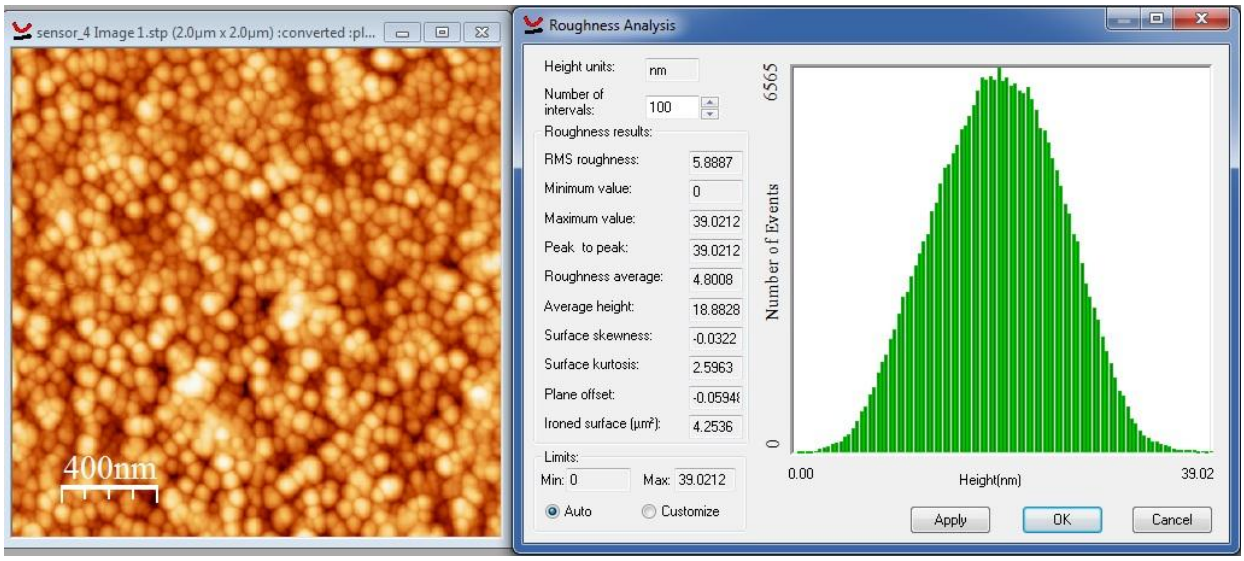

Figure 0.8 ***Left image: ZnO thin film at 70 W, AFM analysis in tapping mode after annealing treatment. Right image: surface roughness analysis.***

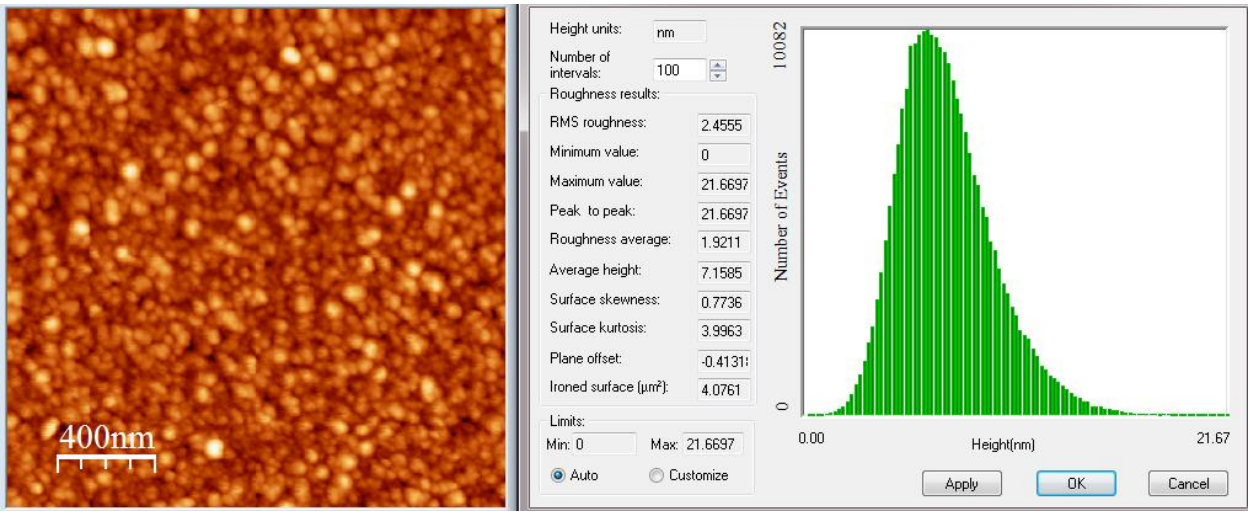

Figure 0.9 ***Left image: ZnO thin film at 150 W, AFM analysis in tapping mode. Right image: surface roughness analysis.***

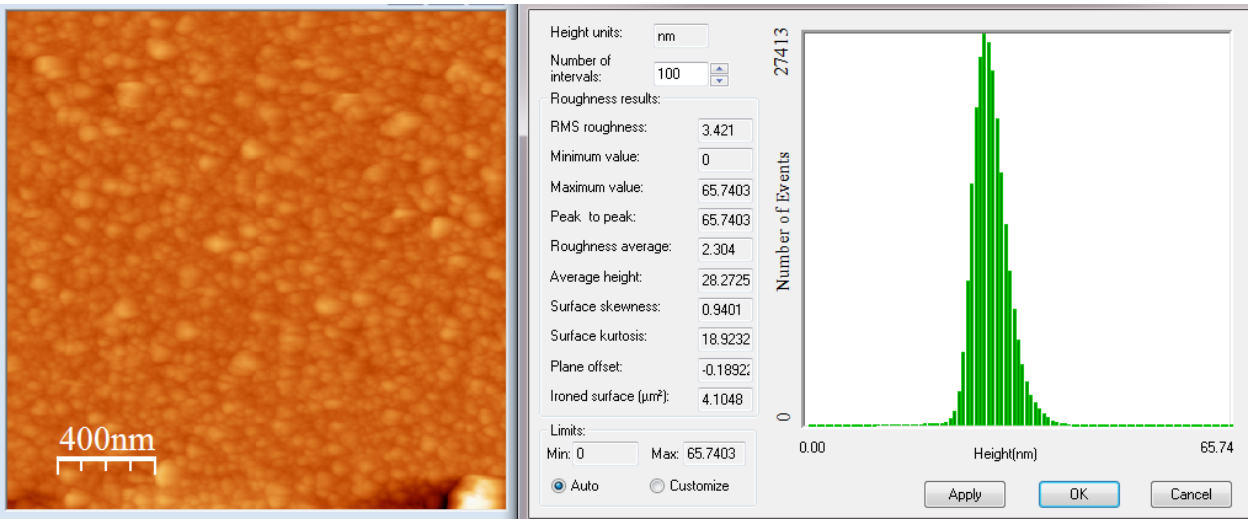

Figure 0.10 ***Left image: ZnO thin film at 150 W, AFM analysis in tapping mode after annealing treatment. Right image: surface roughness analysis.***

2.3 ZnO (1D) Nanowires by Electrochemical deposition

Apart from 2D thin films, many efforts still focus on synthesizing oriented one dimensional ZnO nanostructures. Till date, techniques using sophisticated and expensive equipment but also low temperature and cost-effective methods such as electrochemical deposition (ECD) and hydrothermal deposition were employed for the synthesis of ZnO 1D nanostructures [48][49]. One of the major advantages of electrochemical synthesis is given by its application for scale up and large fabrication feasibility, therefore suitable for an

industrial use [50]. ECD of ZnO nanowires has been focused mostly on the preparation of nanorod/nanowire arrays on flat substrates as well as inside pores of template membranes. The difference between nanorods (NR) and nanowires (NW) lies on their length. Typically a short NW tends to be found as NR within the literature.

Electrochemical deposition involves a chemical bath and three electrodes, which participate in the overall procedure: the working, the reference and the counter electrodes. The working electrode's surface is the place where all the chemical reactions, involving ZnO NRs growth, take place. The reference electrode is used in order to precisely control the deposition potential and the counter electrode is inserted in order to close the electrical circuit and allow the current flow. A graphic representation of the electrochemical cell is given in Figure 2.11, while the actual cell is presented in Figure 2.12.

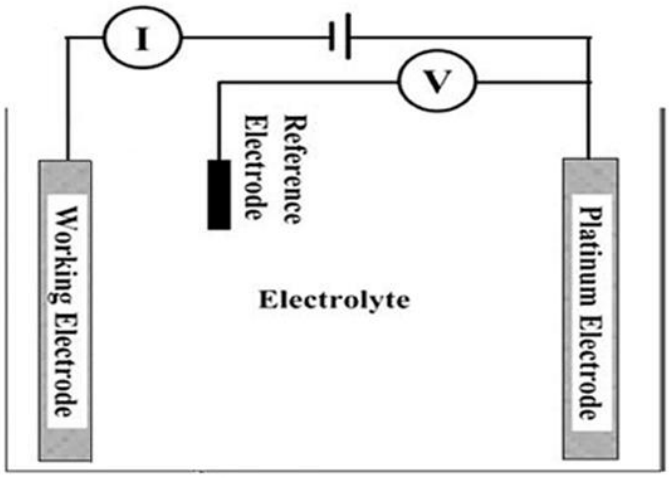

Figure 0.11 ***Basic setup of a three electrode electrochemical cell, employed in ZnO nanorod growth. The cell consists of the working, the counter and the reference electrodes, immersed inside an electrolyte.***

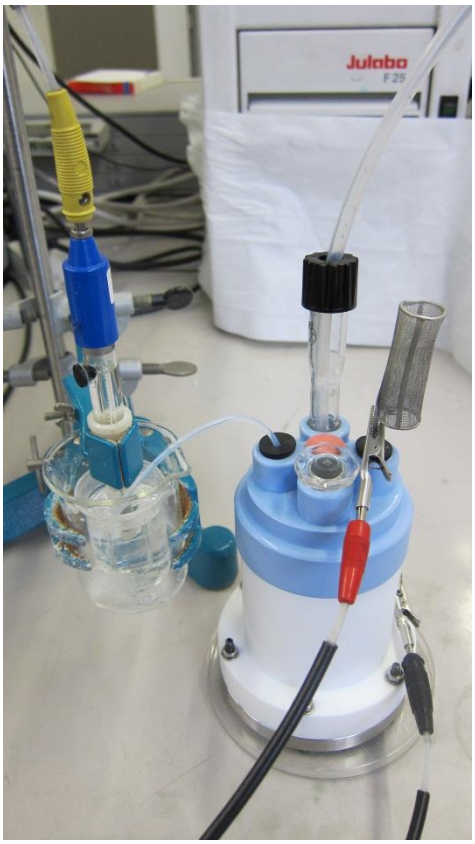

Figure 0.12 ***Actual electrochemical cell used in the growth process of ZnO nanorods.***

ZnO synthesis by ECD is based on the cathodical reduction of an oxygen precursor at the surface of the working electrode. Three main oxygen precursors have been proposed in the literature until now [51] [52].

- Molecular oxygen (O_2)
- Nitrate ions (NO_3^-)
- Hydrogen peroxide (H_2O_2)
-

The general outline for ECD of ZnO nanorods is supported as follows:

$$\text{Nitrate: } NO_3^- + H_2O + 2e^- \rightarrow NO_2 + 2OH^- \quad [2.1]$$

$$\text{Hydrogen peroxide: } H_2O_2 + 2e^- \rightarrow 2OH^- \quad [2.2]$$

$$\text{Molecular oxygen: } O_2 + 2H_2O + 4e^- \rightarrow 4OH^- \quad [2.3]$$

All three previous reactions allow the generation of hydroxide ions (OH^-). In order to form ZnO, these hydroxide ions should combine with Zinc ions (Zn^{2+}). As Zinc precursors are used either Zinc chloride ($ZnCl_2$) or Zinc Nitrate ($Zn(NO_3)_2$), which guarantee the presence of Zinc ions inside the chemical bath. Once hydroxide

ions are formed, they immediately precipitate in presence of Zinc to form Zinc hydroxide $Zn(OH)_2$ which is easily dehydrated above 65°C to form ZnO, according to the following chemical reactions.

$$\text{Chemical precipitation: } Zn^{2+} + 2OH^- \rightarrow Zn(OH)_2 \quad [2.4]$$

$$\text{Dehydration: } Zn(OH)_2 \rightarrow ZnO + H_2O \quad [2.5]$$

The process evolves itself drifting the pH of the electrolyte to a constant increase and to a local super-saturation of the bath in the vicinity of the electrode, thus provoking the precipitation on the electrode surface of ZnO. Therefore, a specific crystal order requires the pH control of the electrolytic solution to a proper value. In this chapter the growth of ZnO NR in free standing mode, as well as in porous templates is reported.

2.3.1 ECD ZnO Nanorods in free standing mode

2.3.1.1 ZnO Nanorods on indium tin oxide (ITO) substrates

The whole growth process starts with the appropriate selection of the substrate electrodes. Since the movement of the ions inside the solution is guided by an electric field, conductive electrodes are selected for this step. Two types of electrodes are used in this study, indium tin oxide (ITO) covered glass and gold (Au) coated silicon (Si). Both of these two options offer adequate conductive properties, suitable for ECD synthesis.

Initial experiments were performed in pre-deposited ITO/glass (Diamond coatings [53]) in order the deposition growth parameters to be investigated. The electrolyte prepared was a solution containing 5 mM of $ZnCl_2$, 0.1 M of KCl and 5 mM of H_2O_2. The presence of zinc chloride and hydrogen peroxide was explained previously. The addition of potassium chloride in the solution guarantees the good electrical conductivity of the electrolyte. All experiments were controlled via an AMEL 5000 Potentiostat/Galvanostat presented in Figure 2.13.

Figure 0.13 ***AMEL 5000 Potentiosat/Galvanostat, controlling the growth process.***

Before the actual deposition linear polarization studies were performed on ITO covered glass as reported in Figure 2.14. The method consists in generating hydroxide ions at the surface of the cathode by reduction of the oxygen precursor. The cathodical reduction was observed from -0.7 V to -1 V, meaning that any potential value applied within this range is capable of initiating the deposition of ZnO nano-structures. In the following experiments, the potential values in the range -0.7 to -1 V were applied, following the potentiostatic (or chrono-amperometric) mode and the effect of deposition potential on the obtained ZnO nanowires was assessed. The counter electrode was a platinum (Pt) grid and the reference electrode was a saturated calomel electrode (SCE). The temperature was monitored continuously and regulated at 75 °C. As potential and current distribution is governed by phenomena related to charge transport in the electrodes and charge/mass transport in the electrolyte [54], the influence of over-potential on current distribution must be taken into account.

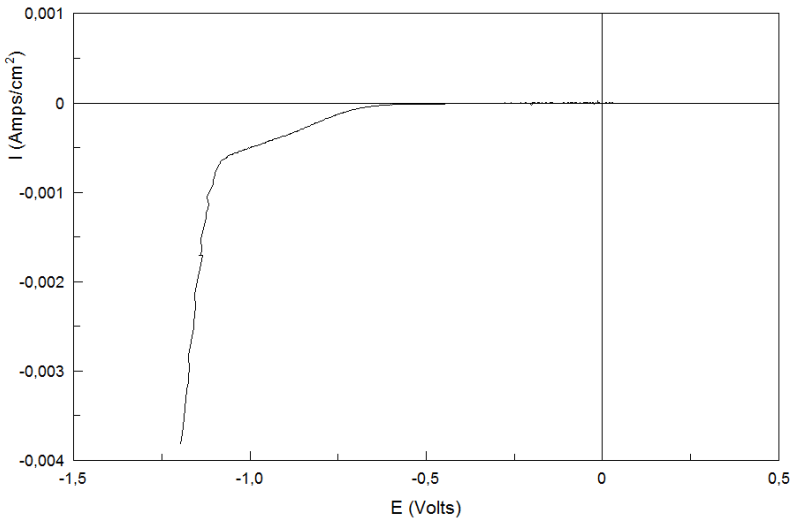

Figure 0.14 ***Linear voltammetry curve on ITO covered glass, as working electrode. Electrolyte used: 5 mM of $ZnCl_2$, 0.1 M of KCl and 5 mM of H_2O_2 at a scan rate of 100 mV/sec.***

A typical I-t curve, showing the variation in current values during the growth is presented in Figure 2.15. In this case, the potential was fixed at -700 mV, allowing the current monitoring. As shown, the current is decreasing as an absolute value during the growth of ZnO nanomaterials, which reveals the increase of the resistance during the growth. Such phenomena could be explained by the formation of ZnO semi-conductive nanostructures on the working electrode, which combined with the decreased concentration of second species conductors (ions), modify the overall observed resistance. The same effect (increase of resistance) happens when potentiostatic mode is applied in more negative potential values as well.

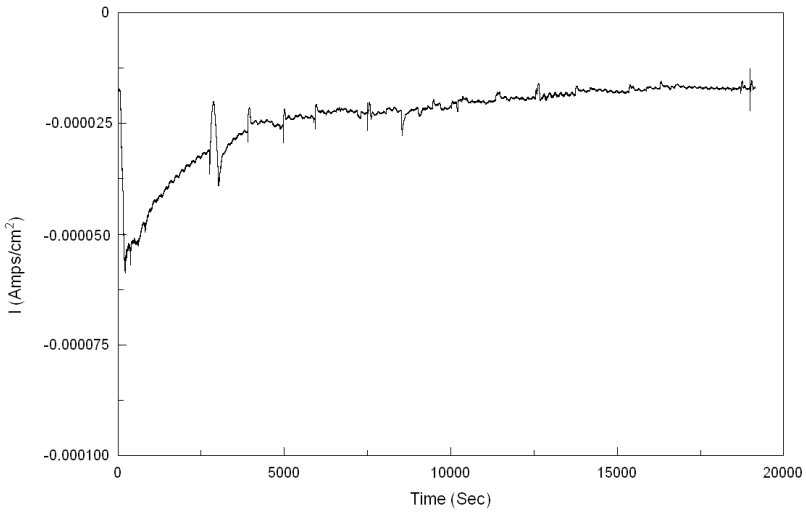

Figure 0.15 ***Chrono-amperometric diagram of ZnO NW deposition on ITO substrate, at -700 mV.***

Morphological characterization of the grown material was done by means of Fei 200 3D SEM, structural characterization by X-Ray Diffraction and elemental characterization by EDS system integrated on the Fei SEM microscope. In Figure 2.16 is presented a comparison between the ZnO nanostructures grown in potentiostatic mode in four different applied potentials, for two hours of deposition. These top-view images show slight but satisfactory degree of verticality for the as-grown NRs. An interesting remark is that the NR density increases along with the deposition potential from -700 to -900 mV and decreases again after -900 mV. This is happening because as moving the potential closer to -1 V the nucleation and the growth of the particles happen in a faster rate, which leads to larger agglomeration. Figures 2.17 and 2.18 present the NR length and diameter, plotted versus the deposition potential and NR density for the ECD growth. Further experiments done in more negative potentials revealed the deposition of Zinc metal nano-structures (films and larger particles) instead of ZnO nanorods. Figure 2.19 describes the general rule associated with ZnO nanostructures growth by electrochemical deposition on ITO substrates. According to this figure, the ZnO NR growth takes place in the whole range of deposition potentials investigated, from -0.7 V to -1 V, assessed as well by the linear polarization measurements. The difference among the growth conditions lies on the fact that less negative potentials (close to -0.7 V) favour the nucleation step, but offer slower growth rates. On the other hand more negative potentials (close to -1 V) lead to higher growth rate by supplying more ions to the reaction. The optimal growth conditions include the regulation between the nucleation centres and the material growth. In the linear polarization graph this is presented by a peak in the current at a specific voltage. In the case of ITO, the position of this peak was not so obvious, as in the experiments following for Au/Si substrates.

The results concerning the growth of ZnO nanorods on ITO can be expanded to other substrates as well, due to the similarity in the chemical processes applied. In this way, the correlation between the linear polarization initial measurements and the final conclusion after the growth is possible and allows the selection of the appropriate growth potential prior to the growth procedure.

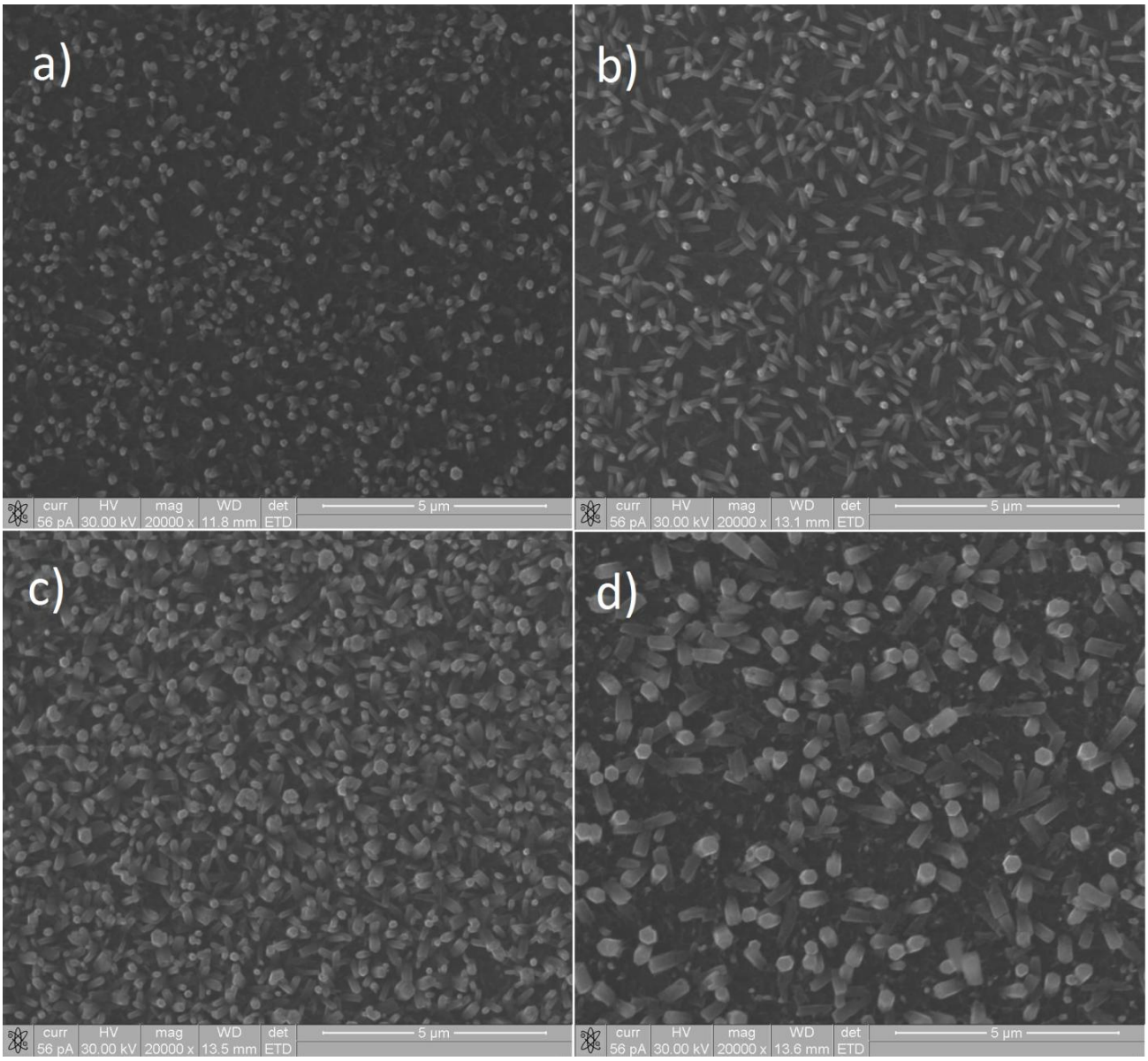

Figure 0.16 ***SEM micrographs of ECD ZnO nanorods on ITO substrates by potentiostatic mode. Potential selected: (a) -700 mV, (b) -800 mV, (c) -900 mV and (d) -1000 mV.***

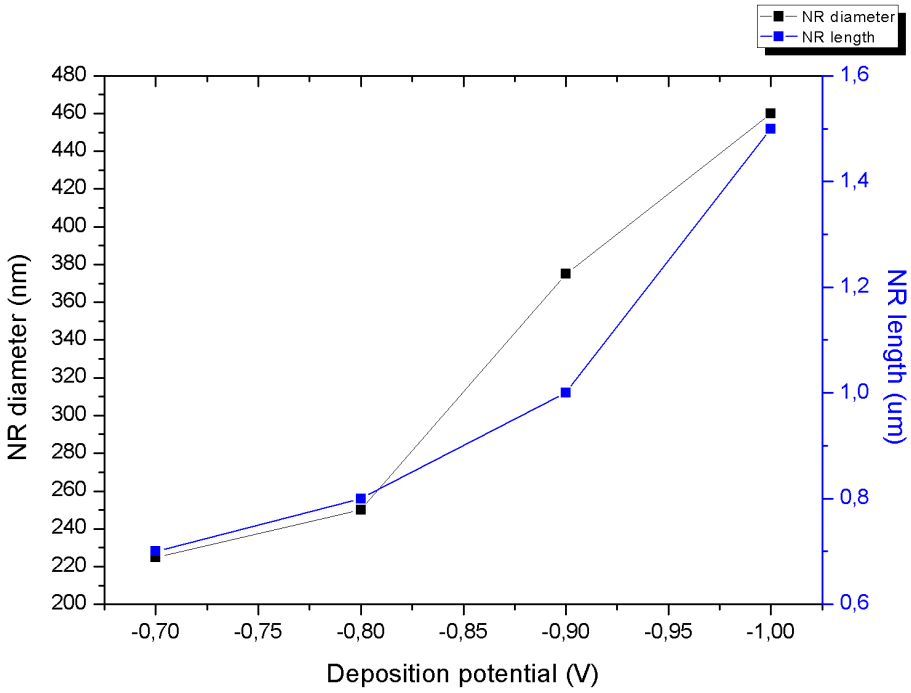

Figure 0.17 ***ZnO NR length and diameter vs. deposition potential.***

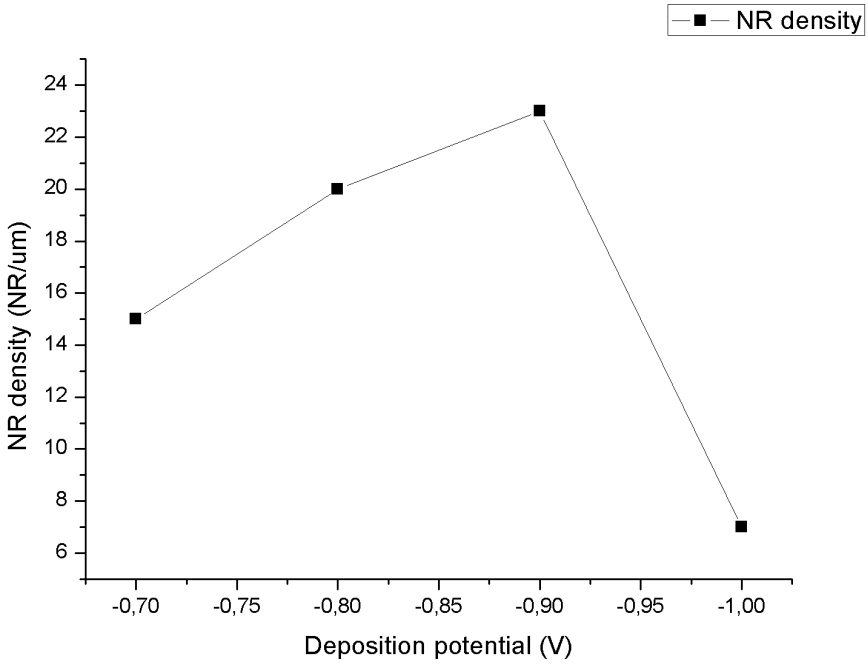

Figure 0.18 ***ZnO NR density vs. deposition potential.***

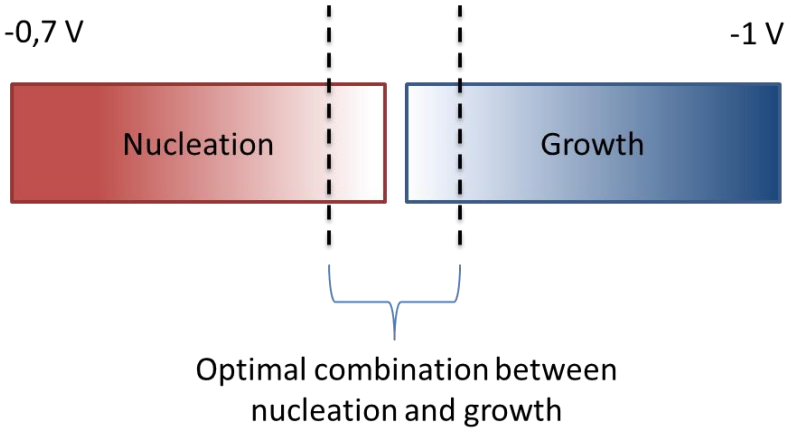

Figure 0.19 ***Growth mechanism, prevailing the synthesis of ZnO nanostructures by electrochemical deposition.***

From the previous results, Figure 2.16(c) (V= -900 mV) expresses the highest NR density and for this reason, the sample referring to this picture was selected for further investigation. Elemental analysis (EDS) certifies the nature of the NR, presented in Figure 2.20. Zinc and oxygen presence are obvious, as well as some peaks related with the substrate like Indium and Tin. XRD analysis shown in Figure 2.21 exhibits the facets of the ECD ZnO crystals presented on Figure 2.16(c). Three of the most commonly found peaks of ZnO ([100], [002], and [101]) are presented in this graph. The (002) peak is detected with slightly higher intensity than the rest, which represents the vertical growth of the nanorods along the polar [0001] axis. The other two facets correspond to laterally grown nanorods. The remarkably high peak close to 30° degrees is not associated with the nanorods as a theoretical peak at that region is not associated with ZnO and it was attributed to the ITO substrate.

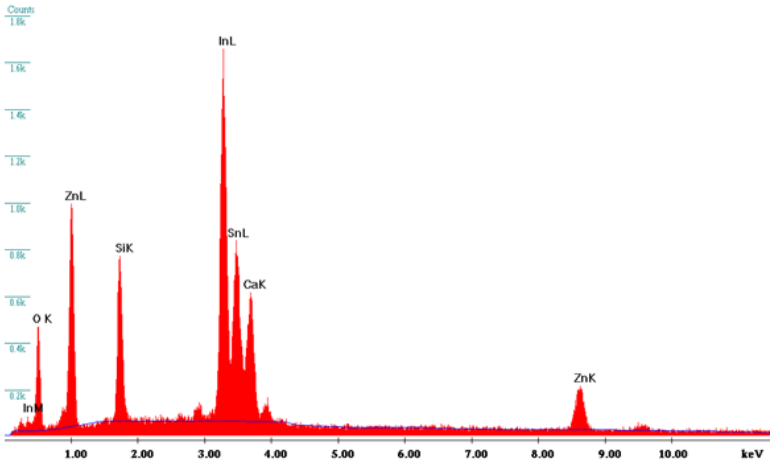

Figure 0.20 ***EDS elemental analysis on ZnO NR from Fig. 2.16.***

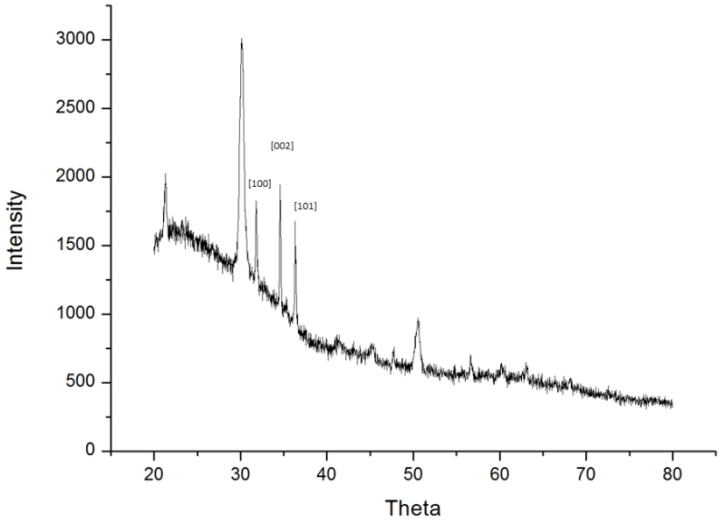

Figure 0.21 ***XRD pattern of ECD ZnO nanorods from Fig 2.16.***

3.3.1.2 ZnO Nanorods on gold coated silicon substrates

Literature studies on ZnO nanowire growth by electrochemical deposition suggest the substrate's planarity as an important factor for the vertical growth (c-axis orientation) of the ZnO nanorods. For this reason the use of sputtered Au films on Si, as substrates was investigated. Tapping mode AFM measurements (Figure 2.22) were performed on both, Au/Si and ITO/glass to express their surface roughness. The results indicate Si/Au (Ra: 1.76 nm) as better substrate candidate, since it offers smaller RMS roughness values than ITO (Ra: 2.87 nm).

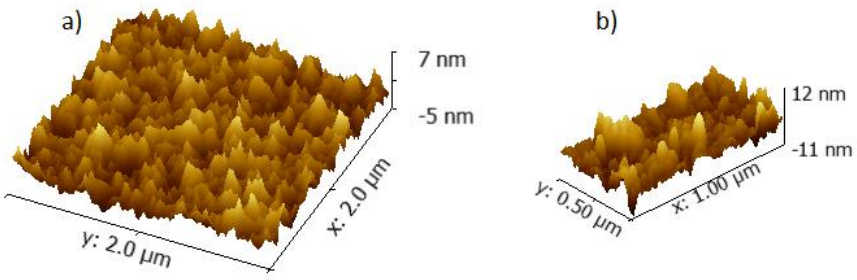

Figure 0.22 ***Surface topography, AFM tapping mode of (a) Au/Si and (b) ITO/glass substrates.***

In this case, a freshly cleaned Au coated Si wafer was used as the supporting electrode. As in the case of ITO substrates, polarization resistance experiments were performed before the actual growth to identify the optimal deposition potential and are presented in Figure 2.23. The linear voltammetry scan indicates an onset at -700 mV, exhibiting in the same time a clear peak around -850 mV. The previous analysis (for ITO) designates the selection of this specific potential for ZnO deposition.

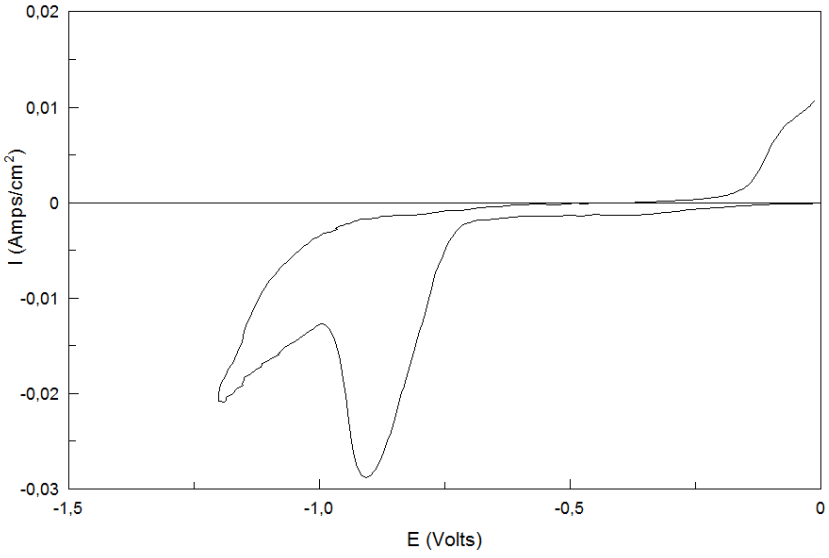

Figure 0.23 ***Linear voltammetry curve on Au/Si substrate as working electrode, at a scan rate of 100 mV/sec.***

Vertically-aligned ZnO NRs were grown at 85 °C in a single ECD step from a solution containing 1mM $ZnCl_2$ (Aldrich 99.999%), 100mM KCl and ultra-pure deionized water. KCl was added in the bath to assure the proper electrical conductivity during growth. Ag/AgCl and a Platinum grid were used as reference and counter electrodes respectively. Potentiostatic mode was selected, and the applied potential was set to -800mV with respect to the reference. The molecular oxygen was supplied to the bath separately from an external tank.

This approach yielded large aspect ratio NRs in a relatively short-time synthesis [55]. The process was reported to occur in two steps. The oxygen is first electro-reduced at the Si/Au substrate surface to form OH^- ions (Eq. 2.3), which are then consumed to generate zinc hydroxide – $Zn(OH)_2$, the precursor preceding the ZnO formation by dehydration (Eq. 2.4 and 2.5).

Figure 2.24 shows SEM micrographs top (a), 45° tilted (b), of the ECD ZnO NRs. A uniform and homogeneous array of dense ZnO NRs vertically-aligned to the Si/Au substrate was obtained. Notably, the ZnO NRs exhibited a good degree of verticality as emphasized by the closed-up SEM magnification in the inset of Fig. 2.24(b), as well as an excellent hexagonal symmetry as shown in the TEM microtome cross-sectional slice view depicted in the inset of Fig. 2.24(a). Straightforwardly, the latter feature can be attributed to the Wurtzite-type crystallographic structure of ZnO [56]. ZnO NR of average length ~1.5 μm and with a lateral size of ~150 nm prepared in these conditions exhibited a density of 125 NRs/μm^2.

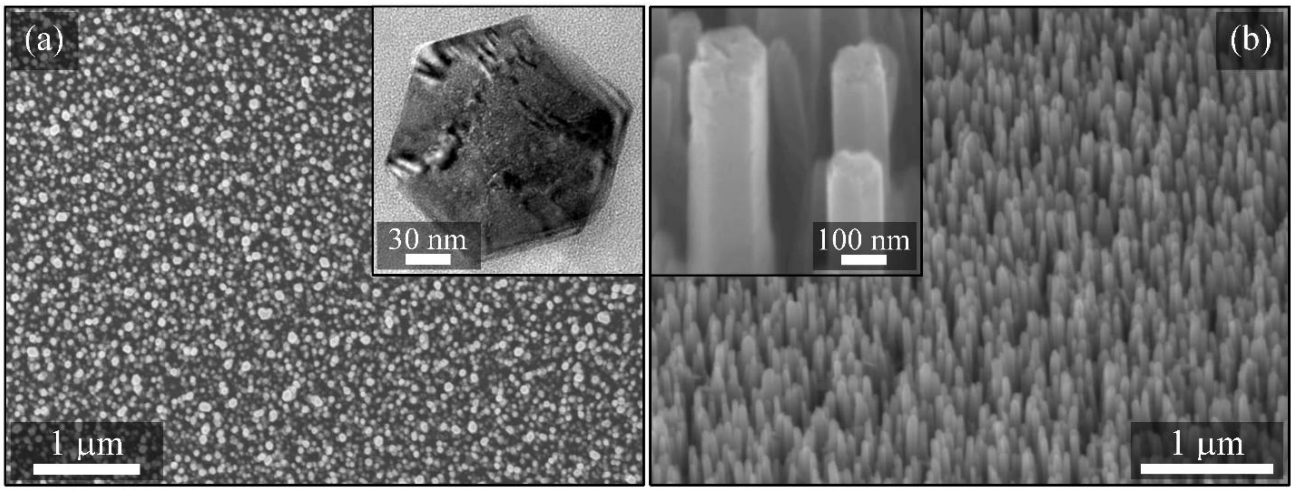

Figure 0.24 ***Scanning electron microscope (FE-SEM) images (a – top and b – 45° tilted sample). Inset of (a): Transmission electron microscope (TEM) image (bright-field view) of a cross-sectional slice through a single NR, showing its excellent hexagonal symetry. Inset of (b): Corresponding closed-up magnification, emphasizing the high degree of NRs verticallity and orientation.***

Elemental analysis presented in Figure 2.25, showed clear presence of zinc and oxygen traces. Figure 2.26(a) shows the XRD spectra acquired for the Si/Au – grown ZnO NR arrays presented in Figure 2.24. The observed Si and Au peaks were assigned to the supporting Si/Au substrate (JCPDS 27-1402 and JCPDS 04-0784, respectively), although the intensity of the Si (111) peak was relatively low due to the presence of the dense ZnO NRs array. In contrast, the strong peak found at $2\theta_{NRs} = 34.51°$ was due to the reflections from the (002) planes of the Wurtzite hexagonal phase of ZnO (JCPDS 36-1451), indicating the preferential growth of the ZnO

NRs perpendicular to the substrate (as confirmed also by the SEM images shown in Fig. 2.24) [57]. The tiny shift of the ZnO (002) peak position to the right compared to the ideal value corresponding to the ZnO bulk material ($2\theta_{bulk} = 34.422°$ - indicated in Fig. 2.26(a) by the black dashed line) can be attributed to possible defects in the crystalline network of the as-grown ZnO NRs[58]. The crystalline lattice constant was estimated from the XRD spectra to be in excellent agreement with the JCPDS data ($c_{NWs} = 5.21\text{Å}$ versus $c_{bulk} = 5.20\text{Å}$).

Figure 2.26(b) gives a high magnification TEM image through a single ZnO NR acquired perpendicular to the growth axis. The distance between two succesive lattice planes was measured (see Fig. 2.26(b)) to be about ~0.52 nm, in good agreement with both, XRD spectra (see Fig. 2.26(a)) calculations and the expected value for the Wurtzite hexagonal phase of ZnO. Furthermore, the NR axis corresponded perfectly to the c-axis. This result can be coupled with the SAED pattern (bright-field image) in the inset of Fig. 2.26(b) confirming the excellent crystalline alignement toward [0001] direction.

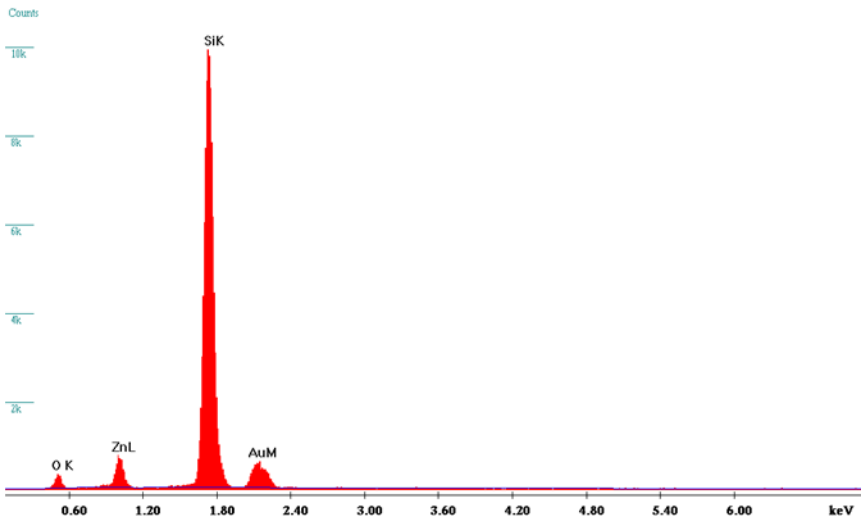

Figure 0.25 ***EDS elemental analysis on ZnO NR from Fig. 2.24.***

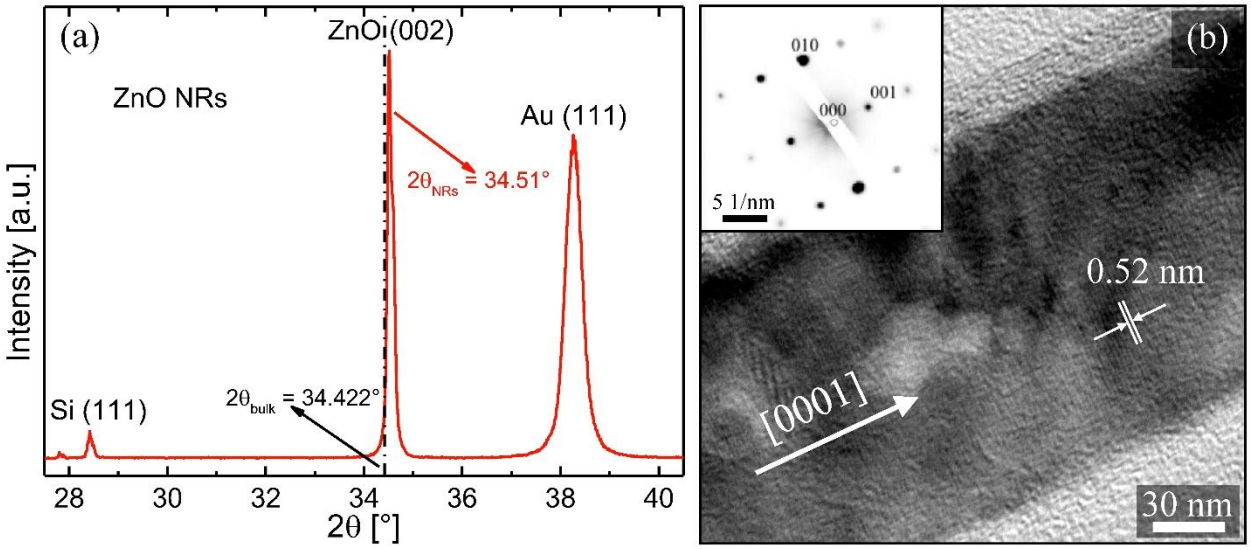

Figure 0.26*(a) X-ray diffraction (XRD) spectra acquired from a Si/Au substrate with electrodeposited vertically-aligned ZnO NRs. The peak position corresponding to the ZnO bulk material is indicated by the dashed black line. (b) Higher magnification TEM image through a single ZnO NR, showing a good alignment of the growth direction with the c-axis of the ZnO Wurtzite structure. The inset: selected area electron diffraction (SAED) pattern (bright field view) confirming the excellent crystallinity of the prepared ZnO NRs.*

2.3.2 ZnO Nanowires in porous templates

2.3.2.1 ZnO Nanorods in anodic porous alumina (APA)

For the fabrication of the APA template a well established (CRF Labs) but lengthy process has followed (Figure 2.27). Using as substrate ITO/glass, a titanium thin film which serves as adhesion promoter was deposited. After that, the deposition of a thicker film of tungsten takes place and then, by RF sputtering at the begining and electron beam evaporation later, a thick aluminum film of around 500nm. Two step anodization process was followed for the fabrication of APA. The initial stage, was done using oxalic acid for several minutes in order to create the initial pores in aluminun. Etching of APA using CrO_3 was performed in order to lead the second anodization direcly to the fabricated holes. Using once again the oxalic acid the second anodization step had been performed. That step was followed by the widening of the pores to remove tungsten and titanium and allow a free path to the ITO surface (electrode for ECD). The fabricated APA in its final form is presented in Figure 2.28 together with a top and tilt view of a SEM micrograph.

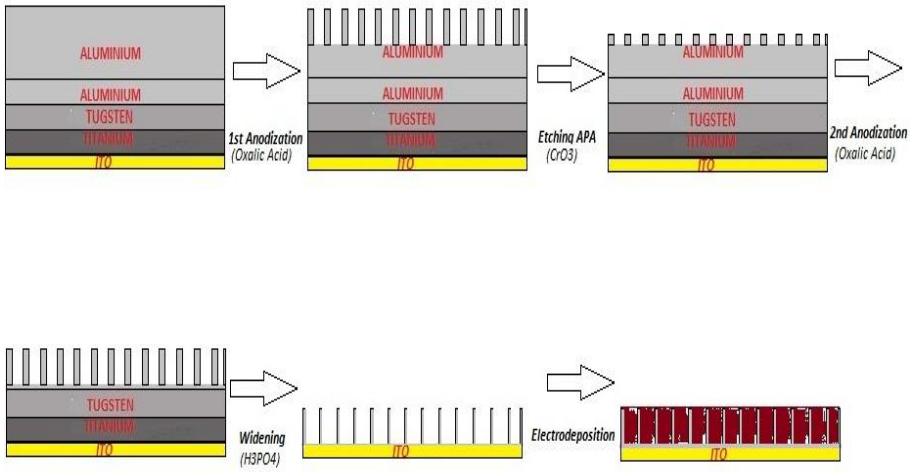

Figure 0.27 ***Anodic porous alumina (APA) fabrication process, schematic representation.***

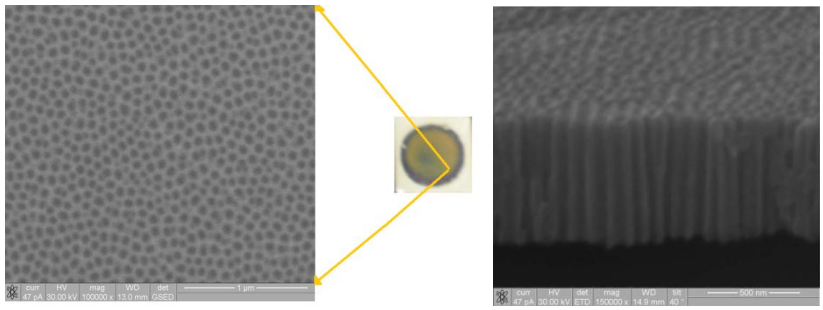

Figure 0.28 ***Actual APA picture and SEM micrographs showing the pore distribution, diameter and density top and tilt views.***

The APA porous structure is used as a template inside which electrodeposition takes place to grow vertically aligned ZnO NRs. Once again, linear polarization measurements performed before the actual growth to identify the optimal deposition parameters, presented in Figure 2.29. From this graph a clear onset shift to more negative values than in the case of planar surfaces is observed. This behavior was adressed to the higher resistance exhibited by a porous electrode than a planar one. The electrolyte used in ZnO NR growth in APA templates was a solution containing 0.05 M of $Zn(NO_3)_2$. Once again potentiostatic mode was selected and the potential was set at -1 V. The deposition lasted for 30 minutes at 85°C.

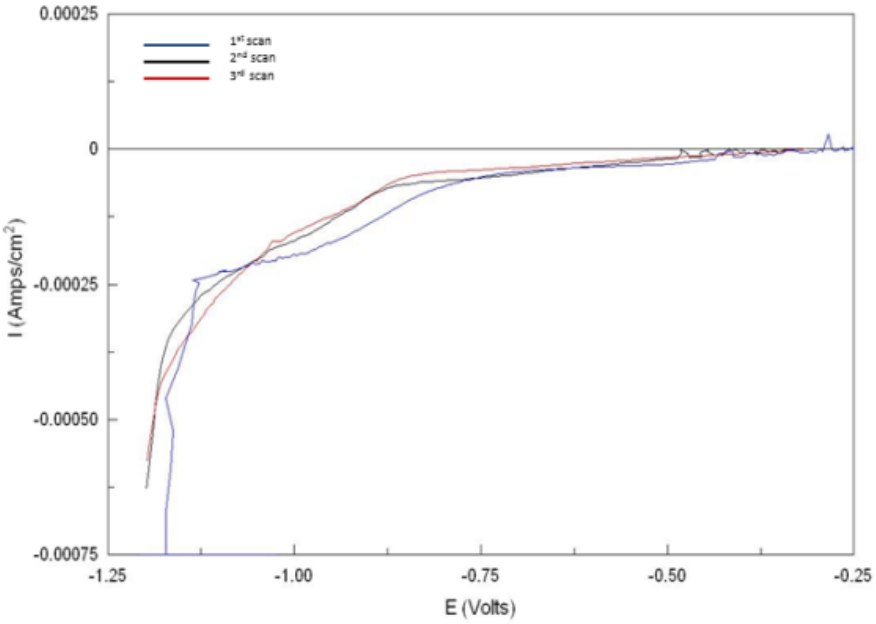

Figure 0.29 ***Linear voltammetry curve on APA/ITO substrate at a scan rate of 100 mV/sec.***

The results of this experiment are presented in Figure 2.30. It is not evident whether the growth happened inside the pores or only on their tops. A possible explanation is that the electrolyte did not impregnate inside the pores in combination with improper anodization of alumina (rendering it conductive). The use of an organic based electrolyte, like dimethylsulfoxide (DMSO) is suggested to enhance electrode's wettability [59]. A novel electrolyte was prepared by maintaining the same concentration on $Zn(NO_3)_2$ and substituting the deionised water with DMSO. Figure 2.31 shows the ZnO NRs grown inside APA pores by means of organic based electrolyte, after the dissolution of APA template (with KOH or NaOH).

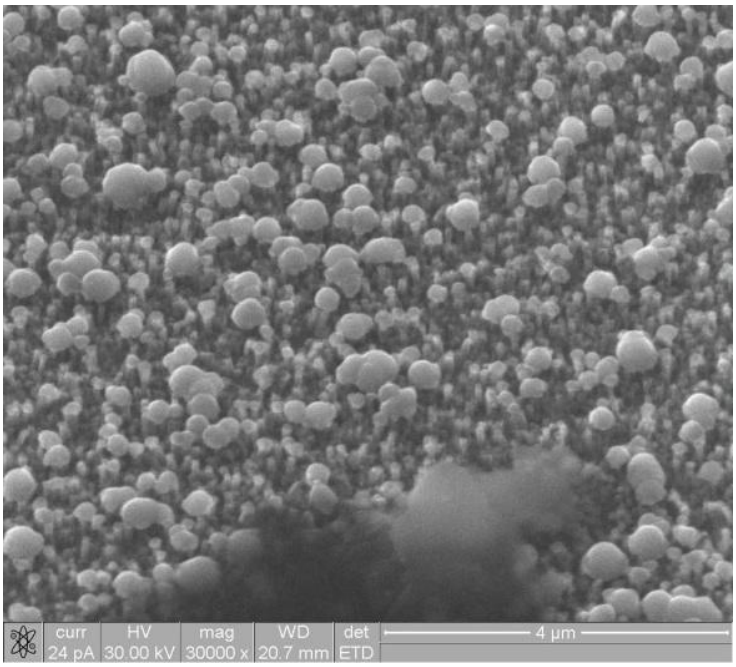

Figure 0.30 ***Growth result of ZnO deposition on APA by aqueous $Zn(NO_3)_2$ based solution.***

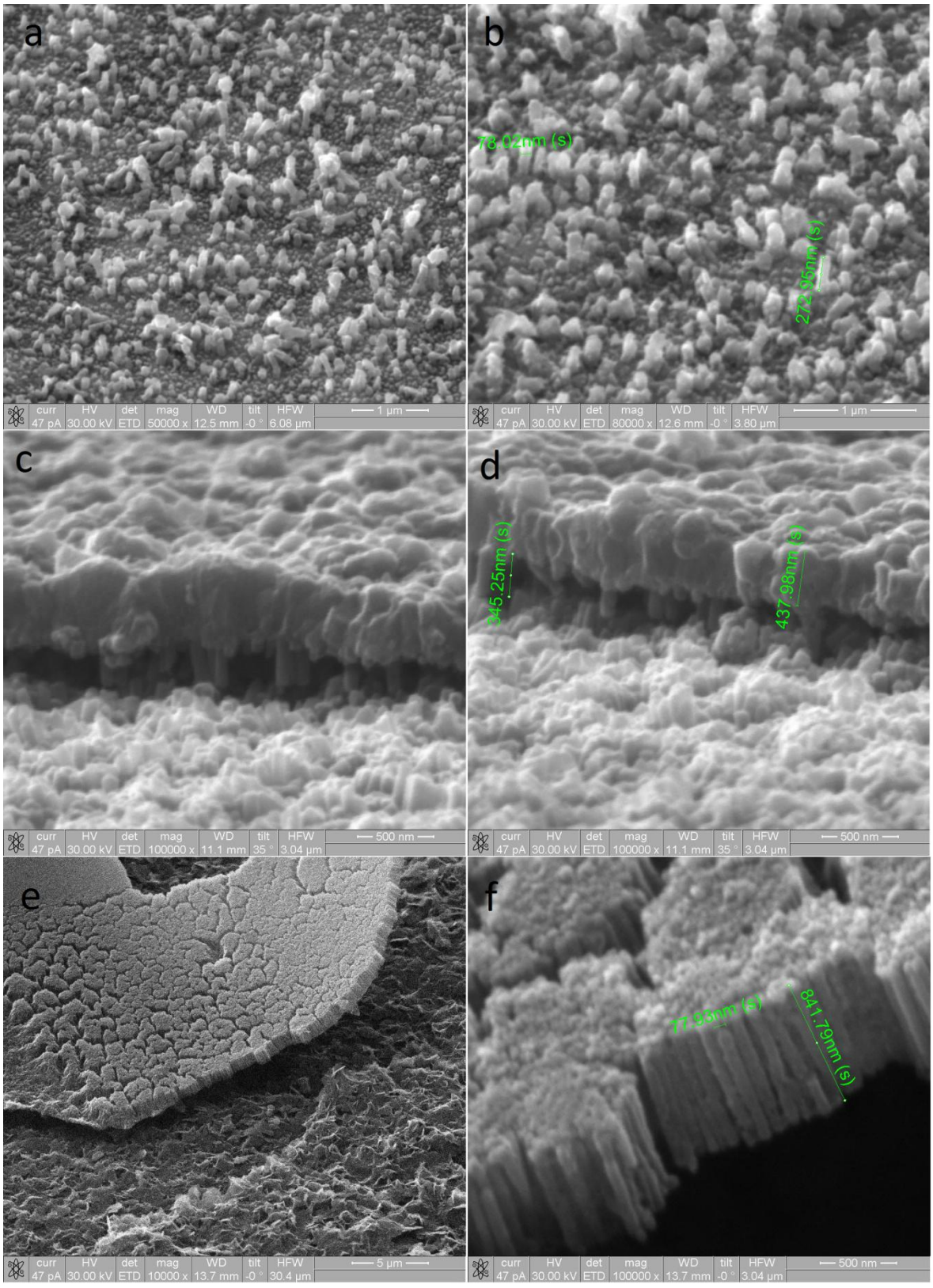

Figure 0.31 ***SEM micrographs of ZnO NR inside APA templates, (a), (b) after the dissolution of APA template, (c), (d) partial template dissolution, (e) cluster made by ZnO NR and (f) higher magnification of the ZnO cluster, clearly demonstrate the NRs.***

From the previous SEM micrographs, it is indicated that DMSO promotes the NR growth inside the porous structures. XRD structural characterization assesses the use of organic based electrolyte for ZnO NR growth. Figure 2.32 presents the X-Ray diffraction patterns of an empty APA template and ZnO NR grown inside APA by aqueous and organic solutions [59]. In this graph, higher peaks addressed to ZnO are clearly presented for the case of organic based electrolyte than the aqueous one.

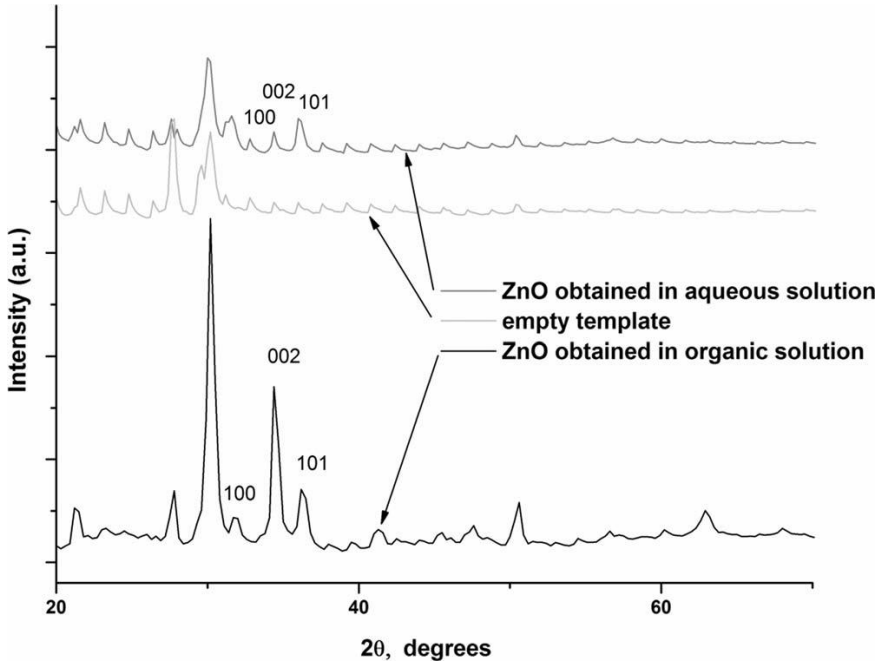

Figure 0.32 ***XRD pattern of the ZnO NR arrays embedded in the alumina template/ITO substrate*** **[59].**

2.3.2.2 ZnO Nanowires in Polycarbonate track-etched membranes

Besides APA templates, commercially available polycarbonate track-etched membranes (by ion bombardment) were investigated as ECD supporting structures for the template growth of ZnO NW arrays. For the scope several templates were studied, whose holes' diameters and lengths were varying from 10 to 100 nm and from 5 to 16 um respectively. Thermal evaporation technique was employed for the fabrication of bottom contact (metal electrode) at membrane's back side. The chosen material was Au as it offers acceptable adhesion with the template and furthermore do not damage the polycarbonate membrane.

The working electrode in this case was immersed into the electrolyte by a pipe system made by Teflon, allowing the diffusion of electrolyte only from the upper part (side exposed to the electrolyte), Figure 2.33. Electrical connection with the bottom electrode was done by an aluminum disk found in the interior of the pipe. On the top a rubber gasket was inserted, avoiding the electrolyte's penetration inside the pipe structure.

In this way the polycarbonate membrane is in contact with the electrolyte at its one side and with the aluminum disk on the other (bottom electrode). A schematic representation of the growth inside the membranes is depicted in Figure 2.34.

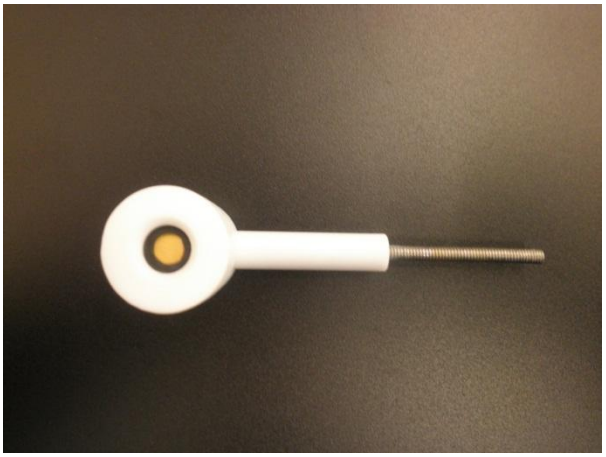

Figure 0.33 ***Pipe system engaged in electrochemical deposition inside polycarbonate membranes. The design allows only one side of the membrane to be exposed to the electrolyte.***

The ideal scenario involves the deposition until the membrane holes are fully covered by ZnO. Experimental findings however, reveal that is quite unlikely to achieve a simultaneous and homogenous pore filling. The deposition stops when a sharp increase in the current (absolute value) is observed at the I-t deposition curve (Figure 2.35). This remark shows that the resistance is instantaneously decreasing. Such a behavior is addressed to at least one fully covered hole and therefore deposition will be favored at that specific point more than at the rest areas. At the end a ZnO thin film (responsible for resistance decrease) is formed on top of polycarbonate membranes, inhibiting the growth inside them. Consequently, the deposition time varies and specifically depends on the time of a single pore complete filling. After the deposition ends, the polycarbonate membrane can be chemically dissolved releasing the nanowires into a suspension of isopropanol solution.

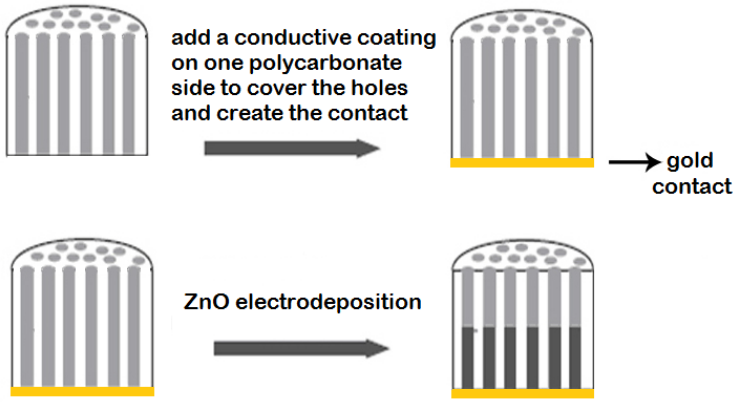

Figure 0.34 ***Schematic representation of the ECD steps process in template membranes.***

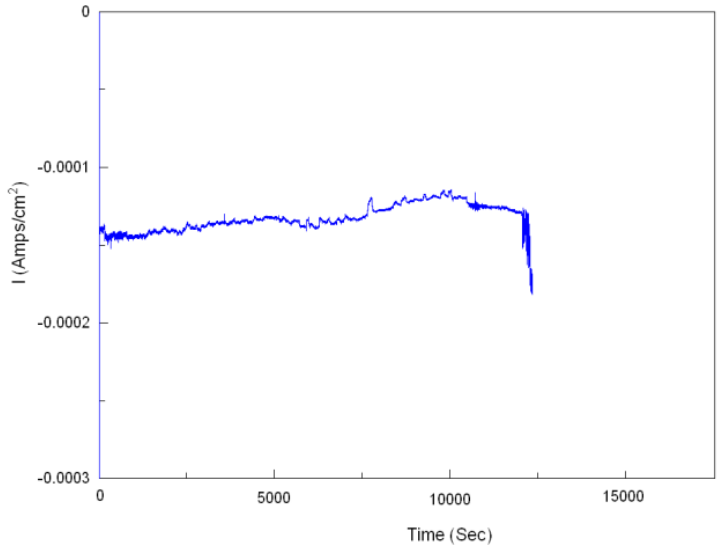

Figure 0.35 ***Current density diagram collected during the ZnO NW deposition in the polycarbonate track etched membranes.***

SEM images presented below show the ZnO NW left after the dissolution of the polycarbonate membrane. In each case the diameter was the same of the mold of each hole and their length was ranging according to the filling cover factor of the pores. An important comment states that nevertheless the shape and structure of the NR are quite good, their density remains notably poor. Even after the membrane dissolution, it gets quite challenging to spot and identify the remnant NW. As seen in Figure 2.36 the density of these NW approaches few tens over a square micron. This number is rather small for up-scaling the template ECD (TED) to fabricate NW for any use except research purposes. Therefore, in the present activity is rather unfeasible to choose this technique for a massive production of piezoelectric sensors. Experimentally the best growth results in terms of density, homogeneity and length were obtained by using potentiostatic mode at -1.05 V for 3 hours of deposition in membranes having pore diameters of 100nm (Figure 2.36 a, b and c).

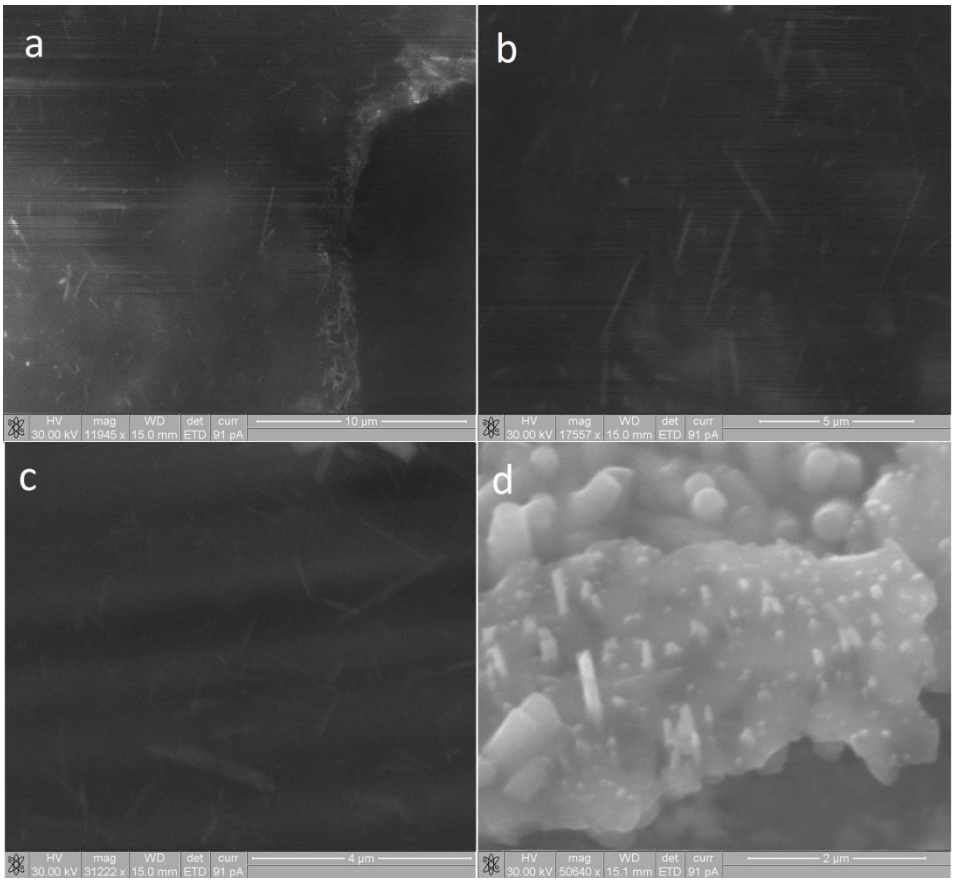

Figure 0.36 ***SEM micrographs of ZnO NW synthesized in PC membranes in different magnifications. Images were recorded after the dissolution of the membrane. Potentiostatic mode was used for 3 hours of deposition, (a), (b) ,(c) deposition potential regulated at -1.05V and (d) -1.2V.***

2.4 ZnO Nanowires by Hydrothermal growth

Additionally to electrochemical growth, in the present thesis hydrothermal growth mechanism was investigated in order to fabricate ZnO nanostructures in a cost effective and scalable manner. Despite the fact that hydrothermal growth of ZnO nanowires (NW) is well documented in the literature [60][61][62] on a variety of rigid substrates including copper, silicon, and glass slides coated with ITO, in this study there has been an attempt of shifting on flexible ones in order for piezoelectric applications. Throughout this chapter it is reported the growth of ZnO NW on flexible kapton films.

Nanowire growth occurs in an aqueous solution containing 30 mM of zinc nitrate hexahydrate ($Zn(NO_3)_26H_2O$) and 30 mM of hexamethyletetramine (HMTA). The role of each substance in the solution is as follows: Zinc nitrate hexahydrate acts as Zn^{2+} ions precursor for ZnO formation. Hexamethyletetramine has two functions, the first is to be the source of OH^- ions, which after their combination with Zn^{2+} form the $Zn(OH)_2$ and

the second is favoring the growth along the NW axis rather than NW diameter. HMTA decomposes upon heating and releases OH^- by the following reactions [63]:

$$(CH2)_6N_4 + 6H_2O \leftrightarrow 6HCHO + 4NH_3 \quad [2.6]$$

$$NH_3+H_2O \leftrightarrow NH_4^+ + OH^- \quad [2.7]$$

The $Zn(OH)_2$ dehydration following according to Eq. 2.5, leads to the final formation of ZnO in NW form. Besides the OH^- generation, HMTA as non-polar material is anticipated in binding to the non-polar side walls of ZnO i.e. [100], [002], and [101]. In this, HMTA inhibits the lateral material growth favouring the longitudinal one [63]. Moreover HMTA was suggested as a pH buffer [64], maintaining the solution pH favorable for NW growth since the rate of HMTA decomposition is independent of the reaction yielding ZnO, Eq. 2.5.

2.4.1 Zinc acetate dihydrate seed layer in hydrothermal growth

Contrary to the electrochemical deposition, the hydrothermal process requires the presence of a seed material onto the substrate which acts as nucleation center for further nanowire growth. The most commonly used ZnO seed layer is zinc acetate dihydrate ($Zn(CH_3COO)_2H_2O$). Upon heating the film on a hot plate zinc acetate dihydrate decomposes and forms solid zinc oxide through the following reactions [65].

$$Zn(CH_3COO)_2\_H_2O \rightarrow Zn(CH_3COO)_2+H_2O \quad [2.8]$$

$$4Zn(CH_3COO)_2+H_2O \rightarrow Zn_4O(CH_3COO)_6+2CH_3COOH \quad [2.9]$$

$$Zn_4O(CH_3COO)_6+3H_2O \rightarrow 4ZnO+6CH_3COOH^- \quad [2.10]$$

$$Zn_4O(CH_3COO)_6 \rightarrow 4ZnO+3CH_3COCH_3 +3CO_2 \quad [2.11]$$

Initially, at around 50 °C, zinc acetate dihydrate begins to lose water [2.8] and becomes anhydrous zinc acetate. As temperature is increased up to 270 °C, several gaseous products (carbon dioxide, acetone, acetic acid) are produced, leaving behind solid zinc oxide on the substrate [2.9] to [2.11]. As water evaporates through heating, the mechanism for the formation of zinc oxide will shift from [2.10] to [2.11]. Hydrothermal growth has been proven to provide highly aligned vertically oriented nanowires and is the most used technique for piezoelectric applications.

In order to deposit zinc acetate dihydrate on the substrate surface, drop casting, ultrasonic vapour deposition, spin coating and inkjet printing techniques were engaged. In this work, zinc acetate dihydrate was spin coated on the substrate surface to form a thick film. The resulting film was quite uniform at the center of the substrate and a bit thicker at the edges. An important parameter at this stage is the concentration of zinc acetate in the seed solution. Very high concentrations resulted in a seed layer prone to crack and flake off the substrate during heating. Such a behavior was addressed to the difference in thermal expansion between zinc

oxide and the substrate, creating stresses at the interface as the seed layer is oxidized. This was observed for rigid ITO-coated glass substrates. Lower concentration seed layers are less likely to flake off since the resulting zinc oxide layers are less dense and not completely connected, leading to lower internal stress and greater relaxation, while maintaining adhesion to the substrate. During the growth, the bases of the nanowires merge, leading to a seed layer which is completely connected.

The resulting NWs grown show a high degree in verticality and density as well. Figures 2.37 (a) and (b) present the ZnO NWs grown on thin alumina substrates using spin coated zinc acetate dehydrate as seed layer at the center and close to the edge respectively. It is obvious that the central part would enhance the vertical growth, while the side parts (where the seed layer is thicker) promote the growth of ZnO NW bundles.

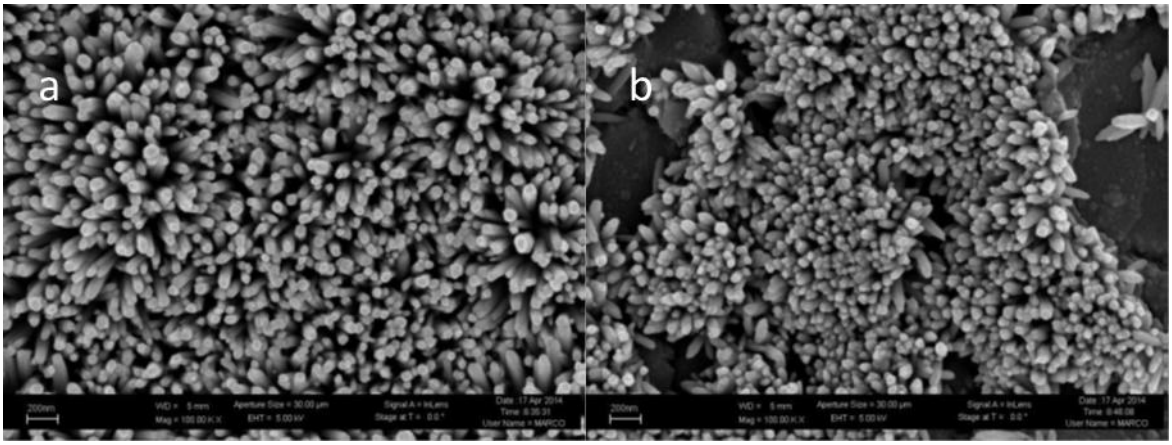

Figure 0.37 ***Hydrothermal growth of ZnO NW on thin alumina substrates. (a) Central part, (b) Close to sample's edge.***

2.4.2 Zinc oxide thin film as seed layer in hydrothermal growth

Another possible candidate to be considered as a seed layer is ZnO thin film. From the previous section it is obvious that the nucleation centers for ZnO NW growth are provided by the ZnO crystals remained on the substrate. A ZnO thin film could perform equally, as it is a polycrystalline material of ZnO. Relevant studies [66] have revealed differences in the growth rate, diameter, density, and surface area of these highly oriented NW which were depended on the seed layer's physical properties. ZnO NWs morphology is strongly influenced by the thickness of the seed layer and the corresponding crystal size. Moreover the surface roughness was reported to be a significant parameter determining the vertical growth of these NWs.

The substrate used in this case was a flexible kapton film. Since these ZnO NWs were grown in order to probe their piezoelectric properties for energy harvesting and sensing applications, the thickness of the seed layer had to be kept minimal, to affect as less as possible the following measurements. To this end, four different ZnO films, used as seed layers, were prepared in order to study the effect of seed layer's thickness in the following ZnO NW growth and presented in Table 2.2. From the previous analysis for ZnO films, the sputtering power was regulated at 150W to offer more planar surfaces. Figure 2.38 presents the ZnO nanowires grown on the ZnO films of Table 2.2 via hydrothermal solution growth for 4 hours.

Table 2. 2 ***Dimensional properties of ZnO seed layer films used for hydrothermal growth.***

Seed layers	Z1	Z2	Z3	Z4
Thickness (nm)	10	50	100	500
Roughness (nm)	2.45	2.52	2.48	2.71

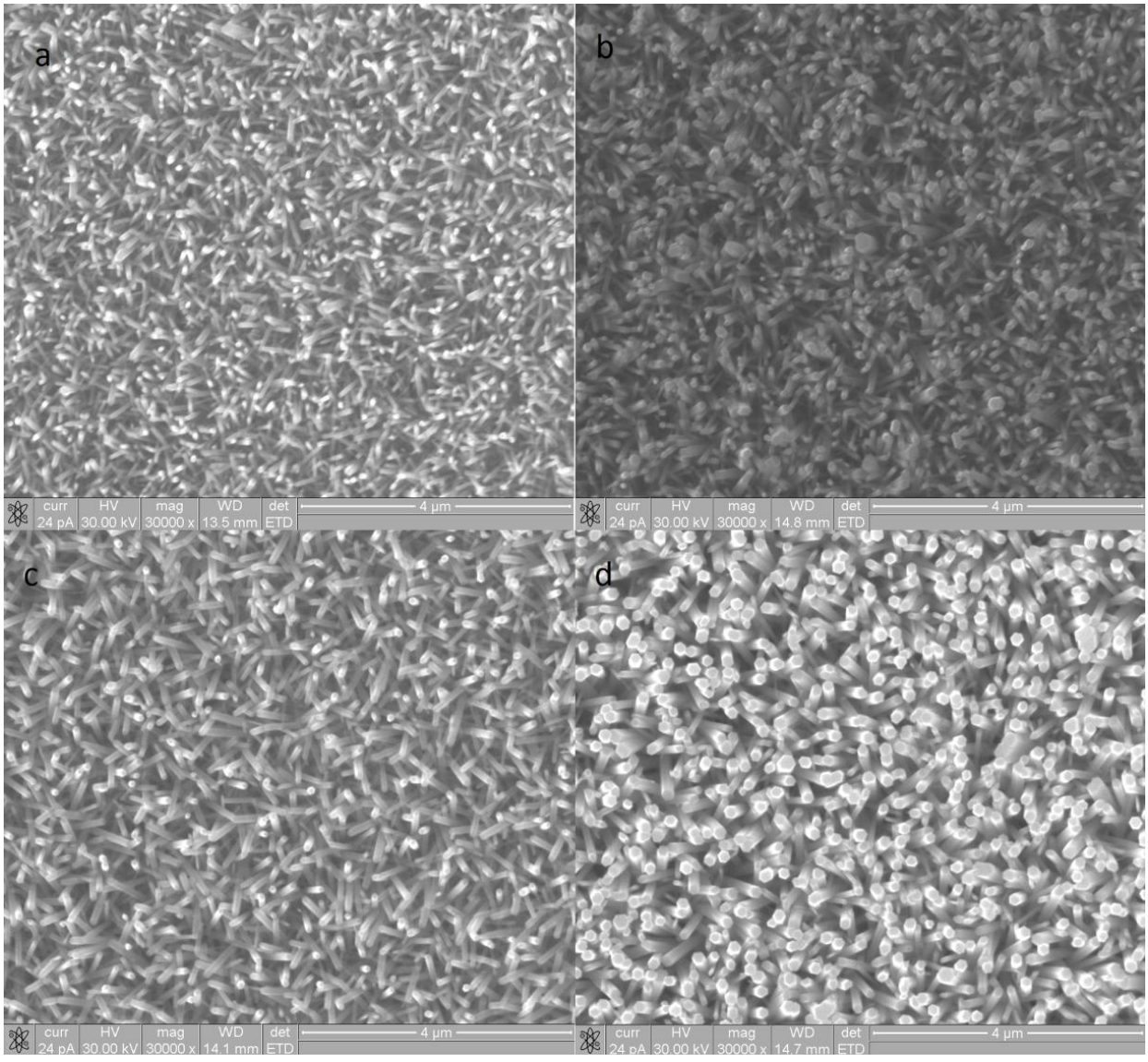

Figure 0.38 ***ZnO NWs grown on ZnO films of various thicknesses (Table 2.2). Seed layers (a) ZnO film 10 nm, (b) ZnO film 50 nm, (c) ZnO film 100 nm, ZnO film 500 nm.***

From the growth results, it can be pointed out that NWs diameter increases along with the seed layer's thickness. Nevertheless, the NWs density follows the opposite path, as in the same area grow bigger structures. The following graph (Fig. 2.39) presents the NW diameter and density dependence on the seed layer's thickness. The right image of Figure 2.39 illustrates the crystal growth direction (XRD analysis on NW came

from Fig. 2.38(c)) to be the (002, the peak is found at 34.22 degrees, JCPDS) c-axis, which was the initial intention.

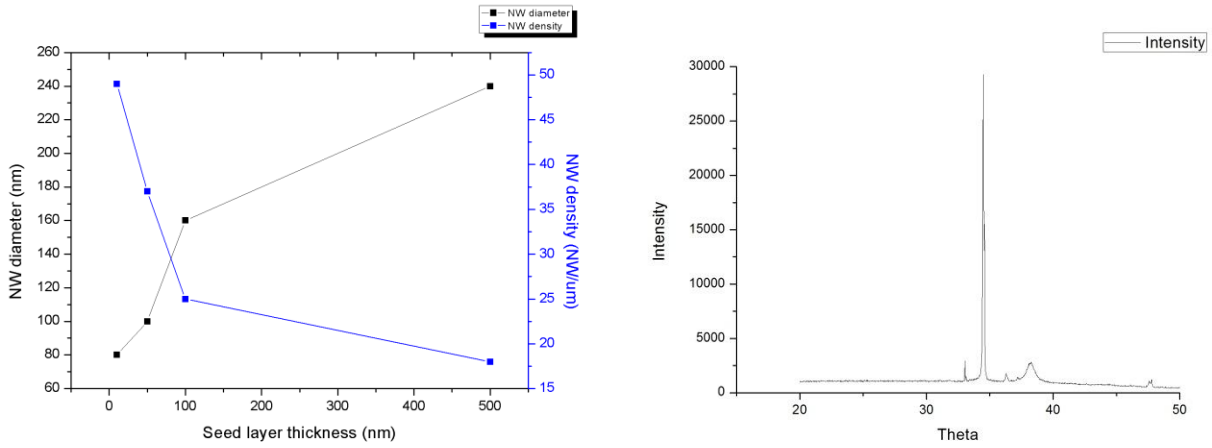

Figure 0.39 ***Left image: NW diameter and density dependence on the seed layer thickness in hydrothermal growth and Right image: XRD pattern, reveals c-axis direction growth.***

Once having exploited the different options in growing ZnO nanostructures, the next step would be to select the most appropriate technique for further piezoelectric and energy harvesting experiments. In this work, electrochemical deposition was chosen for piezoelectric coefficient extraction as it gives highly vertical nanowires, grown along c-axis. The fabrication of energy harvesting devices requires large deposition areas. For this reason hydrothermal synthesis was preferred as it offers better scaling up possibilities in combination with the desired crystal growth direction (c-axis).

Chapter 3

Piezoelectric response and energy harvesting performance of ZnO nanostructures

In this chapter it is reported the piezoelectric response of the abovementioned ZnO nanostructures. Precisely, the piezoelectric properties of electrochemically grown ZnO nanorods are reported by means of their d_{33} piezoelectric coefficient. To this end, piezoresponse force microscopy (PFM) was introduced as it offers high resolution in nanoscale measurements. For successful extraction of d_{33} piezoelectric coefficient, highly vertical nanorods grown along c-axis are essential. This is needed as PFM creates an electric field which is dissipated from a nanorod's top to the bottom. Thus, by align the poling direction with the growth direction and performing the measurement in this manner, reliable and repeatable results are achieved, as well as precise calculation of d_{33} piezoelectric coefficient. Additionally to single nanorod PFM measurements, the piezoelectric response of lab-scale ZnO arrays based devices was evaluated by mechanically induced deformation and simultaneous signal acquisition. All the relevant device's electrodes were done by deposition techniques, carefully avoiding short circuiting. The tests were based on collecting the open circuit voltage coming out from the devices when bent and left to execute a free oscillation. Care was placed to bend the samples in the same way for appropriate comparison purposes. Further, the tests were repeated by connecting one resistance (matched with the internal device resistance) and measuring the power and energy dissipated on that same resistance. By these experiments the accurate quantification of energy harvesting becomes feasible.

3.1 Piezoresponse force microscopy.

PFM measures the mechanical response of a piezoelectric material, when an electrical voltage is applied to the sample with a conductive tip of an AFM. As mentioned in the introduction the piezoelectric effect can be divided in two operating modes (direct and inverse). According to inverse piezoelectric effect the sample expands or contracts locally in response to an applied electrical stimulus, shown in Figure 3.1. When the tip is in contact with the surface, the local piezoelectric response is detected as the first harmonic component of the tip's deflection. The phase φ of the electromechanical response of the surface yields information on the polarization direction below the tip. For c-domains (polarization vector oriented normal to the surface and pointing downward), the application of a positive tip bias results in the expansion of the sample, and surface oscillations are in phase with the tip voltage, $\varphi = 0$. For c+ domains, the response is opposite and $\varphi = 180°$.

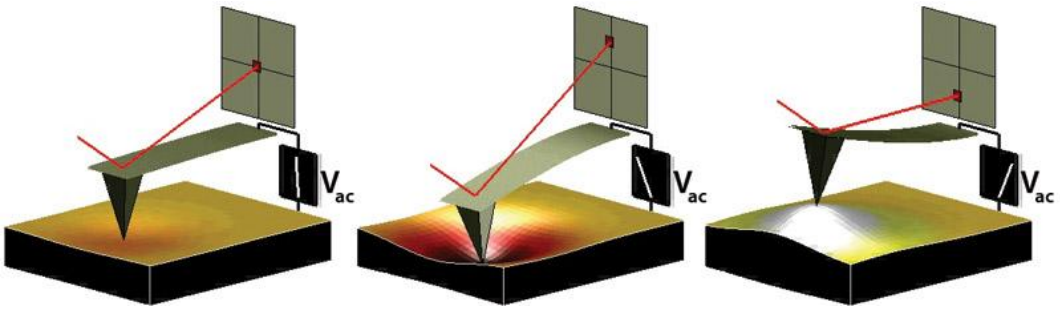

Figure 0.1 ***Depiction of PFM operation. The sample deforms in response to the applied voltage. This voltage, in turn causes the cantilever to deflect, which can then be measured and interpreted in terms of the piezoelectric properties of the sample*** **[67]*.***

PFM requires detection of small tip displacements induced by relatively high amplitude, high frequency voltages measured at the same frequency as the drive. Any instrumental crosstalk between the drive and the response will result in a virtual PFM background that can easily be larger than the PFM response itself, especially for weak piezo materials. For this reason minimizing crosstalk between the driving voltage and the response is the most favored way of achieving correct PFM images.

3.2 PFM measurements on ECD ZnO nanorods.

The relationship between the strain and the applied electric field (inverse piezoelectric effect) in piezoelectric materials is described by a rank-3 tensor, shown in Figure 3.2. The 'd' matrix gives the piezoelectric coefficients in diverse modes. As known a material can grow along x, y and z (or c) axes. The subscripts appeared in 'd' matrix represent the mechanical response at a given axis as a result of an electric field implementation across one of the rest. The most important component of the 'd' matrix is the d_{33} coefficient, for typical "vertical" PFM. Specifically, the d_{33} piezoelectric coefficient is the one that couples directly into the vertical motion of the cantilever when an applied electrical field is imposed across that same direction. In the case of ZnO material it happens to be the most favored piezoelectric component as well.

$$\begin{bmatrix} D_1 \\ D_2 \\ D_3 \end{bmatrix} = \begin{bmatrix} d_{11} & d_{12} & d_{13} & d_{14} & d_{15} & d_{16} \\ d_{21} & d_{22} & d_{23} & d_{24} & d_{25} & d_{26} \\ d_{31} & d_{32} & d_{33} & d_{34} & d_{35} & d_{36} \end{bmatrix} \begin{bmatrix} T_1 \\ T_2 \\ T_3 \\ T_4 \\ T_5 \\ T_6 \end{bmatrix} + \begin{bmatrix} \varepsilon_{11} & \varepsilon_{12} & \varepsilon_{13} \\ \varepsilon_{21} & \varepsilon_{22} & \varepsilon_{23} \\ \varepsilon_{31} & \varepsilon_{32} & \varepsilon_{33} \end{bmatrix} \begin{bmatrix} E_1 \\ E_2 \\ E_3 \end{bmatrix}$$

T_1 = normal stress in x direction

T_2 = normal stress in y direction

T_3 = normal stress in z direction

T_4, T_5, T_6 = shear stresses

D : $F/m * V/m = C/m^2$

T : N/m^2

d : C/N or m/V

Figure 0.2 ***Analytic equation of inverse piezoelectric effect. The ' d' matrix represents the piezoelectric coefficients associated in different modes.***

As it was understood from the early beginning of piezoelectric phenomena, the crystallographic orientation of materials plays a decisive role in the piezoelectric properties [68]. According to the definition of the piezoelectric effect, all components of the piezoelectric tensor should vanish in crystals possessing the center of inversion symmetry. That lack of a center of symmetry in ZnO's crystal unit cell is responsible for any piezoelectric behavior present on this material.

As seen in Figure 3.2, 'd' matrix consists of few different components. The number N of independent components is a third-rank tensor. In principle, it may be as large as $3^3 = 27$. The piezoelectric tensor, however, can have maximum of 18 independent components because $d_{ki\,j} = d_{k\,ji}$ owing to the symmetry of the stress and strain tensors ($T_{ij} = T_{ji}$, $S_{ij} = S_{ji}$). The case of N = 18 corresponds to triclinic crystals of class 1. In crystals with higher symmetry, the number N further reduces. This feature follows from the Neumann's principle: The symmetry elements of any physical property of a crystal must include the symmetry elements of the point group of this crystal. As a result, in tetragonal crystals of the 4mm and hexagonal of the 6mm symmetry, there are only three independent components, and the piezoelectric effect is described by the matrix shown in Figure 3.3.

a)

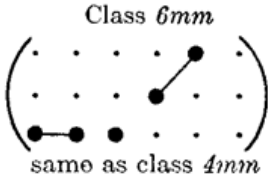

b)

$$\mathbf{d} = \begin{bmatrix} 0 & 0 & 0 & 0 & -11.34 & 0 \\ 0 & 0 & 0 & -11.34 & 0 & 0 \\ -5.43 & -5.43 & 11.37 & 0 & 0 & 0 \end{bmatrix} pC/N$$

Figure 0.3 ***(a) 'd' matrix in 6mm class materials, (b) theoretical piezoelectric coefficients in ZnO bulk form.***

Figure 3.3 b) clearly demonstrates d_{33} piezoelectric coefficient to be the highest in ZnO bulk material. The choice of using PFM to perform piezoelectric measurements was done for the two previously analyzed reasons:

- PFM's excellent resolution in vertical mode, the one associated with d_{33} coefficient.
- ZnO's d_{33} highest piezoelectric coefficient.

3.2.1 PFM measuring process

Before any actual measurement a calibration procedure takes place on the instrumentation which guarantees the reliability of the results. Calibration requires the measurement on a reference material of known piezoelectric properties. As the cantilever sensitivity may change with frequency, it is important to obtain a calibration factor at the measurement frequency. As a reference, a sample of 100 nm thick epitaxial lead zirconate titanate (PZT) thin-film deposited on an electrically-conductive substrate was used. The reference sample contains a series of top electrodes which have been characterized using a traceable interferometric method as described by Lepadatu *et al.*[69]. For the top electrodes on the reference sample an effective d_{33} coefficient equal to 48 ± 2 pm/V was obtained from interferometry measurements. Thus if $d_{PZT,mV}$ is the raw cantilever displacement amplitude measured at 1 V driving amplitude on the reference electrode and $d_{ZnO,mV}$ is the raw measurement on ZnO then the vertical surface displacement in pm is given by $d_{pm} = d_{ZnO,mV} \times 48/d_{PZT,mV}$.

Individual NRs were measured by first locating them using a tapping mode AFM scan and then centring on the NRs using precise offsets on the piezo-driving stage. As described formerly [70], (002) is the most favoured piezoelectrical axis of ZnO. A quantitavive piezoelectric measurement across the c-axis requires an external polarization, as well as simultaneous strain monitoring across the same direction. The former characterization mode lets the extraction of the d_{33} effective piezoelectric coefficient. Figure 3.4 shows a schematic representation of PFM measurement on verticaly grown ZnO NRs. PFM tip contacts the NR's surface at one specific point, precisely where the measurement is performed. Evidently, any relevant movement is partially inhibited by local clamping effects [71]. The effective d_{33} value is calculated from the displacement of the cantilever tip and the voltage as shown in Eq. 3.1 where Δt is the vertical displacement and V is the applied voltage amplitude. The actual d_{33} value for the material is related to the measured effective d_{33} but is potentially affected by off-centre bending modes, and constraints due to substrate effects [72] and neighbouring NRs.

$$d_{33}(eff.) = \frac{\Delta t}{V} \qquad [3.1]$$

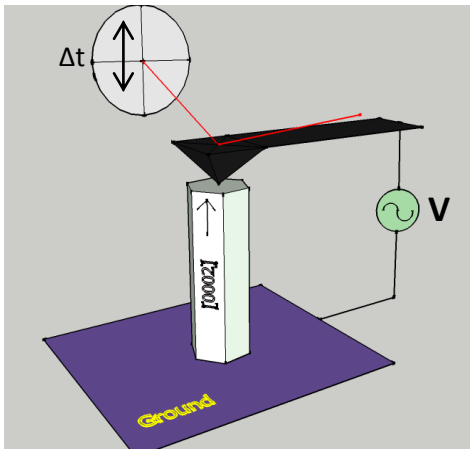

Figure 0.4 Schematic representation of PFM measurements on ZnO NRs. An external electrical (AC) field polarizes the NR, which expands or retracts accordingly. This movement is measured by the instumentation's photodetector and converted to an electrical signal.

The electric field is applied along the whole length of the nanorod (c-axis) by placing the PFM tip at the centre of the upper face of the nanorod while keeping the bottom electrode (Au) grounded. The NR c-axis orientation and vertical growth determine the d_{33} piezoelectric constant. In this way the tip's displacement amplitude (pm) is accurately evaluated as a function of driving voltage amplitude (V).

3.2.2 PFM results

Figure 3.5(a) shows a tapping mode AFM scan of a region with ZnO NRs – from this image a mean NR diameter of about 150 nm was estimated. For these measurements a medium-stiffness cantilever with measured constant k = 8.8 N/m, nominal tip diameter 20 nm, and Pt-Ir metallic coating was used. The piezo-response was measured using a contact force of ~80 nN.

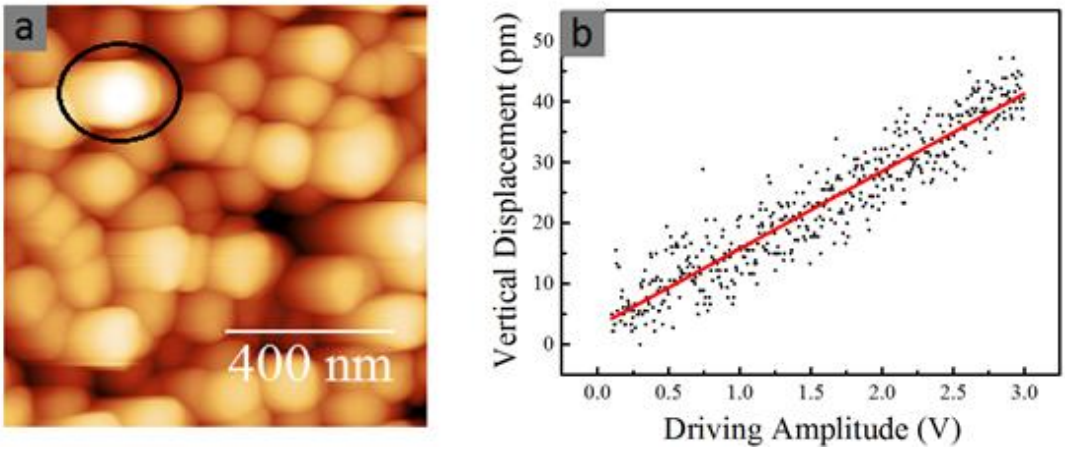

Figure 0.5(***a) Tapping mode AFM image on vertically grown ZnO NRs. PFM measurements were performed on the most prominent NRs, found in bright white colour. (b) PFM mode voltage amplitude ramp on an individual ZnO NR showing the calibrated vertical piezo-response.***

A typical voltage amplitude ramp on individual ZnO NRs is shown in Figure 3.5(b). The measurement voltage window was set from 0.1 to 3 V. As expected from theory, the displacement response is linear with the driving voltage amplitude. The excitation voltage frequency was 40 kHz and the response found to be constant with the driving frequency up to 100 kHz. Below 40 kHz the signal to noise ratio becomes smaller, leading to a non-reliable measurement. The effective d_{33} value of Eq. 3.1 is obtained using a linear fit of the calibrated displacement-amplitude ramp as shown in Figure 3.5(b). These measurements were repeated on more than 50 NRs in different regions of the sample. The piezoelectric response was highly reproducible with small variation in the measured d_{33} (effective) value. The distribution of d_{33} values was found to be well described by a normal distribution with a mean value of 11.8 pm/V and standard deviation of 2.2 pm/V, as shown in Figure 3.6.

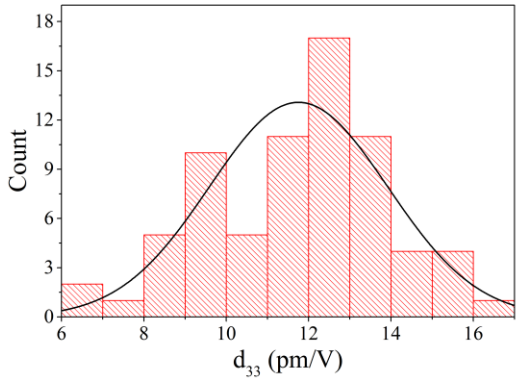

Figure 0.6 ***Distribution of d_{33}effective coefficient, obtained on numerous ZnO NRs*.**

The mean d_{33} value for the NRs is 19% larger than the typical value measured for bulk (9.93 pm/V) as reported elsewhere [73] and from the theoretical molecular dynamics predictions [74][75] - where it was

demonstrated that ZnO NW of diameters larger than 4nm do have bulk-like piezoelectric properties. This outcome is of high interest from application standpoint, indicating that ECD ZnO NRs would perform ~20% better than their bulk counterpart if used on piezoelectric applications. Indeed, since NRs exhibit lower deformation energies than bulk [74], lower mechanical energies would induce their deformation and final polarization. Based on this fact, ECD ZnO NR arrays are promising candidates to replace bulk piezoelectric devices.

Table 3.1, is a synopsis of the d_{33} (effective) values for 1D ZnO nanostructures of similar types reported in the literature measured by similar nano-probe techniques. As apparent from this table, the ECD-fabricated nanostructures, result of this study, exhibit larger piezoelectric response of about 60% with respect to the hydrothermal-nanostructures, and of about 40% if compared to the template-assisted ones. The latter is among the most commonly used techniques to grow such structures. More recently, Broitman *et al.* demonstrated a d_{33} piezoelectric coefficient equal to 9.2 pm/V - value still 30% smaller than ECD's - in similar nanostructures but fabricated by an aqueous chemical method [76]. On the other hand, the d_{33} coefficient measured here is notably smaller if compared to values reported by Zhao *et al.* for thermally evaporated [0001] ZnO nanobelts. The PFM response at high frequencies would generally result in dynamic cantilever stiffening. Hence, the PFM measurements obtained in this way contain less contribution from the electrostatic terms compared to the electromechanical response [77]. The abnormally large values (also controversial to DFT theoretical calculations) reported in [78] are unlikely to be connected only with the piezoelectric effect and may include an electrostatic contribution which is reduced by the frequency increase. Instead, the fairly stable measured responses across the whole range of frequencies (40-100 kHz) obtained hby ECD NR grant minimum contribution of such effects, attributing the full output response to ZnO's piezoelectricity.

By PFM the vertical displacement is accurately monitored. Bending or other complex deformation of the NRs will result in effective piezoelectric coefficients that differ significantly from the previous values. Bending modes will also have relatively low characteristic frequencies (compared to longitudinal compression), resulting in frequency dependence of the effective coefficient and large variation from one rod to another. The reason of performing PFM measurements on ECD nanorods is their high verticality. This means that these complex deformations will have only a little influence on the final measurement [79]. This is supported by the lack of frequency dependence on these measurements, the small variation in measured effective d_{33} coefficient and the closeness to the expected bulk value. The fact that the mean value of the d_{33} coefficient is larger than bulk may be also attributed to deviations from verticality of the NRs, resulting in some small degree of bending mode, yet not enough to introduce a strong frequency dependence.

Table 3. 1 Comparison between *differently grown ZnO nanostructures,* in terms of their d_{33} *(effective) piezoelectric coefficients.*

Growth technique	*d33 piezoelectric response (pm/V)*
Electrochemical deposition	11.8
Hydrothermal [80]	4.41
Template assisted, Vapour diffusion deposition [81]	7.5
Aqueous chemical growth [76]	9.2
Thermal evaporation [78]	14.3-26.7
ZnO bulk [73]	9.93

3.3 Energy harvesting

3.3.1 Device fabrication

In the previous chapter, different synthesis methods for preparation of ZnO nanostructures were reported. Moreover the piezoelectric nature of electrochemically deposited ZnO nanorods was expressed in the first part of chapter 3, by measuring their d_{33} piezoelectric coefficient. However, the transition from the bare material to a functional piezoelectric device requires the proper interconnection between the micro and the macro-world.

The procedure followed in order to fabricate piezoelectric devices based on ZnO nano-materials can be described by Figure 3.7. As shown below, the whole process starts from the appropriate substrate selection. Restrictions faced at this point are related with the performance of the particular substrates during the ZnO growth mechanism (if chemical methods are used) like temperature resilience. In this study two different materials have been tested as supporting substrates, SiOx and kapton. Since none of them is conductive, the following step includes the bottom electrode fabrication, which will be later used for connection with external instruments (oscilloscope) for performing energy harvesting tests. For this scope gold was chosen, as being one of the best and more stable conductors available. In the same time Au sputtering gives a perfect planarity on the substrate, which is important in NW growth. Form this point ZnO nano-materials growth takes place as it is described in chapter 2.

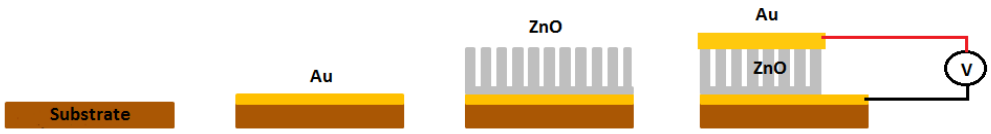

Figure 0.7 ***Principle fabrication steps for piezoelectric devices development, based on ZnO nano-materials.***

The current sub-chapter reviews the electromechanical performance of novel devices based on electrochemically deposited ZnO nanorods, hydrothermally grown ZnO nanowires and physically vapor deposited ZnO thin films. The second contact with the piezoelectric material is done again by sputtering a thin layer of Au on the top of the nanostructures. For the case of ZnO thin film this approach should be rather facile, however for ZnO NW or NR the process gets more complex. The NR porous structure cannot block the penetration of Au particles in order not to arrive at the bottom electrode. In this way short-circuit is created at the two ends of the materials which does not allow the achievement of any electrical measurement.

In order to overcome this difficulty, between the active material (ZnO) and the Au electrode, a thin layer of PMMA 2% was spin coated (1300 rpm) on ZnO's tops. PMMA solution was prepared in house by mixing solid PMMA with Anisol in a concentration of 1%, 2%, 5% and 10%. The final solution was left to stirring for several hours in room temperature until a uniform transparent colour was achieved. From the aforementioned

concentrations, the one finally chosen was PMMA 2%, as during the spin coating process offered the smoothest result on the film. Smaller PMMA concentrations would lead to a low viscosity film which might penetrate inside the nanostructures with much possibility of gap creation. The process requires the repetition of several spin coating events in order to securely encapsulate the active piezoelectric materials. On the other hand higher concentrations would lead to a thicker film formation with increased resistance, which could misinterpret the final piezoelectric results, by introduction of electrostatic forces. The previous approach for piezoelectric device fabrication is shown in Figure 3.8. In this figure one of the devices was dismantled for SEM image characterization and its micrograph is presented in Figure 3.9.

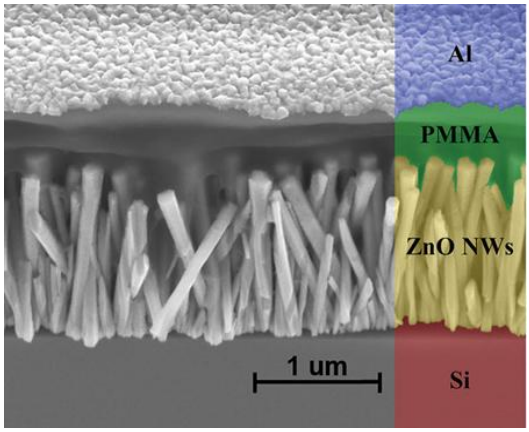

Figure 0.8 ***Basic layout of piezoelectric devices consisted of ZnO NW arrays*** **[82].**

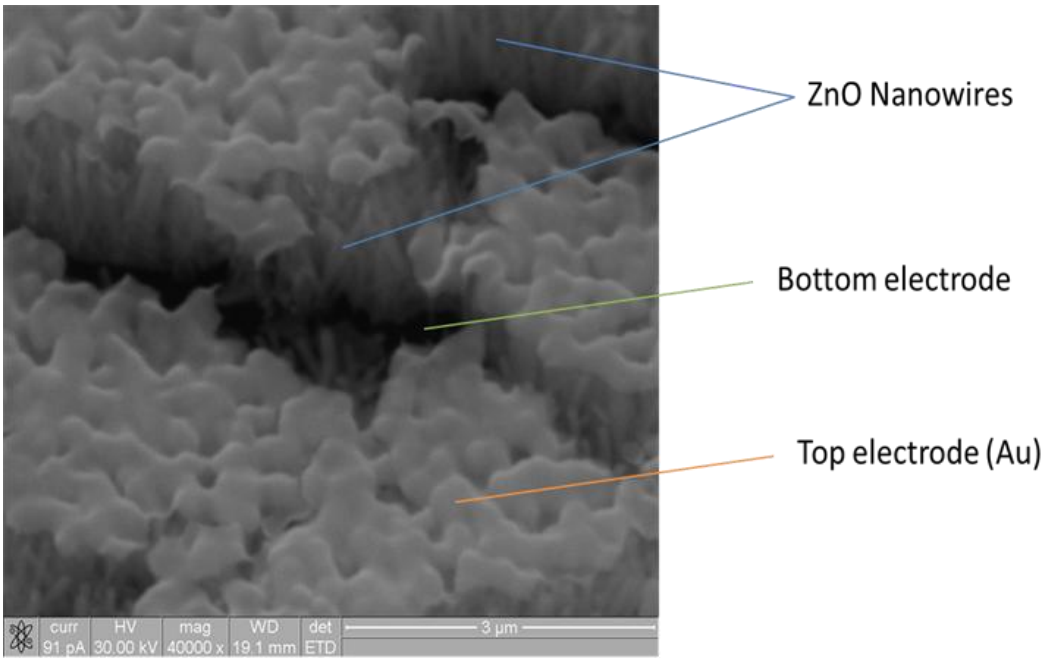

Figure 0.9 ***Actual device fabricated in CRF's laboratories clearly shows the active layer of ZnO nanowires as well as the bottom and top electrodes.***

3.3.2 Piezoelectric tests on ZnO NRs grown electrochemically on rigid substrates

Once the devices are assembled, the following step involves the piezoelectric performance characterization. For this scope, mechanical deformation of the active layer is requested. The deformation should be able to polarize the ZnO NRs and create a piezoelectric voltage output on the device's ends. Should these two ends be electrically connected with an oscilloscope, the acquisition and quantification of the former output becomes feasible. The previous testing characterization is schematically described in Figure 3.10 and the actual testing layout in Figure 3.11.

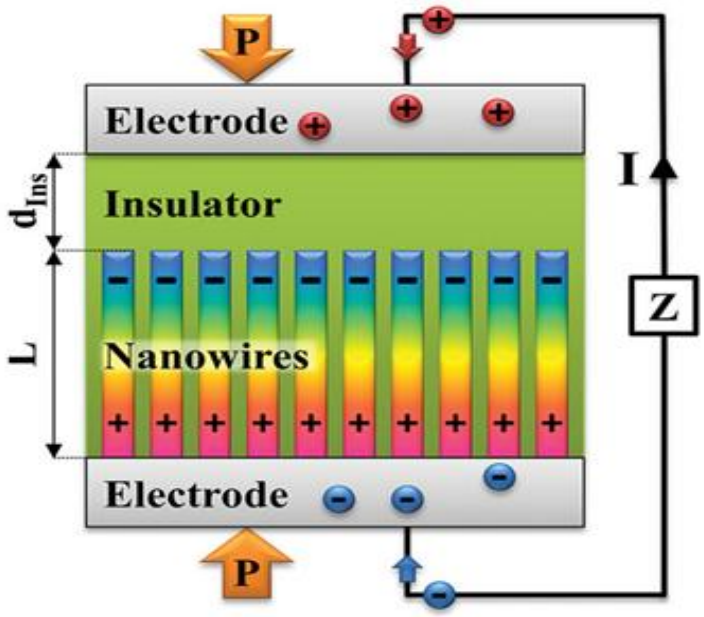

Figure 0.10 ***Schematic representation of piezoelectric testing principle.***

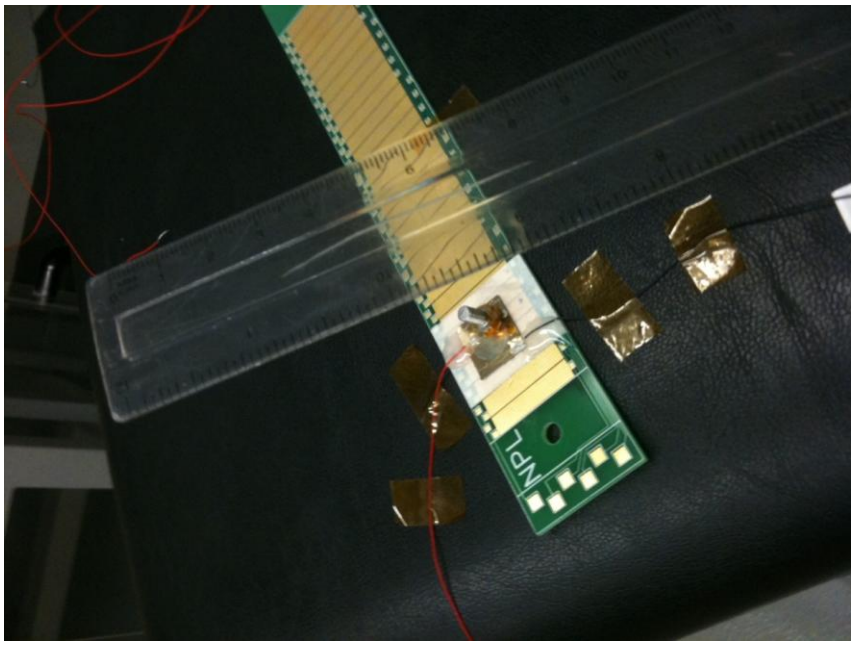

Figure 0.11 ***Layout of the direct piezoelectric experiment.***

Performance tests on rigid substrates were performed by external force application on the top electrode and by simultaneously collecting the generated signal. The force was mechanically applied by a plastic ruler (insulator, Figure 3.11), which was bent up to a specific point and left to reflect back by itself. The movement of the ruler was terminated upon an electrically insulated bolt (in order to avoid any electron exchange that could affect the measurement) and the kinetic energy was converted to mechanical force on the top electrode.

Before the actual testing, the mechanical force created by the ruler was measured using a potentiometer. Several similar repetitions were done in order to arrive at a mean force value applied on the electrode. Figure 3.12 shows that the mean applied force on the top electrode after some repetitive measurements was around 350 mN.

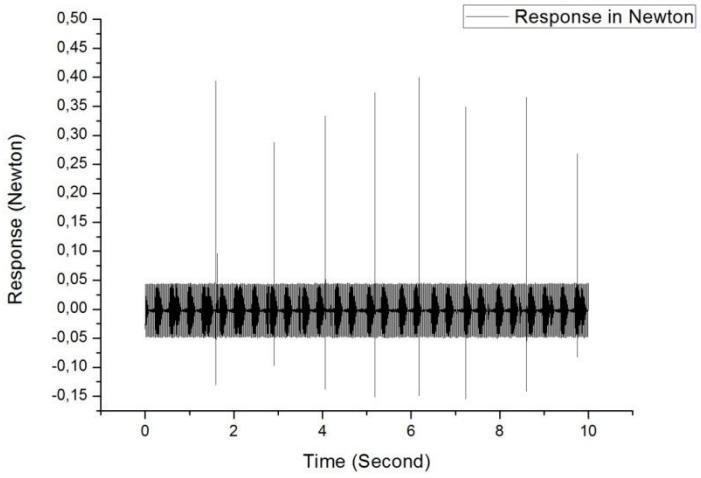

Figure 0.12 Measurement of applied force*, coming from the bent ruler*.

Every time that the ruler was applying force on the device, an output voltage peak was being collected. The previous observation was associated with the piezoelectric effect, which origins from the ZnO NRs. Three different devices were tested for their piezoelectric performance. The difference lies in the dissimilar internal resistances measured after the whole fabrication. Even if the fabrication steps were comparable between them (2 hours of electrochemical deposition), the final piezoelectric result was proven to be rather different. Table 3.2 states the diversity in their internal resistances.

Table 3. 2 ***Internal resistances of the three different samples.***

Sample	DP_1	DP_2	DP_3
Resistance (kΩ)	160	3,17	111

In Figures 3.13, 3.14 and 3.15 are shown the piezoelectric outputs of the three aforementioned devices measured in open circuit topology, V_{oc}. A clear sharp peak is observable each time the mechanical force is applied on the device for all cases. Despite the fact that the force was maintained almost at the same level, the piezoelectric response did not follow that trend. It can be conceived that even a slight difference in the force applied to the device could lead to diverse piezoelectric response. The general rule states a smaller force to generate smaller peaks and the contrary. For comparison purposes, only the highest peaks each time will be considered.

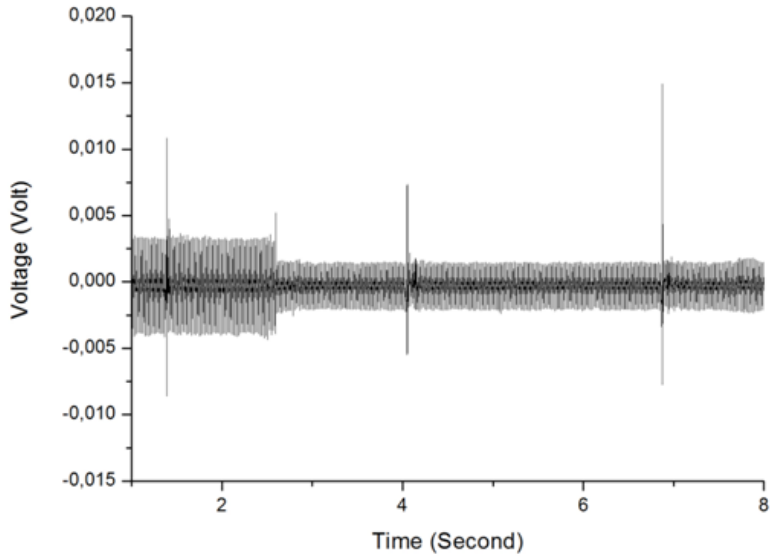

Figure 0.13 ***Open circuit piezoelectric response of DP_1 device.***

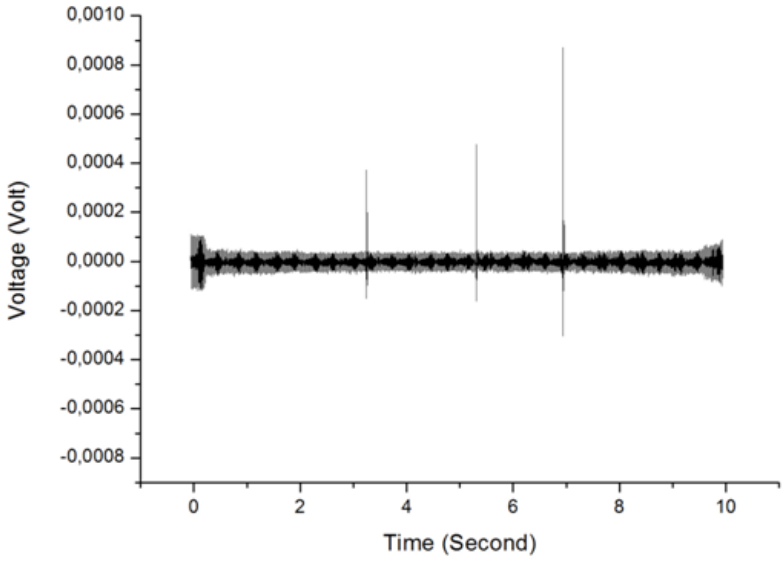

Figure 0.14 ***Open circuit piezoelectric response of DP_2 device.***

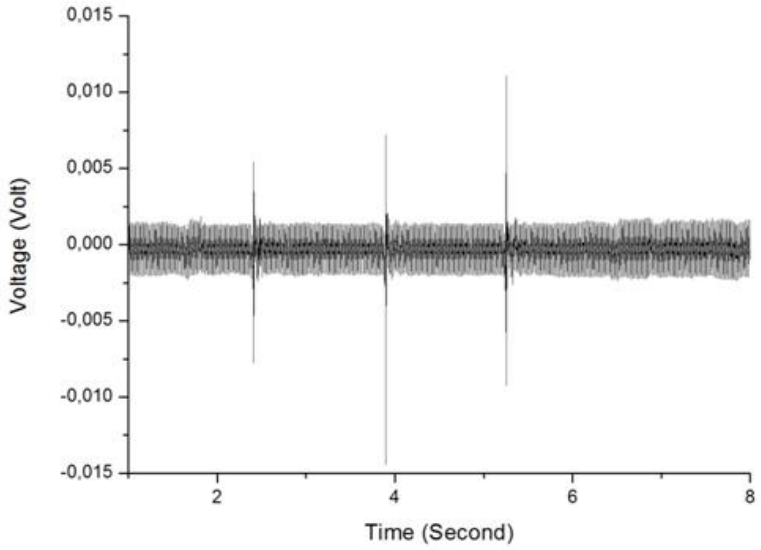

Figure 0.15 ***Open circuit piezoelectric response of DP_3 device.***

From the previous graphs it is seen that the highest piezoelectric output is addressed to DP_1 device which has the highest equivalent resistance as well. Then follows DP_3 and finally DP_2 devices. As a result, it is demonstrated that the higher the internal resistance of the overall device, the higher the piezoelectric generated voltage. The previous finding is in accordance with other studies [83], where it was demonstrated that the value read from the data acquisition system (ex. oscilloscope) mainly depends on the screening rate of the generated polarization from the external circuit. More specific, when ZnO gets compressed, polarization charges develop at the surface as shown in Figure 3.10. Once unscreened, these charges lead to the creation of a depolarization field, E_{dep}, which drives the movement of screening charges both within the material and at the contacts. If a metal contact is formed between the ZnO and the external circuit, the polarization charges can be screened by the free electrons in the metal in a very fast rate. This effect has been described and studied extensively for ferroelectric materials and occurs extremely rapidly due to the high availability and mobility of carriers at the metal surface [84]. It is for this reason that piezoelectric energy harvesting devices using Ohmic contacts do not generate a voltage, as the polarization charges are screened so rapidly by movement of free electrons from the metal that the depolarization field does not develop in the material and no voltage is measured externally. The Schottky contact between the metal (Au) and the semiconductor is believed to have aided in the measurement acquisition. Moreover the screening effect happens also internally, from the free-carriers found in ZnO. As a result a conductive material would generate less voltage compared to a resistive one.

From the previous analysis, a higher internal resistance is expected to decrease the time of screening, allowing more time for piezoelectric voltage generation. This undoubtedly explains why the DP_1 is able to give higher voltage peaks when compared with the other two devices.

By further analyzing the V_{oc} peaks, the piezoelectric generation mechanism is revealed. In particular seen in Figure 3.16, at the time of force implementation a sharp negative voltage peak is observed, resulting from the initial polarization of ZnO arrays. The negative polarization lasts for a few milliseconds and then returns to zero. This is the result of the fully screened piezoelectric polarization from the circuit. After almost 300 milliseconds another voltage peak having opposite polarization and about the same absolute value is detected. This is a common behavior in piezoelectric materials. After the initial polarization, when the applied force is taken away, the material returns to its initial position, by depolarizing itself and the free carriers participated in screening of the piezoelectric field return to their initial position by giving a positive peak.

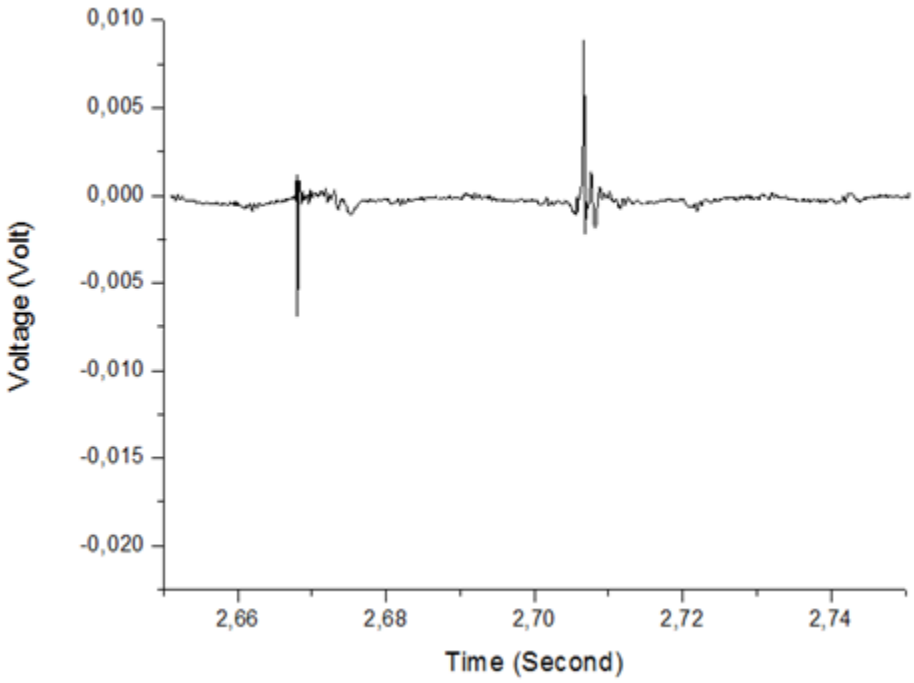

Figure 0.16 ***Piezoelectric peaks analysis by zooming in the time scale. A sharp negative, followed by a positive peak are evidently shown. This behavior is strictly associated with the piezoelectric phenomena.***

The above mentioned way of performing piezoelectric tests was proven to be high valuable, as the generated voltage is clearly associated with the polarization of the active material. Moreover the acquired results were quite reproducible for all mentioned devices, which enhance their reliability. Though the method being trustworthy, the generated voltage peaks were rather narrow (very small duration), which in fact limits the implementation of this kind of setup (rigid substrates) for energy harvesting applications.

3.3.3 Piezoelectric tests on ZnO NWs grown hydrothermally on flexible substrates

Another case study for energy harvesting applications is the use of flexible substrates instead of rigid ones. It has been proposed that the deformation created by a flexed ZnO nanowire should by its own turn, polarize the material as would have been done by external force implementation.

In this case kapton foils were introduced as supporting substrate for the hydrothermal growth. The novel piezoelectric devices based on ZnO NWs were prepared in similar ways by following the previously described steps (Fig. 3.7) on Au coated kapton film of 2.5x5 cm^2 (shown in Figure 3.17). Piezoelectric tests are performed by mounting the flexible devices on a stable basis and bending them in the same manner (Fig. 3.18).

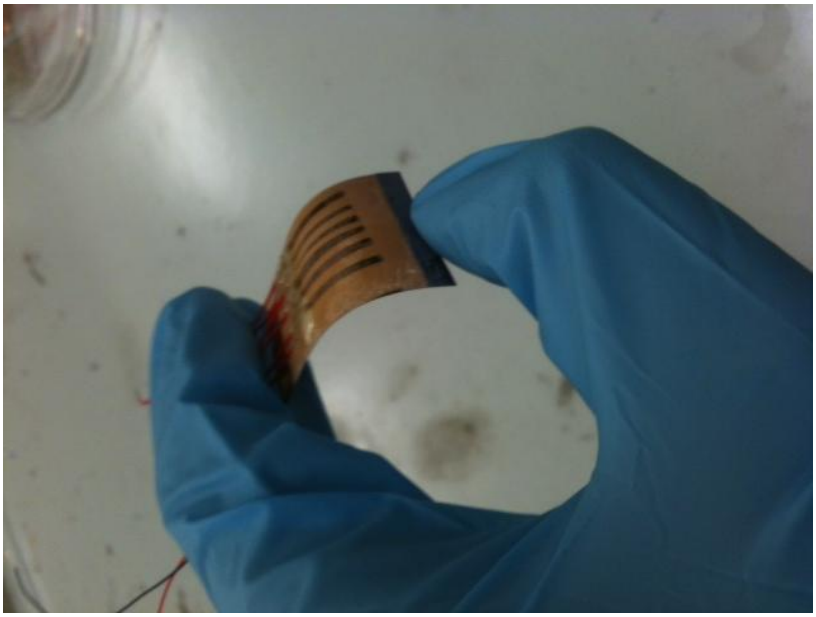

Figure 0.17 ***Piezoelectric generator based on ZnO nanowires, fabricated on flexible Au coated kapton film. The dark stripes, represent the top electrodes.***

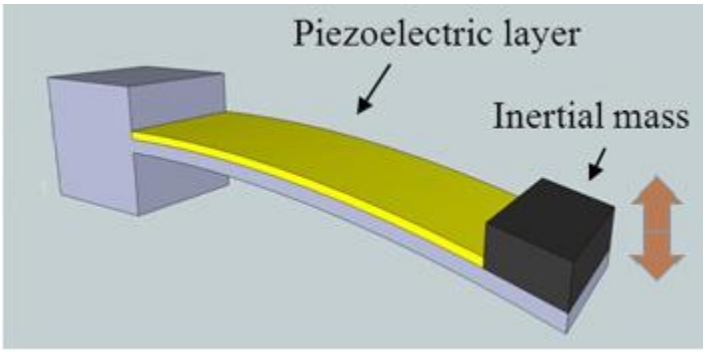

Figure 0.18 ***Piezoelectric testing principle, based on a bending cantilever. By making two contacts (bottom and top) on the piezoelectric active layer, the piezoelectric response is acquired.***

The data acquisition is done in real time by electrically connecting the bottom and top electrodes to an electronic oscilloscope. The cantilever bending was triggered mechanically by deformation until 45˚ and then left to move back and forth by its own eigenfrequency. As in the previous case of rigid substrates, piezoelectric peaks were observed each time the cantilever was bent.

The performed studies include the measurement of the dissipated energy across an electrical load to quantify the energy harvesting properties of the fabricated devices. This investigation was based on the dimensions of the ZnO NW. For this reason two novel nano-generators (as they are commonly found) were built by controlling the growth time during the nanostructures' synthesis. Hydrothermal growth was employed for the ZnO synthesis as described in section 2.4.2. The differently prepared devices are named H3 and H6 which stand for three and six hours of growth respectively, as an attempt to double their actual size. At the same time of the ZnO growth on the devices, another reference sample was introduced in a similar chemical bath in order to be used for characterization purposes. The reference sample, shown in Figures 3.19 and 3.20 was prepared in such a way of allowing the comparison between the two different growth conditions.

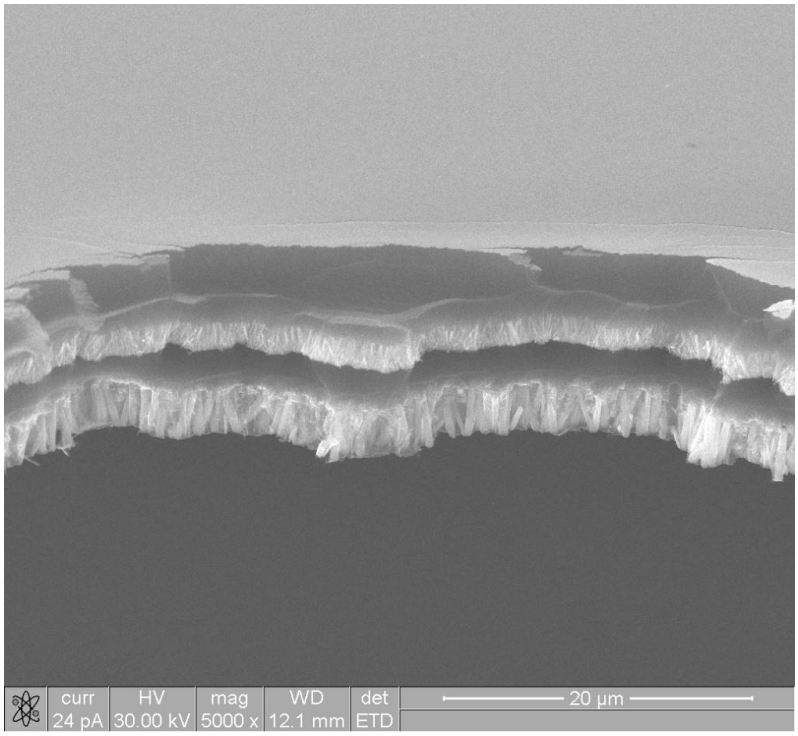

Figure 0.19 ***Reference sample showing the size difference in NWs used in H3 (upper layer) and H6 (lower layer) devices.***

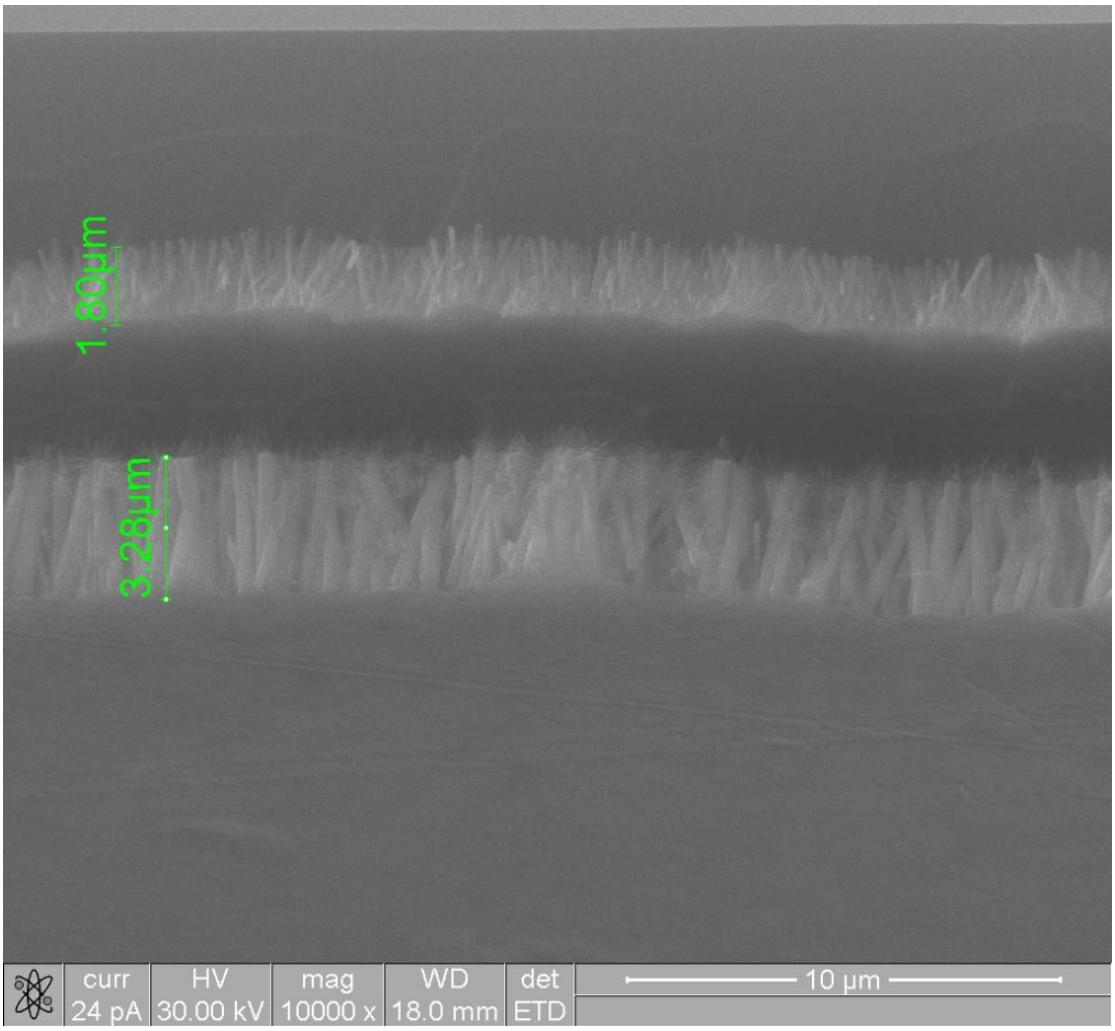

Figure 0.20 ***Reference sample, higher magnification image combined with NW size measurement.***

The upper layer in Fig. 3.20 was used in the first sample (H3) while the lower in the second (H6). Apart from the two aforementioned devices based on ZnO NWs, another one made by ZnO thin film, having thickness of around 1 μm was prepared in order to compare their performances in mechanical energy harvesting. Table 3.3 describes the preparation details regarding the ZnO nano-materials, used in the three mentioned nano-generators.

Table 3. 3 ***ZnO active layer properties used in nano-generators.***

Code name	***H3***	***H6***	***TF***
ZnO active layer	Hydrothermally grown NW	Hydrothermally grown NW	PVD sputtered thin film
Active layer thickness (μm) (ZnO thickness + PMMA encapsulation)	3.5	4.28	2
Resistance (MΩ)	40	10	1
Active area (cm^2)	0.12	0.18	0.4
Active volume (cm^3)	$4.2*10^{-5}$	$7.7*10^{-5}$	$8*10^{-5}$

The proper evaluation of the harvested energy requires an external connection with an electric load and simultaneously monitoring of the dissipated voltage across that load. Equation 3.2 gives the power consumed on that resistance and by integrating that value over time, the quantification of energy harvested is achievable (Eq. 3.3).

$$P = \frac{V^2}{R} \qquad [3.2]$$

$$E = \int_{-\tau}^{+\tau} P = \int_{-\tau}^{+\tau} \frac{V^2}{R} \qquad [3.3]$$

According to the optimal power transfer theorem, the external load should offer the same impedance value as the internal resistance of the device. The selection of the connected resistances was done based on this principle and the results regarding the energy harvesting performance under bending are shown in the following figures.

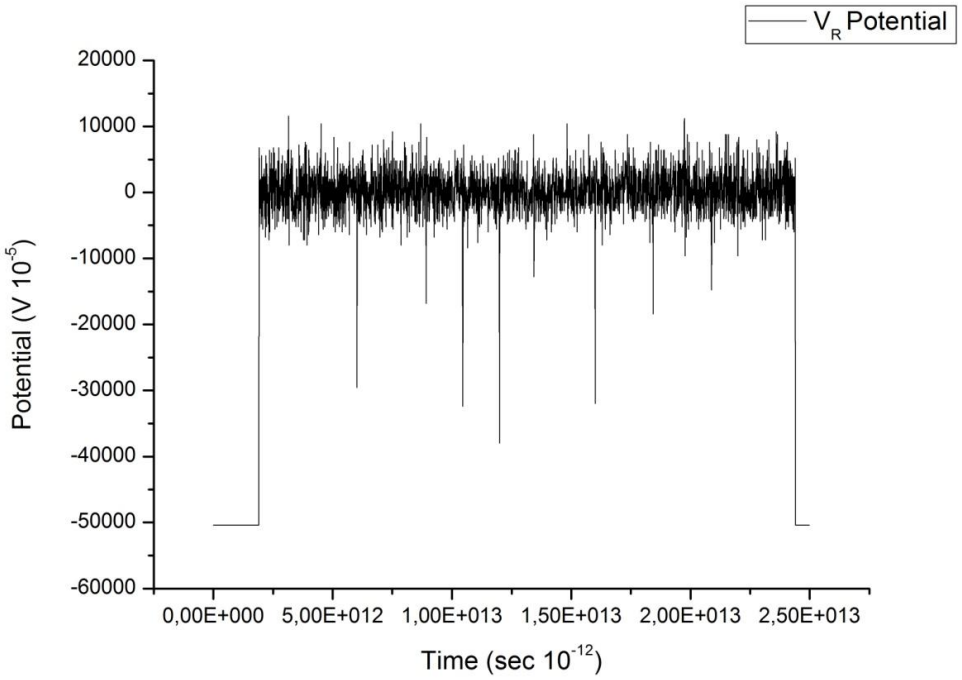

Figure 0.21 ***H3 device's energy harvesting performance.***

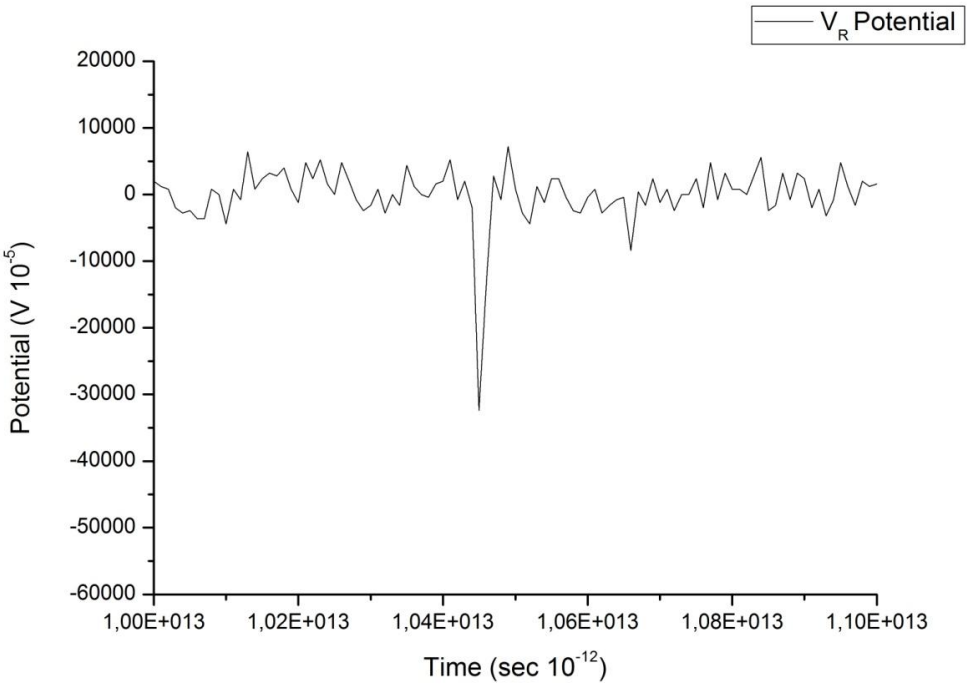

Figure 0.22 ***H3 device's detailed energy harvested peak.***

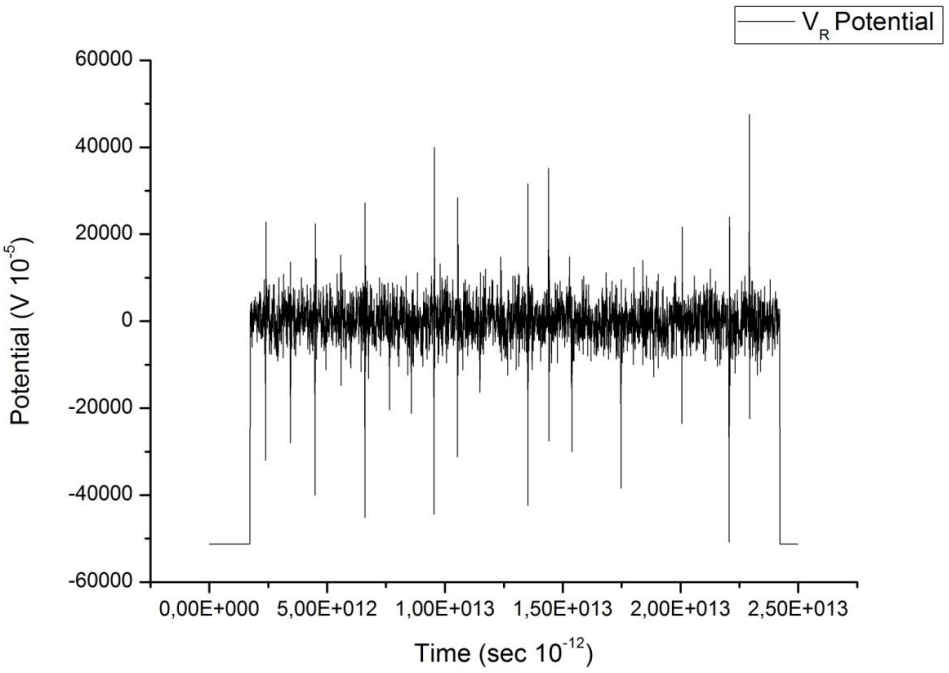

Figure 0.23 ***H6 device's energy harvesting performance.***

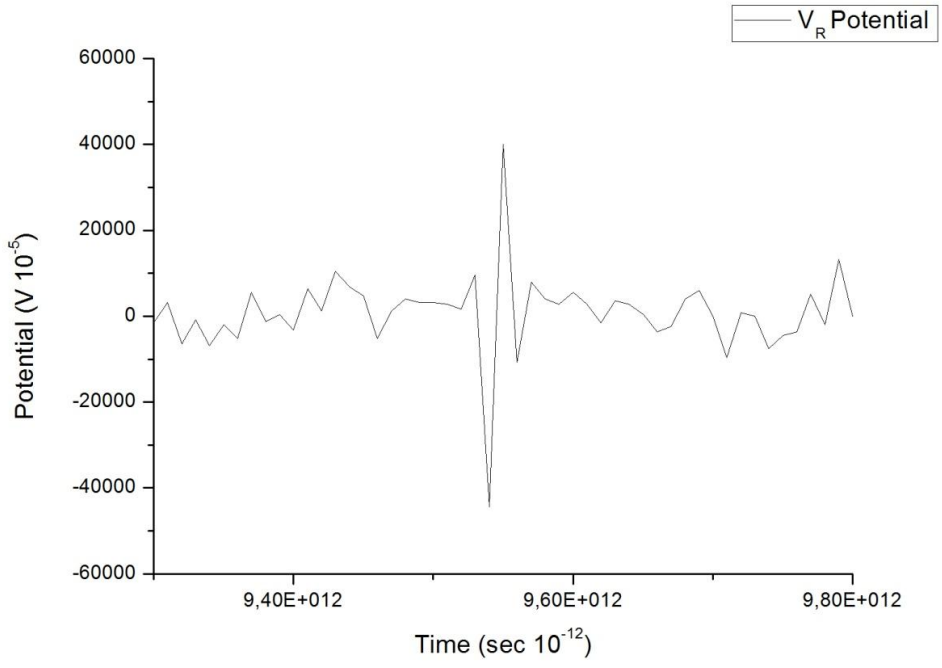

Figure 0.24 ***H6 device's detailed energy harvested peak.***

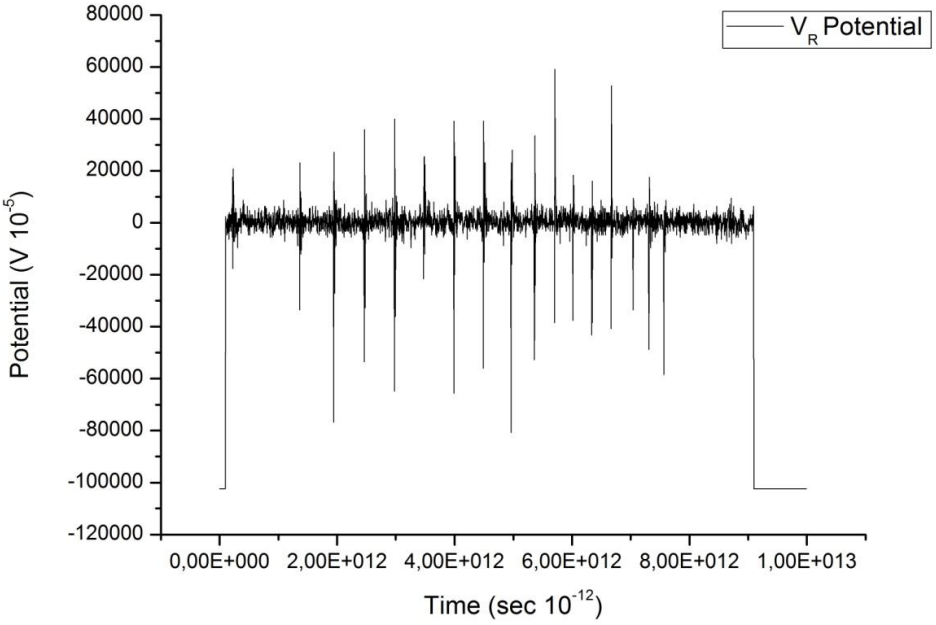

Figure 0.25 ***TF device's energy harvesting performance.***

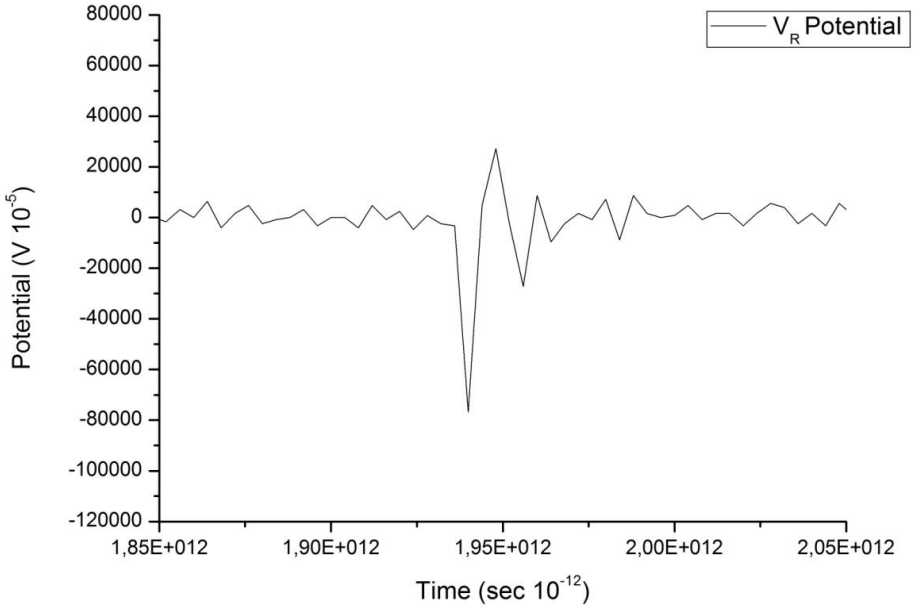

Figure 0.26 ***TF device's detailed energy harvested peak.***

From the previous figures the amount of harvested energy, through the dissipated power on the resistor is calculated. Table 3.4 resumes the energy harvesting performances of the fabricated nano-generators. In general, nano-structured energy harvesting devices are deposited on a planar substrate. Therefore the power scales with the active area (A) of the device. Hence, it is useful to calculate the *area power density* (P/A). In addition, for many piezoelectric energy harvesting devices based on ceramic piezoelectric materials the *volume power density* (P/V) is often quoted. This is obtained by dividing the power by the total volume of the device. Although different ways of calculating the volume (volume of active material or working volume required to accommodate the mechanical displacement) can lead to large discrepancies in reported power densities. In order to aid comparison between different nanostructured devices, the thickness of the device was taken as that of the active portion of the device, i.e. the piezoelectric plus any encapsulating material (PMMA) and electrodes, but not the supporting substrate. This is because the active layers could in principle be added to an existing surface, such as the casing of machinery, which does not alter the energy harvesting properties.

Table 3. 4 ***Energy harvesting performance of the three fabricated nano-generators, based on their peak to peak generated potential.***

Code name	***H3***	***H6***	***TF***
Power (μW)	3	18,4	250
Areal Power density (μW/cm^2)	25	102	625
Volumetric Power density (μW/cm^3)	71	238	3125
Energy (μJ)	0,015	0,368	5
Areal Energy density (μJ/cm^2)	0,125	2	12,5
Volumetric Energy density (μJ/cm^3)	0,35	4,7	62,5

According to the energy harvesting tests, ZnO thin film based devices are proven to be far more effective than the ones based on 1D ZnO nanostructures. This observation was mainly associated with the deformation of the material itself. The difference lies on the way a nanowire and a thin film are getting deformed during the operation. The bending/flexing of a thin film based piezoelectric beam was proven to strain the active ZnO layer in a more efficient way than it is done in the case of ZnO NW. Albeit ZnO NW used in the fabrication of H3 and H6 were expected to exhibit better performance as they are grown along their c-axis

(most piezoelectrically favored axis in ZnO, chapter 2), thin films are doing so (grown along all known axes for ZnO). During the experiments the instantaneous bending of the beam induces the material's deformation along diverse directions. This behavior makes the thin film based beam able to transform any kind of bending in polarization across the electrodes, in contrast to NW which are capable of exploiting mechanical energies imposed only along their c-axis direction.

The comparison between the shorter and longer NW used in H3 and H6 devices respectively, demonstrates clear superiority for the latter ones regarding their energy harvesting properties. It was proven that by almost doubling the NW size (mainly length) the energy harvesting properties are multiplied by a factor of sixteen. The previous observation was linked more to the deformation that the active materials get rather than any other material property, as they were grown in the same exactly way. These findings are in accordance to the results published by Rivera *et al.* where it was demonstrated that longer ZnO NW would lead to a larger charge generation than shorter ones [85].

Chapter 4

Graphene based materials in supercapacitor electrodes

Chapter four is describing the analysis done on candidate materials for supercapacitor electrodes. As mentioned in the introductory chapter, energy harvesting by itself cannot be essential if this energy is not properly stored for future use. A forthcoming technology in energy storage is given by supercapacitors, which can be placed in-between normal capacitors and batteries in terms of their storage properties. In this chapter, five different graphene based nano-materials are studied for their suitability in fabrication of supercapacitor electrodes. The most significant properties affecting their performance are studied and presented.

In the chapter's beginning it is found the characterization of mechanically exfoliated graphene for EDLC capacitors as well as its functionalization with MnO_2 nanoparticles in an attempt to probe pseudo-capacitance effects. Then the attention shifts to electrochemically exfoliated graphene nano-platelets and the chapter ends with the characterization of reduced graphene oxide materials. In the context of this chapter there are found XRD and Raman spectroscopy techniques, used to discriminate pure graphite (basis of graphene) from graphene, BET absorption techniques for specific surface estimation and SEM micro-characterization. Further, for determination of reduced graphene's oxide performance in elevated temperatures, thermogravimetric analysis (TGA) is implemented. In order to identify the types of oxygen groups present in graphene oxide materials, the corresponding Fourier Transform Infrared spectra (FTIR) were recorded and their contribution in rGO was examined by X-Ray photoelectron spectroscopy (XPS) analysis. In general this chapter reviews the most substantial analysis to be performed on any candidate material for determination of its effectiveness in supercapacitor electrode fabrication.

4.1 Electrode materials

As mentioned in the introduction any candidate material for supercapacitor electrode should fulfill the following requirements.

- High specific surface areas, typically from 1000 to 2500 m^2/g or more.
- High conductivity
- High surface wettability
- Thermodynamic stability
- Mechanical durability

As shown in Figure 1.6 supercapacitor electrodes are made from high surface area materials, upon or close to which the formation of electrochemical double layer takes place. Consequently a high surface area material is expected to form a considerably large double layer, thus offering high capacitance values. Porous carbon materials with their high surface areas are among the most promising candidates for this scope. Activated carbon structures are usually designed to combine mesopores (2 to 50 nm) and micropores (<2 nm). Both of them have a crucial role in energy storage and power delivery of the device [86]. Though a proportional increase in the capacitance with the surface area is expected, care must be taken in the electrolyte's accessibility at the electrode's surface. A large number of studies have shown that a significant percentage of obtained capacitance is due to presence of micropores [87]. Further studies state that the utilization of even smaller pores in energy storage (0.7-0.8 nm) called sub-micropores can lead to abnormal increase in the specific capacitance. On the other hand, the presence of mesopores guarantees affluent electrolyte accessibility towards micropores in a fast and efficient way by reducing the resistances that obstruct ionic movement. Therefore, high power densities are achieved. Basically, a suitable electrode design should include an optimized balance in the existence of these two pore types in order to perform adequately both of the previous functions.

Another factor of paramount importance when designing a supecapacitor is electrode's conductivity. Usually the parameters that influence a material's transport properties are its intrinsic electronic structure and its functionality. High electrode conductivity is desired in any electrochemical double layer capacitor (EDLC) charge storage application, as it facilitates the double layer formation. Any pore-like structure tends to decrease the conductivity of a given material. Therefore, any attempt of conductivity escalation by surface modification should be carefully examined as it may cost an available area loss. Although electrical conductivity is in general reduced in porous structures, ionic conductivity is improved by higher mobility of electrolyte ions through the pores. Electrical conductivity is also affected by surface functional groups like oxygen and nitrogen. These groups function like the mesopores (mentioned earlier) as they improve the electrolyte's accessibility to the active surface areas [33].

High surface wettability is needed for any given electrode, as it guarantees the successful electrolyte's penetration throughout the whole electrode's length. In this way the maximum possible number of carbon atoms assists in charge storage. Thermodynamic stability and mechanical resilience both assure a firm and stable electrode during supercapacitor's operation.

4.1.1 Activated Carbon

Activated carbon (AC) is the most popular electrode material in commercial supercapacitors due to its large surface area, low cost and easy process-ability. However the complex porous structure of AC does not permit the exposure to the electrolyte at all carbon atoms. Figure 4.1 shows a graphical comparison between different carbon structures in terms of electrolyte's ion accessibility. These, practically useless atoms with no contribution in charge storage, limit the specific capacitance of activated carbon electrodes.

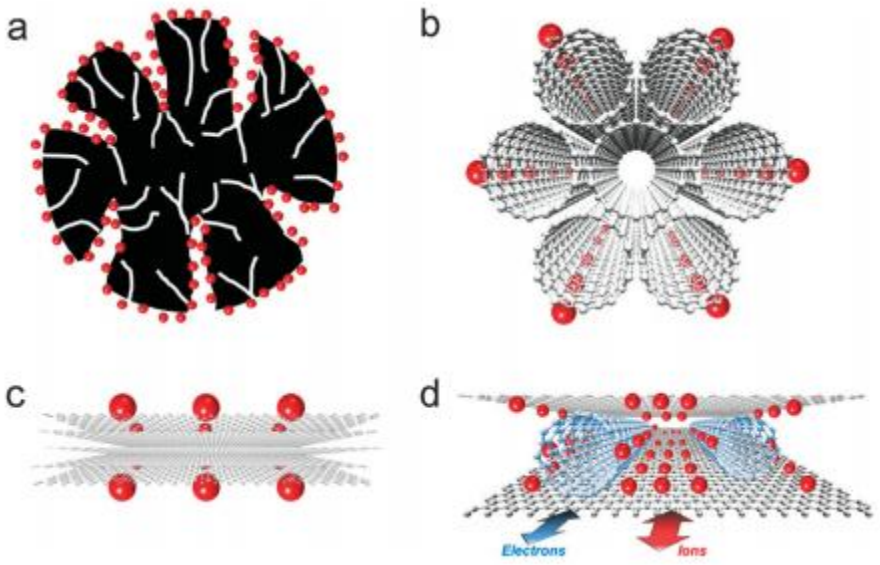

Figure 0.1 ***Comparison of different carbon based materials as supercapacitor electrodes. (a) Activated Carbon, (b) Carbon nanotubes, (c) Graphene, (d) Graphene + CNTs*** **[29].**

4.1.2 Carbon Nanotubes (CNT)

CNTs are usually viewed as graphene [88] sheets rolled up into a nanoscale tube form, to produce the so-called single-wall carbon nanotubes (SWCNT). When more than one graphene tubes is rolled around the core of a SWCNT then the form of multi-wall carbon nanotubes (MWCNT) is achieved. Figure 4.1(b) shows a representation of a SWCNT used as electrode material for supercapacitor applications. These nanostructured carbon materials possess many of the aforementioned requirements for EC electrodes. More specific CNTs exhibit high electrical conductivities [89] with decent surface areas [90] ranging from 300 to 1000 m^2/g. Their high mechanical and thermal stabilities [91] further support their use in supercapacitor electrodes. All previous characteristics tend to enhance energy and power densities. More recent studies revealed that the specific surface area of CNTs depends on their outer layer structures.

Due to their relatively easy fabrication methods, randomly entangled CNTs were the first materials of this type that were studied for supercapacitor electrodes. Compared with activated carbons, CNTs do not possess such large surface areas, but exhibit better electrical conductivity. Still, high specific capacitance values [92] of 102 F/g for MWNTs and 180 F/g for SWNTs [93] have been demonstrated. More recently, aligned CNTs have also been studied as electrode material in supercapacitors. It was proposed that their structure can be accessed easier by electrolyte's ions than, in entangled form. The alignment gives rise to a great amount of mesopores, a highly desirable property of supercapacitor electrodes. The principle results demonstrate that vertically aligned CNTs are reasonably advantageous over their randomly entangled counterparts for supercapacitor applications [94].

Their high intrinsic conductivity along with the accessible tubular network renders CNTs suitable for high power devices. Instead their low active surface area (~$450m^2/g$) is responsible for the relatively small

energy densities. Moreover CNTs tend to agglomerate after their fabrication, which is further decreasing their specific surface areas [95]. Figure 4.1(b) accurately represents the condition where the middle CNT is closely surrounded by a group of others and cannot participate in the charge storage mechanism as it is not accessible by electrolyte's ions. Further production techniques are necessary to overcome the agglomeration phenomena, along with the proper alignment to upgrade their efficiency in supercapacitor electrodes.

4.1.3 Graphene

Graphene [88], with its distinctive structure is one of the most favorable materials till date, to extend the storage limits in energy and power densities when used as electrode material in supercapacitors. The advantages of graphene are found also on CNTs, like high electrical conductivity, mechanical resilience and chemical stability. Graphene was reported to lead at high capacitance values. Typically the specific capacitance in a graphene based electrode may arrive at 350 F/g for aqueous electrolytes and 160 F/g for ionic liquids [96].

As seen earlier, supercapacitor electrodes are mainly constructed of porous materials (AC) or materials that can be arranged in a porous structure (CNT). Unlike them, graphene which is a monolayer 2-D material consisting of carbon atoms arranged in a honeycomb structure engages its high surface area in the charge storage mechanism. Ideally, graphene's layers should remain intact, while suspended inside the electrolyte solution permitting total surface area accessibility for EDLC formation [97]. More specifically the following reasons advance graphene as electrode in supercapacitors. Firstly, the high theoretical surface area of $2630 m^2/g$ [88] outreaches the one of CNTs and AC and provides more active sites for ions absorption. Then, as zero-gap semiconductor graphene's low resistivity of 10^{-6} Ω cm [98] supports the fast charge and discharge operations, which are highly appreciated in supercapacitors. Secondly the large tensile strength of 130 GPa [99] easily allows the use of graphene as single electrode material as well as in a shattered structure called graphene nano-platelets. Lastly, graphene can be easily functionalized with transition metals for pseudo-capacitance investigation since its chemical stability grants its use as a host substrate.

Figure 4.1(c) represents the ionic transport on graphene foils found in supercapacitor electrodes. In the ideal case all graphene foils should be in contact with the electrolyte. Hence, the total surface of graphene layers would be available for energy storage. However, the effort to produce single graphene sheets is obstructed by its tendency to stack with other layers and take the form of platelets (<100 layers). Figure 4.1(c) clearly demonstrates that internal layers do not participate in energy storage mechanism. As a result a lower gravimetric specific capacitance could be observed in this case, contrary to the theoretical predictions.

Synthesis of graphene has been reported to be done in several ways. Among the well appreciated, chemical vapour deposition (CVD) is used for the fabrication of graphene's nanoplatelets and nanoribbons. Alternatively chemical exfoliation using sulfuric acid is used to produce graphene oxide (GO). A key topic in the research and application of GO as supercapacitor electrode is the reduction, which partly restores the structure and properties of graphene. Different reduction processes result in different properties of reduced GO (rGO), which in turn affect the final performance of materials or devices composed of rGO. In this work, the

electrochemical performance of graphene based electrodes of appropriate mass loadings, suitable for supercapacitor applications are reported. Details for the fabrication of the materials and the electrodes are also discussed.

4.2 Properties and characterization of Graphene based materials

4.2.1 Commercially available Graphene nano-platelets (GNPs)

Commercially available GNPs purchased from XG Sciences (made by mechanical exfoliation) under the trade name *xGnP C-750,* were used as-obtained for electrode preparation and also as the scaffold for MnO_2 functionalization in case of MnO_2/GNP. GNPs were produced by mechanical exfoliation of graphite [100] and they consist of short stacks of graphene sheets in a platelet shape (Figure 4.2). More specific, xGNP-C-750 particles typically involve aggregates of sub-micron platelets with particle diameter smaller than 2 μm and thickness of few nm.

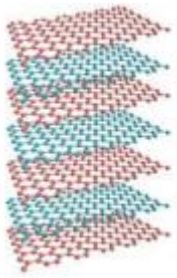

Figure 0.2 ***Representation of Graphene nano-platelet form. Several monolayers of Graphene in aggregation form the platelet.***

The morphology and structure of the employed materials were analyzed by means of scanning electron microscopy (SEM, QUANTAN FEG 650, FEI microscope), Raman spectroscopy (HR UV 800 (JYV-Jobin YVon), laser wavelength 532 nm) and X-ray diffraction (XRD) (diffractometer D5000 Siemens using Cu Kα radiation). Nitrogen adsorption/desorption isotherms were analyzed to determine the specific surface areas (ASAP 2010 Micromeritics nitrogen adsorption apparatus).

Figure 4.3 shows optical and SEM microscopy images of xGnP-C-750. It can be seen that xGnP-C-750 is made of very fine particles (~1 μm), which agglomerate to form larger particles of varied morphology (from irregular to spherical). These larger particles agglomerate in their own turn to form items of even bigger size. Due to the very fine grain size this anisotropic behavior is difficult to be seen.

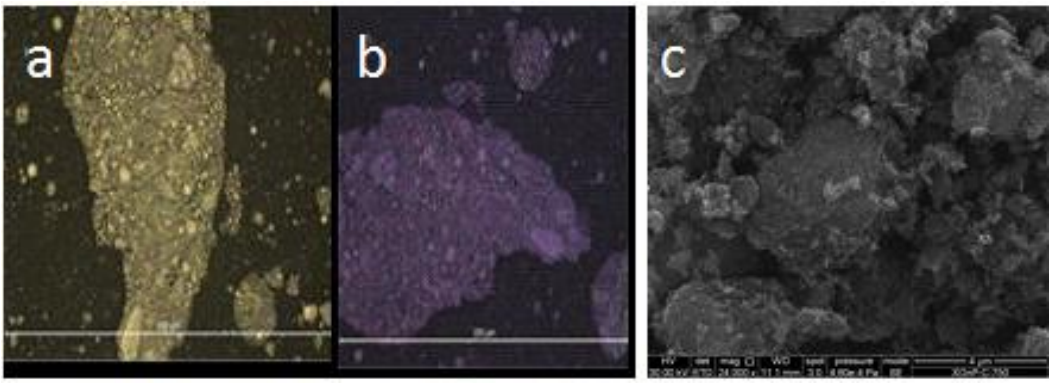

Figure 0.3 ***Optical microscopy images of xGnP-C-750 using a microscope with reflected and polarized white light (a) and (b), SEM image of xGnP-C-750 (c).***

Figure 4.4 presents the X-Ray diffraction measurement performed on xGnP-C-750 material. The results reveal an interlayer distance of 3.37 Å between two graphene foils. This distance is found to be quite in agreement with the theoretical one for graphite. Practically, the larger the number of graphene foils the more xGnP-C-750 moves towards nanostructured graphite, moving away from graphene's desired properties (surface area and conductivity).

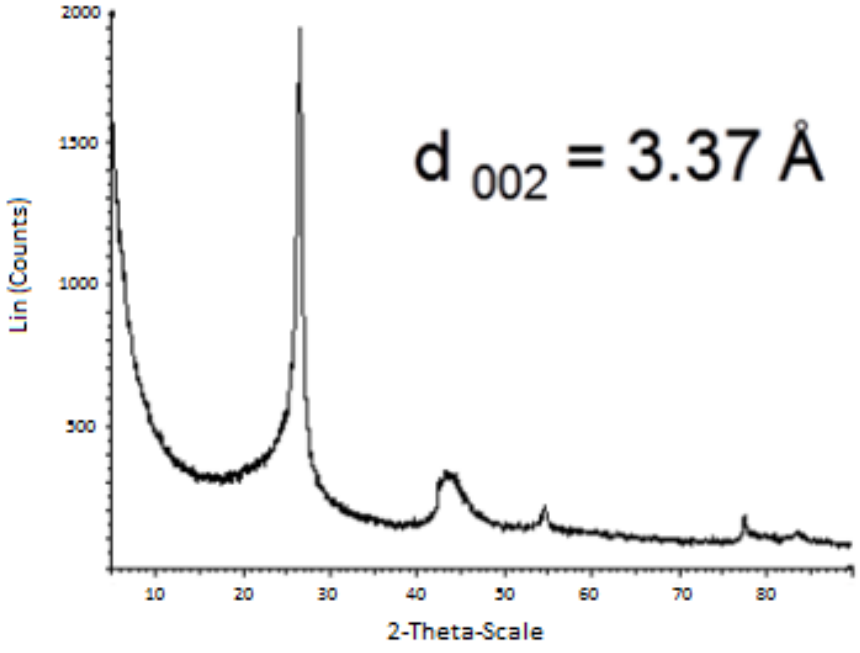

Figure 0.4 ***XRD spectra collected from xGnP-C-750 powder.***

The Raman spectra of xGnP-C-750 (Figure 4.5) presents three clear peaks. D, G and 2D peaks, at 1350 cm^{-1}, 1580 cm^{-1} and 2690 cm^{-1} respectively. Due to added forces from the interactions between the layers of stacked graphene, the spectrum will change from that of single-layer to that of multi-layer as the number of graphene layers increases. Typically, the stacking of numerous layers leads to the splitting of the 2D peak into an increasing number of modes that combine to give a wider, shorter or higher frequency peak, as in Figure 4.5. According to theoretical expectations, the first-order D peak should not be visible in pristine graphene because of its crystal symmetries [101]. In order for a D peak to occur, a charge carrier must be excited and inelastically scattered by a phonon, then a second elastic scattering by a defect or zone boundary must occur to result in recombination. The ratio of peak intensities I_D/I_G can be used to characterize the level of disorder in graphene. The noteworthy D peak reveals the existence of defects throughout the material, which can be attributed to the spacing between the different foils. In Table 4.1 a summary of xGnP's chemical composition is presented. As it was expected, carbon is the dominant element. However, the presence of others, like oxygen and nitrogen traces cannot be neglected.

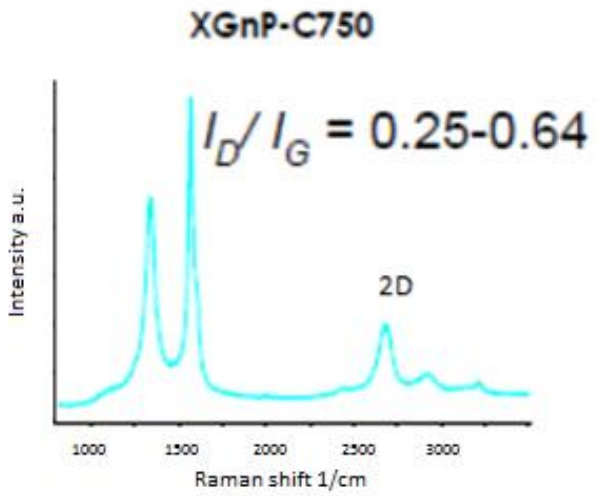

Figure 0.5 ***Raman spectra denotes the level of disorder of xGnP-C-750 material.***

Table 4. 1 ***Chemical composition analysis of xGnP-C-750 powder.***

Carbon	Moisture (%)	Volatile matter (%db)	Ash (%db)	C (%db)	H (%db)	N (%db)	S (%db)	O [diff.] (%db)
C-750	0.5	~ 5.0	0.5	96.2	0.1	1.3	0.02	1.9

In order to determine the specific surface area of the commercially available graphen nano-platelets, N_2 adsorption/desorption isotherms were obtained, as depicted in Figure 4.6. Owing to the presence of super-micropores (l_0 = 1.92 nm) in the material which can lead to unreliable results, the isotherms were analyzed with the Dubinin-Raduskevich model and Kaneko's comparison plot to obtain an average value instead of using the commonly applied BET model [102]. According to the experiment, a specific surface area of 479 $m^2\ g^{-1}$ was determined for xGnP-C-750 instead of 750 $m^2\ g^{-1}$ which was expected from the material's datasheet. The volumetric density of micropores (their critical role in charge storage was mentioned earlier) was possible by this measurement as well.

V_{pores} ($cm^3\ g^{-1}$)	0.49
Micropore volume ($cm^3\ g^{-1}$)	0.27
Average micropore size (nm)	1.92
Microporous surface ($m^2\ g^{-1}$)	– 283
External surface ($m^2\ g^{-1}$)	161
S_{BET} ($m^2\ g^{-1}$)	659
Total Surface Area ($m^2\ g^{-1}$)	479
O-surface functionalities	
($mmol\ g^{-1}$)	2.76
($\mu mol\ m^{-2}$)	5.76
Conductivity ($S\ cm^{-1}$)	0.19

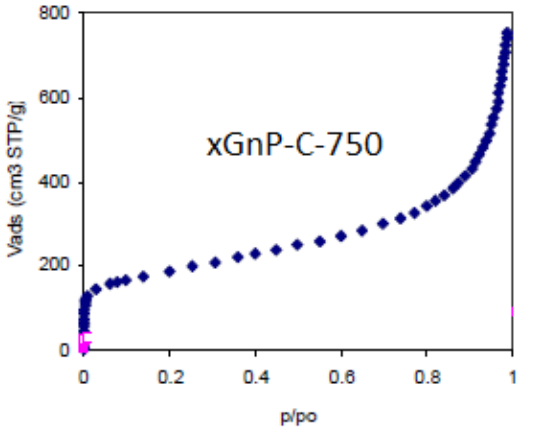

Figure 0.6 ***N_2 adsorption isotherm of xGnP-C-750 reveals the available surface area and the pore size distribution.***

4.2.2 Functionalized Graphene nano-platelets with MnO_2

The functionalization process was performed in accordance with the one described by Yu [103]. The commercial xGnP-C-750 was first dispersed in a 0.01 $molL^{-1}$ $KMnO_4$ followed by the drop wise addition of 0.05 $molL^{-1}$ citric acid until the solution turned brown/purple. The mixture was further heated up to 80˚C in a distillation column with full reflux for 7 h. The functionalised GNP was filtered out and dried at 80˚C for 12 h.

With respect to the commercial xGnP-C-750, a difference in the morphologies of GNP can be observed in Figures 4.7 (a) and (b), before and after the functionalization process respectively. By comparing the two micrographs, the additional presence of the white particles in Figure 4.7(b) confirms the successful decoration of GNP with MnO_2 nano-particles, whose size range from a few nanometers to some microns. The nature of these nano-particles was then investigated with the following methods. Energy dispersive analysis was performed to qualitatively identify the presence of Mn (Manganese) and Oxygen (O), Figure 4.8(a). Structural analysis of the prepared material, further confirmed the presence of graphene and MnO_2. Specifically in the

XRD pattern in Figure 4.8(b) it is visible a sharp peak at 26.2º which corresponds to graphitic-like structure of GNPs and weaker broad diffraction peaks at 36.5 and 66.4º, respectively, indicating the formation of MnO_2.

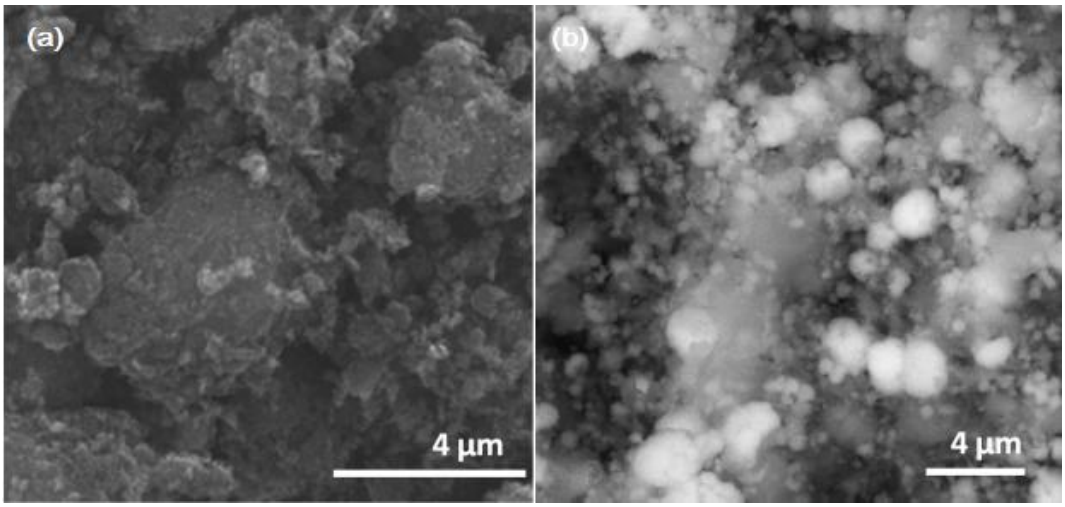

Figure 0.7 ***GNP (xGnP-C-750) SEM micrographs before (a) and after functionalization with MnO_2 nanoparticles (b).***

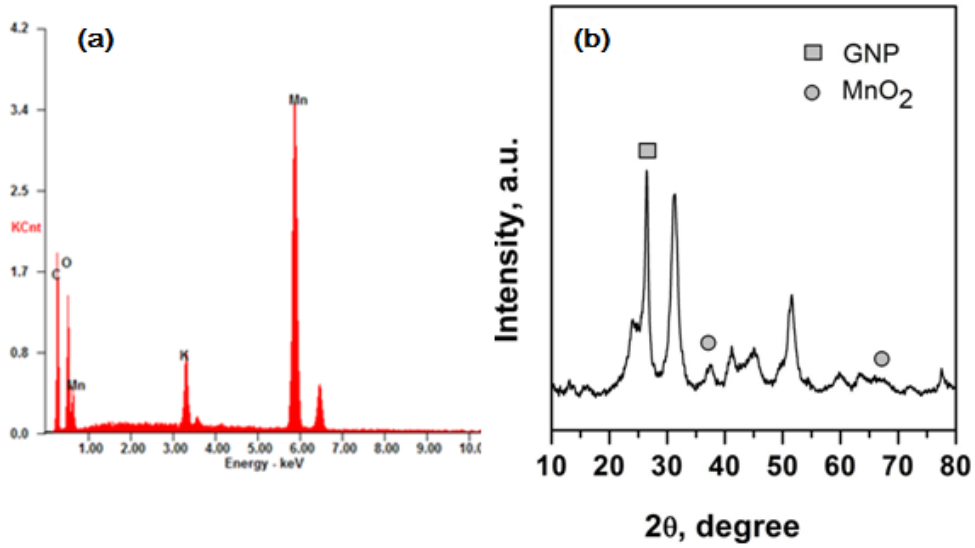

Figure 0.8 ***Energy dispersive EDS qualitative analysis (a) and XRD spectra (b) of the MnO_2 functionalized GNP certify the presence of MnO_2 particles.***

Additional, surface characterization was performed to determine the available specific surface area (A_{sp}) of the functionalized material. The same method of N_2 isotherms, analyzed with the Dubinin-Raduskevich model was used for this case as well. The result showed a severe decrease in the specific surface area of the GNP-MnO_2 with respect to the commercial GNP of about 92%. As revealed from Figure 4.9 the GNP's specific

surface dropped from 479 m^2/g to 39 m^2/g, for the functionalized GNP. The reduction in A_{sp} is addressed to the presence of MnO_2 particles, as well as the functionalization process.

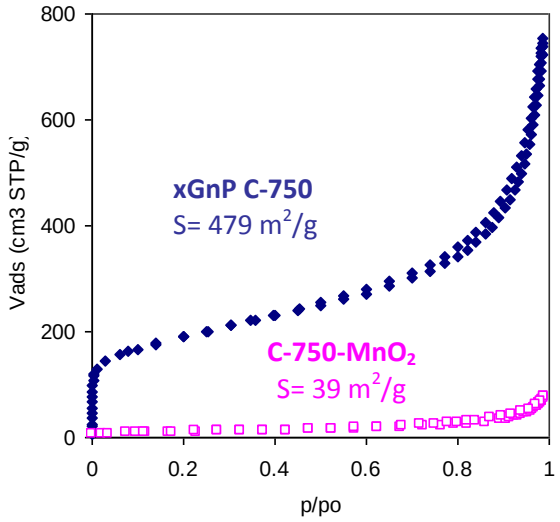

Figure 0.9 ***Specific surface areas of GNP (xGnP-C-750) and GNP-MnO_2, through N_2 adsorption measurements. The dark blue points refer to the normal GNP, while the magenta points refer to the functionalized GNP.***

4.2.3 Electrochemically exfoliated Graphene nano-platelets (eGNP) from graphite

The electrochemical exfoliation process was carried out in a setup as described by the schematic in Figure 4.10 on the anode [104] of the electrochemical cell. The setup consisted of five graphite electrodes (from Mueller & Roessner, tradename *MREG-E*) partially submerged in a sodium hydroxide electrolyte (NaOH) (of 0.1 M). The electrodes were placed 15 mm apart and the portions of each electrode that were not in contact with the electrolyte were connected to a power supply. Two of the five electrodes, were connected to the positive end of the power supply, thus acting as the anode; while the remaining three were connected to the negative end, hence acting as the cathode. A potential difference of 7 V was thereafter applied across the cathodes for the exfoliation to occur.

After the exfoliation process, the materials detached from the graphite electrodes along with the electrolyte were filtered through a pressure aided filtration setup, Sartorius 16249, with the assistance of a Millipore® polycarbonate filter membrane of 0.4 µm cut size. The filtration process was repeated with the addition of de-ionized water until a neutral pH in the filtrate was obtained. The graphene based nano-platelets were thereafter collected as residue from the filtration process and analyzed.

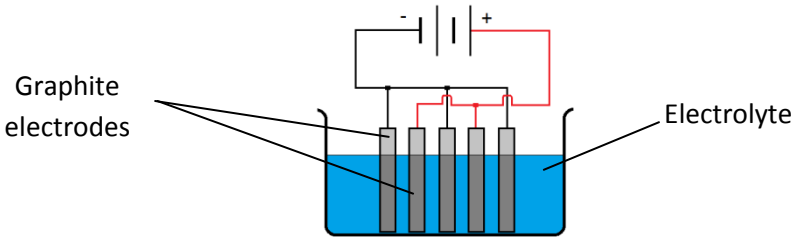

Figure 0.10 ***Electrochemical cell setup used in anodic exfoliation of GNP (xGnP-C-750).***

SEM imaging and Raman spectroscopy have been employed for morphological and structural characterization of the electrochemically exfoliated GNPs (eGNP). As done for the previous samples, nitrogen adsorption measurements for the determination of eGNP's specific surface area were performed for this case as well.

The first set of characterization presented in Figure 4.11, is the SEM micrographs taken of eGNPs after the filtration process. Therein, the layered structure of eGNP is shown. Micrometer and sub-micrometer inter-stack spacing between the graphitic sheets is clearly demonstrated at higher resolutions in Figure 4.11(b). For referencing purposes, the SEM micrograph of raw MREG-E graphite before the electrochemical exfoliation process is shown in Figure 4.12.

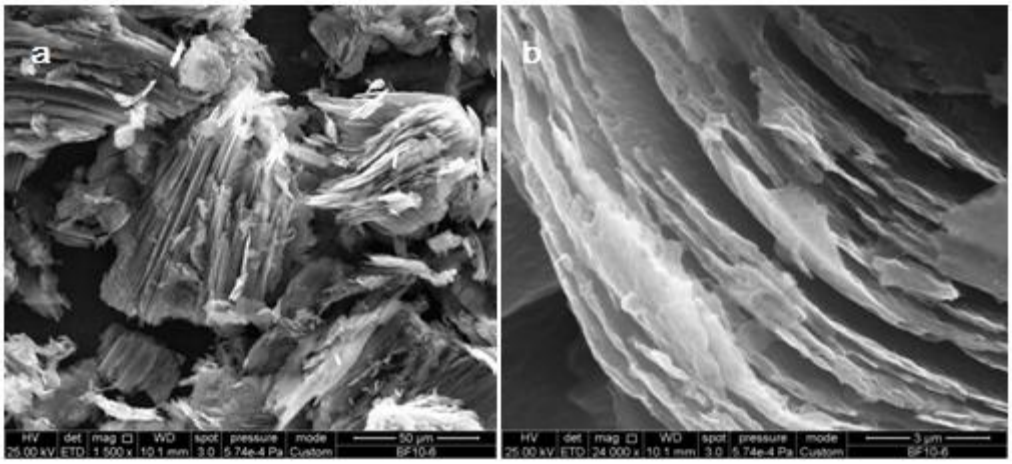

Figure 0.11 ***SEM micrographs of eGNP at different scales, a) the exfoliated GNP from graphite and b) layered structure shown by increased magnification.***

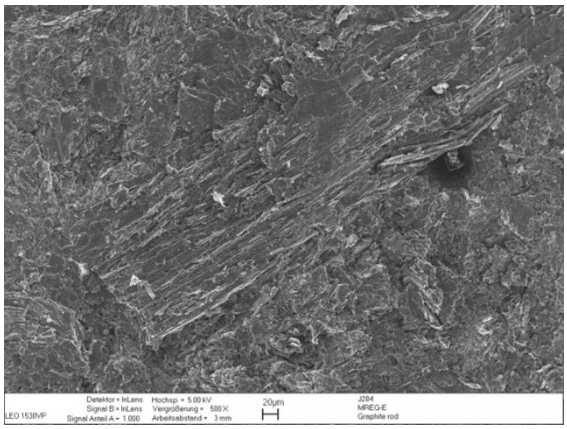

Figure 0.12 ***SEM micrograph of MREG-E graphite before the electrochemical exfoliation.***

Raman shift of eGNP was compared to the raw MREG-E graphite's. In Figure 4.13, the spectrum in blue (of MREG-E) shows a typical G and 2D-band, at ca. 1580 cm^{-1} and 2700 cm^{-1} respectively, along with a small D-band at ca. 1350 cm^{-1}[105]. However, the green spectrum (of eGNP) exhibited an intense and broad D-band which is merged with the G-band. As D-band is assigned to the local defects and disorder especially at the edge of GNPs, this illustrates that the exfoliation was carried out successfully. Due to the above, a significant change in the 2D-band was also observed, giving it a modulated shape [106].

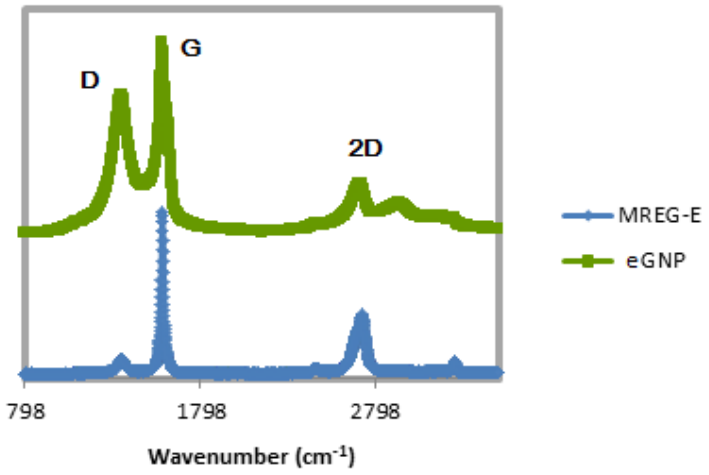

Figure 0.13 ***Raman shifts of graphitic materials before and after the electrochemical exfoliation process. The spectrum in blue color comes from the raw graphite while the spectrum in green from eGNP.***

The closing set of analysis for eGNP, compares its N_2 adsorption isotherms with the ones coming from raw graphite. From Figure 4.14, it is evident a 2.6 times increase in specific surface area compared with raw

graphite after the electrochemical exfoliation process. From these figures, the isotherm in black, Figure 4.14(a) shows that the raw graphite possesses a specific surface area of 4.5 m^2/g, while the isotherm in red, Figure 4.14(b) establishes that eGNP possesses a specific surface area of 12 m^2/g.

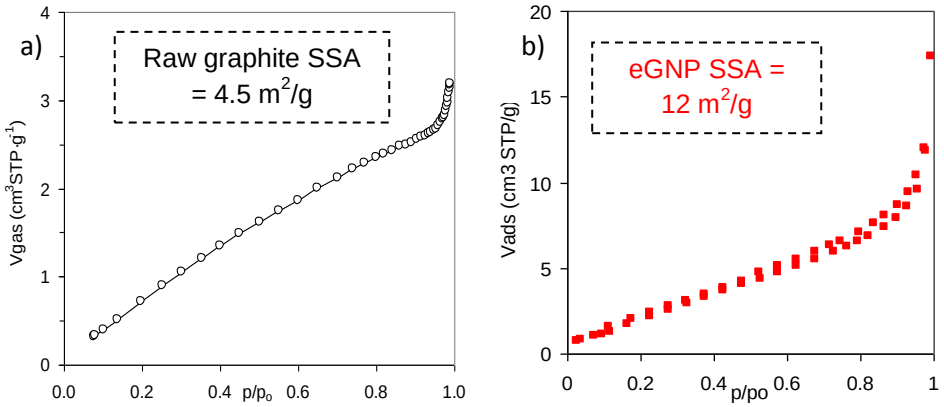

Figure 0.14 Specific surface area determined through N_2 adsorption measurements; (a) measurement results of the raw graphite and (b) of eGNP.

4.2.4 Chemically reduced graphene oxide (rGO)

For the synthesis of GO, 1 g graphite powder was oxidized with H_2SO_4 98% and $KMnO_4$ at 35 °C for 3 h[107]. Further, the mixture was diluted with deionized water and reaction was terminated by adding H_2O_2. The obtained graphene oxide (GO) was filtered, purified with HCl and washed with deionized water till neutral pH was reached and dried at 50 °C for 24 h. For the chemical conversion of GO into rGO, an aqueous dispersion of GO (0.5 mg mL^{-1}) was subjected to sonication treatment for 1 h. Ascorbic acid was added (10:1 w/w ascorbic acid:GO) to reduce GO for 6 h at room temperature, under mechanical stirring. The obtained rGO was isolated by filtration, washing with water and vacuum drying at 50 °C for 24 h.

A series of measurements have been performed, revealing the structural and morphological properties of the as-prepared rGO material. The structural investigation was done by X-Ray diffraction (XRD, D2 Phaser - Bruker) on a diffractometer using Cu Kα radiation and a voltage of 30 kV. Figure 4.15 shows the typical XRD spectra of the GO material before and after the reduction with ascorbic acid. Upon oxidation, the (002) diffraction peak of graphite was shifted from 26.5º to 9.84º while the subsequent reduction of GO with ascorbic acid resulted in the shift of the diffraction peak back to higher 2θ, respectively at 13.78º, indicating the partial restoration of conjugated sp^2 carbon network.

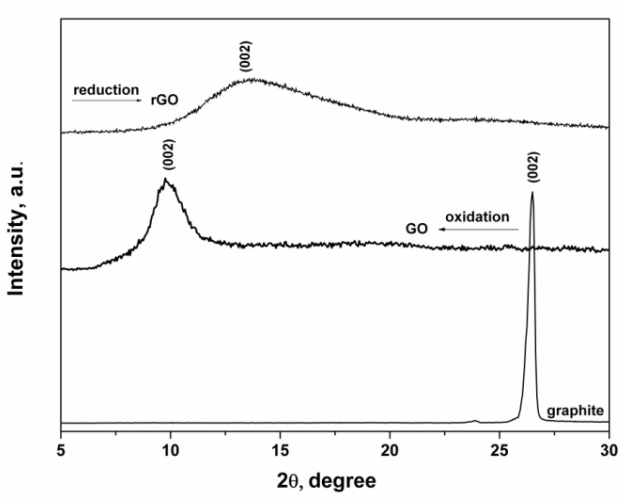

Figure 0.15 ***XRD spectra of GO (lower line) and rGO (upper line) shows a relevant shift and widening of (002) peak.***

The XRD spectra depicts a sharper GO peak in comparison with rGO one, which has lower intensity and a higher full width half maximum point. These results are translated into an increase of the interlayer spacing due to introduction of oxygen functional groups in GO. From 0.34 nm interlayer distance in graphite, the expanded material reaches a value of 0.92 nm and further suffers from re-stacking upon the partial removal of oxygen groups by reduction with ascorbic acid, reaching a 0.57 nm interlayer distance in rGO.

In order the presence of oxygen functional groups to be probed and their thermal behaviour to be evaluated, Thermogravimetric analysis (TGA, Q50 - TA Instruments) is conducted at a scanning rate of 10 ºC min^{-1} under nitrogen flow and the results are shown in Figure 4.16. With respect to graphite that shows high thermal stability of only 5% weight loss below 700ºC, both GO and rGO materials exhibit various weight loss steps, as depending on their composition. The GO plot and corresponding weight derivative show an initial loss of 12% at 100ºC attributed to adsorbed water molecules which is followed by the decomposition of labile oxygen groups registering a steep loss of 26% in the range 100-200ºC and a steadier one of 15% in the range 200-300ºC. Conversely, the rGO shows a smoother and lower weight loss in this temperature range, of a total of 18%, as indicated by the derivative plot showing a smaller peak in the range 100-200º and a shoulder in the range 200-300ºC. As the derivative plot show, the removal of more stable functional groups starts at about 450ºC in GO material, while in rGO the onset is delayed to about 550ºC. The final retained weight at 750ºC was of 17% for GO while 34% for the reduced material. The intensity ratio of derivative peaks for the temperature range of 100-300 ºC results indicate the efficiency of ascorbic acid in removing the functional groups is higher for the oxygen groups that decompose in the temperature range of 100-200º than the ones attributed to the 200-300 ºC. In regards to the removal of more stable oxygen groups, the derivative peak has higher intensity and appears at higher temperature for rGO than for GO indicating that the assessment of the efficiency needs to take into account not only the types of oxygen groups but other factors, as well, such as re-stacking of the sheets observed by XRD measurements.

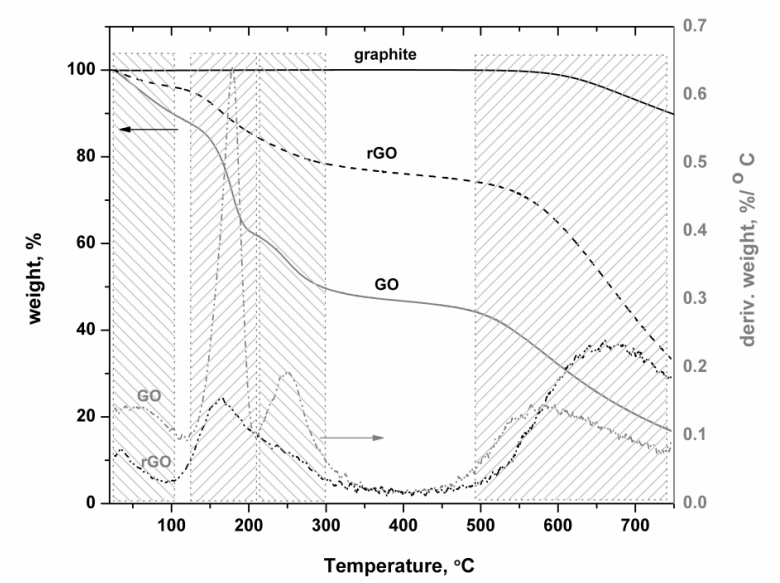

Figure 0.16 ***Thermogravimetric and derivative plots of GO and rGO demonstrate Graphene's weight retention over the temperature.***

In order to identify the types of oxygen groups present in the graphene materials, the corresponding Fourier Transform Infrared spectra (FTIR, FTIR Spectrum BX - Perkin Elmer) were recorded, as depicted in Figure 4.17. The spectra of GO confirmed the successful oxidation of graphite by the appearance of the following features: a broad band at 3000-3600 cm^{-1} attributed to the adsorbed bound water and O-H stretching vibrations [108] and narrower bands at 1783 (C=O stretching vibration band from carbonyl and carboxyl groups), 1614 (C=C stretching vibrations from un-oxidized graphitic domains or to ester groups)[109], 1336 (O-H bending vibrations from hydroxyl groups), 1223 (breathing vibrations from epoxy groups), 1076 (C–O stretching vibration) and at 972 cm^{-1} (stretching vibration bands from epoxy, ether or peroxide groups) [110][111]. The decreased intensities corresponding to oxygen groups observed upon reduction confirmed their partial removal and while their different evolution indicated the efficiency of ascorbic acid in removing the oxygen groups is highly dependent on the type of oxygen groups.

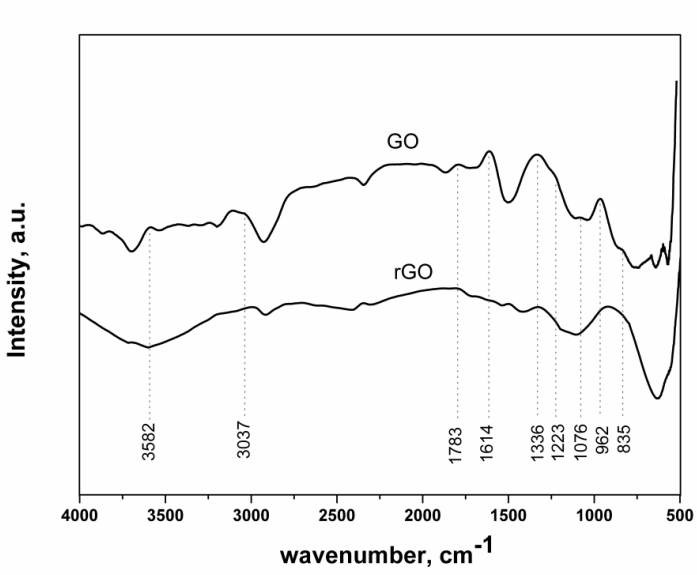

Figure 0.17 ***Fourier Transform Infrared spectra of GO and rGO present the oxygen groups found in the Graphene oxide materials.***

The contribution of oxygen groups in rGO was examined by X-Ray photoelectron spectroscopy (XPS) analysis by means of Omicron spectrometer system equipped with a hemispherical electron analyzer operating in constant pass energy, using Mg Kα radiation (1253.6 eV). Survey scan spectra is performed at pass energy of 50 eV, while the C 1s individual high resolution spectra is taken at pass energy of 20 eV. All binding energies are referenced to the C 1s line at 284.6 eV. The XPS spectra surveys, and the high resolution C 1s and O 1s XPS bands of the rGO and GO materials were recorded and their deconvolution was performed. The peak areas calculation of C and O elements from XPS spectra survey scan in Figure 4.18(a) revealed that the C/O atomic ratio increased from 2.8 in GO to 5.7 in rGO thus indicating an increase in C-content upon reduction, and an associated decrease of the oxygen groups, which was consistent with results of XRD and TGA.

The C 1s band was fitted to six components: (1) located at the binding energy of at 284.4 eV (C=C species), (2) and (3) located at 285.12 eV and 286.02 eV (while some works assigned them to C–OH and epoxy C–O groups [112], other researches assigned them to defective graphitic structure and C sp^3, respectively [113]), (4) at 287.5 eV (>C=O), (5) at 288.2 (COOH) and (6) at 289.04 eV (shake-up satellite band of graphitic carbon band). In accordance with previous reports considering that epoxy groups should have a larger binding energy compared to hydroxyl ones, while the double bond C=O occurs at even higher values, arising from >C=O followed by COOH, here the peaks at 285.12 and 286.02 eV were assigned to hydroxyl/phenolic group, and to epoxy group, respectively [114].

As an estimation of the degree of oxidation, it was observed that the sp^2 carbon fraction obtained by dividing the area under the sp^2 peak and that of C1s peak decreased from 86% in GO to 72% in rGO. Further, the C1s band in Figure 4.18(b) showed that the largest proportion of oxygen in GO was present in the form of C–O functionalities and the lowest were associated with C–OH groups, in agreement with earlier findings regarding Hummers oxidation process [115]. However, the spectra for rGO showed a different evolution in the relative contribution of the components associated with oxygenated species upon reduction, that is while >C=O and

COOH decreased, C–O suffers a slight increase and C–OH got almost doubled, thus indicating that the deoxygenation of some groups produces on the expenses of others. These results come in agreement with the TGA and previous studies confirming that deoxygenation process does not only depend on the proportion of oxygen groups but also on their type and distribution and number of graphene layers [116]. On the other hand, the evolution of the component contribution in the C 1s band after reduction shows a decrease in sp^2 content, while sp^2 species are the dominant component.

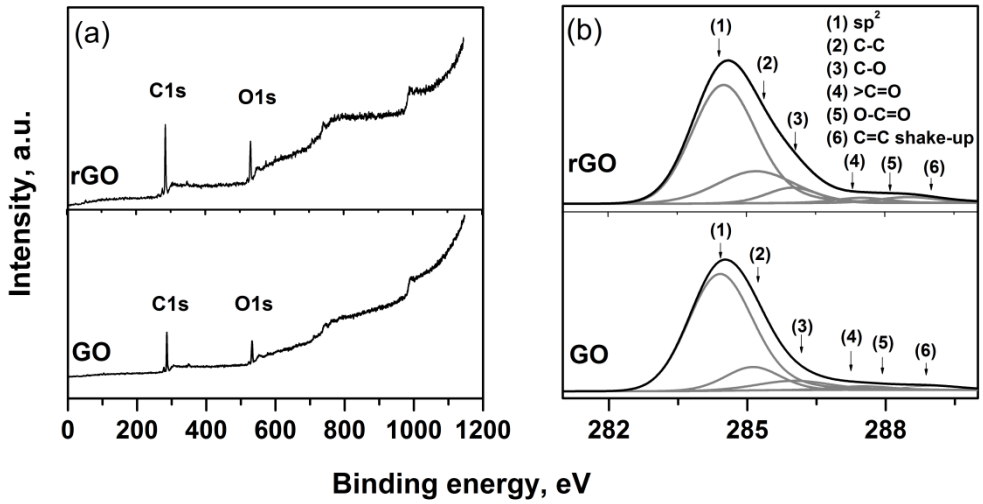

Figure 0.18 X-Ray photoelectron spectroscopy *survey (a) and high resolution C1s XPS spectra de-convoluted peaks for GO and rGO (b).*

The structural changes produced in GO by reduction with ascorbic acid were studied by Raman spectroscopy as presented in Figure 4.19. Both spectra showed the typical D band originating from the edges and attributed to defects at 1352.2 cm^{-1} and the G band corresponding to the first-order scattering of the E_{2g} mode of sp^2 domain of graphite at 1590 cm^{-1}. Considering the relative intensity of D band compared to G one as strongly dependent on the amount of disorder, it can be observed that I_D/I_G is smaller for rGO than GO, since the disorder associated with the oxygen-defects diminishes upon their partial removal. Nevertheless, there is a considerable level of disorder, as indicated by the appearance of the 2D band at 2695.8 cm^{-1} originating from a two phonon double resonance Raman process, indicative of crystalline graphitic material which is slightly less intense in rGO. The previous confirms steric effects of oxygen groups on the stacked layers, assessed as well by the presence of the D+G combination mode induced by disorder at 2936 cm^{-1}, respectively [117].

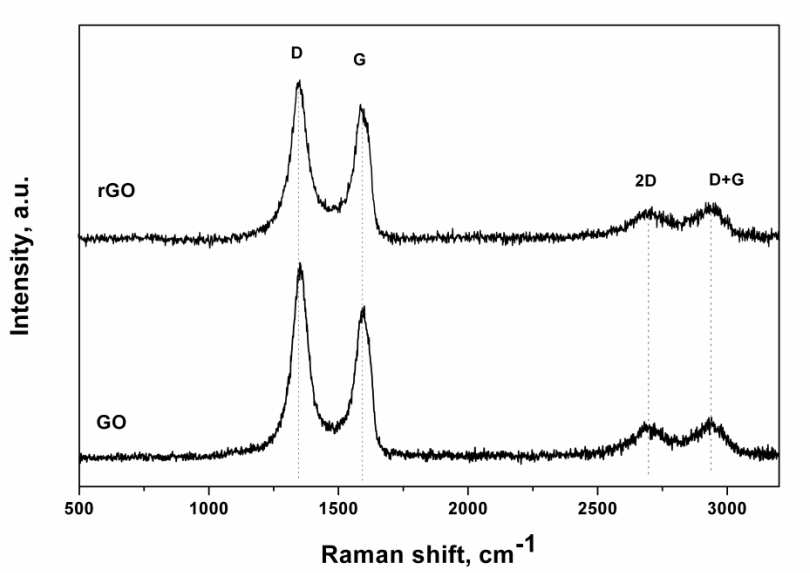

Figure 0.19 ***Raman spectra of GO and rGO.***

Finally, morphological characterization by SEM imaging is presented in Figures 4.20 (a)-(d). A highly porous morphology is observed for both electrodes (rGO and rGO with carbon black) together with the wrinkled structure characteristic to rGO materials. The rGO sheets are well distributed in the coatings as confirmed also by the fracture investigation in Figure 4.20(e). While the morphology of rGO alone shows crumpled sheets, a better distribution of rGO sheets and less agglomeration are observed in the case of rGO decorated with carbon black particles. This result comes into good agreement with previous findings on the incorporation of carbon black into graphene that resulted in the inhibition of the agglomeration of graphene sheets, offering improved electrolyte–electrode accessibility and electrode conductivity [118].

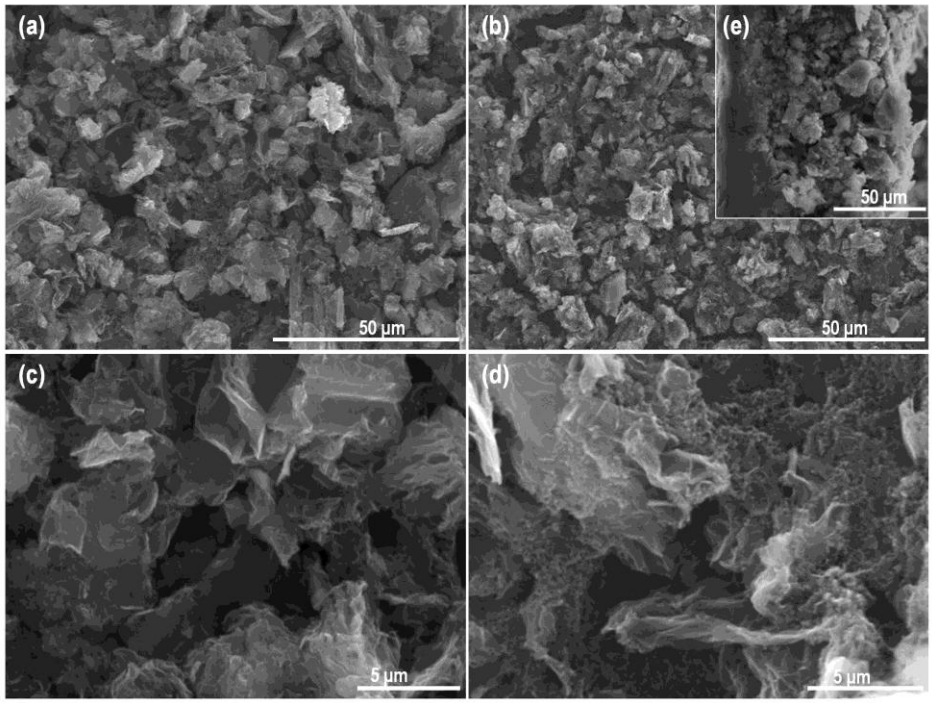

Figure 0.20 ***SEM images at different magnifications for rGO (a) and(c), rGO with carbon black (b) and (d). Inset (e) represents a cross-section of the electrode shown in (b).***

Chapter 5

Electrochemical characterization of supercapacitor devices

The transition from the raw material (AC, Graphene, CNTs) to a supercapacitor electrode and then to the final device requires the performance testing and characterization by well-established electrochemical methods. In this chapter the shift from the graphene material itself to supercapacitor electrode is reported and followed by a precise electrochemical characterization approach. All electrodes tested in this thesis, by the aforementioned graphene nano-materials have been constructed following industrially available techniques (centrifuging, bar coating) based on standard procedures applied for activated carbons (in Fraunhofer IPA). They, have been mounted in an appropriate electrochemical cell to form a lab-scale supercapacitor, in a similar way to a commercial device (supercapacitor consists of two electrodes facing each other and a porous separator in between, Whatman). The whole structure is impregnated in an electrolyte which provides the relevant ions for charge storage mechanism. All processes regarding the prototype device mounting and testing procedures are explained in details, so as to make the results repeatable and reliable. Since there has not yet formed a testing protocol for supercapacitor devices the constant current technique used here, was introduced as being the accepted method from the battery industry for performance evaluation of energy storage devices.

5.1 Measurements cell

The dominant method for performance evaluation, when designing an active electrode material for supercapacitor applications is by direct electrochemical capacitance measurements. To this end, a supercapacitor's electrode can be tested either alone, in a three point electrochemical cell or coupled by another electrode in a two point full cell. These two measuring techniques differ by several important aspects [119]. Three electrodes cells are commonly found in electrochemical research and they consist of a working, a counter and a reference electrode. The crucial point is that only the working electrode contains the material being analyzed. The reference electrode is introduced for a precise potential control and the counter electrode serves for completing the electrical circuit for the analysis. On the other hand, two electrode cells consist of two similar or not electrodes facing each other in an anode and cathode principle, like a real capacitor.

One of their basic differences lies on the voltage applied to the electrode under characterization. For the three electrodes cell the whole potential window is implemented to the working electrode, so the x-axis of the cyclic voltammetry (CV) chart represents the voltage applied over that specific electrode. Conversely, for the two electrodes cell, the voltage window is applied to both electrodes in a differential way. In this manner

the potentials of each electrode are equal with each other and the half value of that presented in the CV chart. Consequently for a given potential on the x-axis of the CV, the electrode under characterization of a three electrode cell has twice the potential applied as is applied to the electrodes of a two electrode cell [119]. This can easily result in inconsistent values reported by these different approaches.

Another factor of major importance is the distance between the electrodes. When the three electrodes technique is followed, the electrodes are immersed inside the electrolyte and the typical distance between them is a few mm. Instead, when a two electrodes cell is employed the distance between the electrodes can be even in the μm range, depending on membrane separator's thickness. A higher distance between the electrodes can vary the time the ions need to conduct the charge, inserting higher resistances. In Figures 5.1 and 5.2 are represented the two previous measuring techniques, 2-electrode and 3-electrode cells respectively.

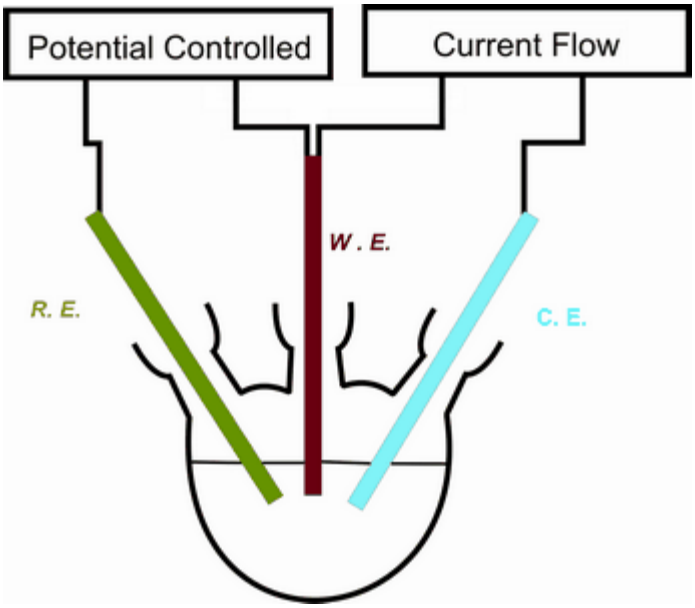

Figure 0.1 ***Schematic representation of a three electrodes electrochemical cell*** **[120].**

From Figure 5.1 it is clear that the distances of the electrodes can be adjusted and arrive at the smallest conceivable without contacting each other. Such an approach would decrease the possible the resistances introduced by the high spacing of the electrodes but still, could never reach the ones allowed by the 2-electrodes' porous separator. Moreover a 3-electrode cell is more sensitive in analyzing faradaic reactions and voltages on a single surface [119]. Thus, it can lead to large errors when projecting the energy storage capabilities of an electrode for supercapacitor use.

Taking in account the previously mentioned reasons, a two electrode cell was designed for conducting electrochemical measurements. Figure 5.2 is schematic representation of the actual cell used for performance measurements.

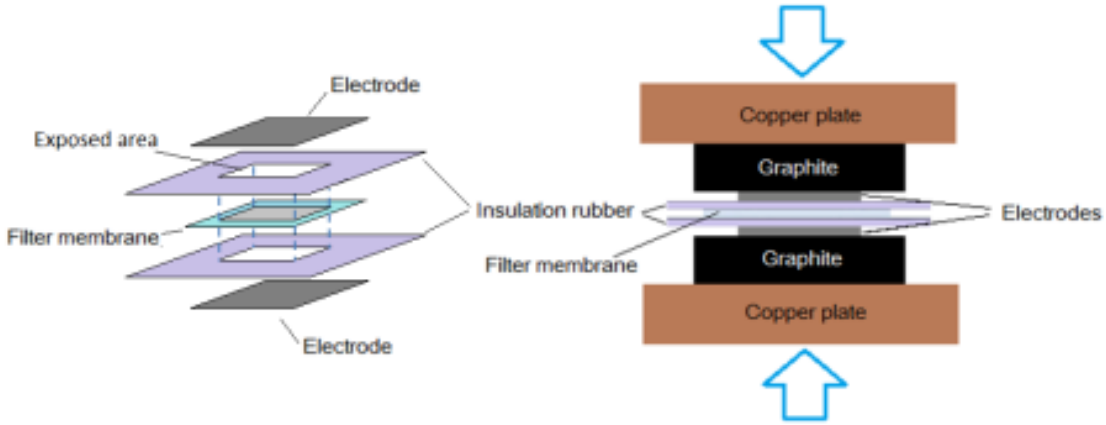

Figure 0.2 ***Schematic representation of the two electrode cell designed in CRF's labs for electrochemical performance measurements.***

As seen from the former figure the cell was designed to permit a window of 2x2 cm^2. At this exact point the two electrodes fabricate the supercapacitor testing device. More precisely, graphite plates were inserted to the back part of the each electrode (current collectors), providing the appropriate potentials. The choice of graphite was done due to its chemical stability, across a large number of electrolytes. In-between the two electrodes a commercially available filter membrane (Whatman Glass microfiber filters 934-AH), pre-soaked with the electrolyte was inserted. For decreasing the interactions with environmental air during the operation and maintain the electrolyte inside the exposed area, two rubber insulators were employed. Their functionality, which resembles a gasket–like condition, is important in keeping the electrolyte in liquid form throughout the whole measurement, as any contact with the environmental air could provoke its evaporation or crystallization. Figure 5.3 shows the genuine fabricated cell which exactly mimicking a supercapacitor's layout.

Figure 0.3 ***Supercapacitor test cell based on two electrodes cell configuration (actual device).***

5.2 Electrochemical measurements

A significant factor for the performance of a supercapacitor device is the electrolyte. As mentioned earlier, the electrolyte provides the ions, the movement of which is responsible for the creation of the electrochemical double layer. Electrolytes consist of a solvent and dissolved chemicals that dissociate into cations and anions, making the electrolyte electrically conductive [20]. The more ions the electrolyte contains, the better its conductivity. In supercapacitors the electrolytes are the electrically conductive connection between the two electrodes. The three main types of electrolytes differentiate upon the solvent used for their fabrication. As a result, aqueous, organic and ionic liquid electrolytes have been studied in supercapacitors development. General requirements for electrolytes include their chemical inactivity and low viscosity. The first one for avoiding any chemical attack to the other materials and ensuring long time stable behavior of the capacitor's electrical parameters. Additionally the second, leads to better electrolyte infiltration to the porous structure of the electrodes and promotes the ions adsorption to a larger surface, which means larger double layer formation and finally higher capacitance values.

Water is a relatively good solvent for inorganic chemicals as it offers fairly high conductivity values. Aqueous electrolytes have an electrochemical window of 1.15 V and a relatively low operating temperature range. For these reasons, they are used in supercapacitor devices with low energy and high power densities. The most common aqueous based electrolytes are KOH and H_2SO_4. On the other hand, organic solvents exhibit lower conductivities than the aqueous ones, so lower power densities are expected. However due to their higher dissociation voltage of 2.7 V they offer higher energy densities, as the energy scales with the square of the operating potential. Lately, ionic liquid electrolytes are proposed due to their increased electrochemical windows (> 2.7 V) and their chemical stability. The investigation of materials offering high energy densities in supercapacitor applications, led to the choice of an organic based electrolyte for the following electrochemical characterization. Tetraethylammonium tetrafluoroborate ($TEABF_4$) in acetonitrile (AC) was used as electrolyte throughout all measurements performed.

5.2.1 Capacitance performance by Cyclic Voltammetry (CV)

Cyclic voltammetry is a valuable and relatively rapid technique in determining the capacitance properties of an electrochemical cell. The capacitance measurement is achieved by cycling in a linear way the potential applied to the cell between two selected values, determined by electrolyte's composition. In this way the potential applied to the cell varies linearly with time, while returning a time-dependent dynamic responsive current which is recorded by computer software. Any linear voltage applied on an EC edge is theoretically predicted to give rise to a current flow of a constant value, according with the equation Eq 5.1.

$$i = C\frac{dV}{dt} \qquad [5.1]$$

So the ideal double layer capacitance in a CV graph should be depicted by constant currents during the charge and discharge phases. These current values should be of the same order of magnitude but with different signs (±i). Subsequently a rectangular form of the CV graph (voltage is plotted on x-axis and current on y-axis) is expected for a double layer supercapacitor, as depicted in Figure 5.4(a).

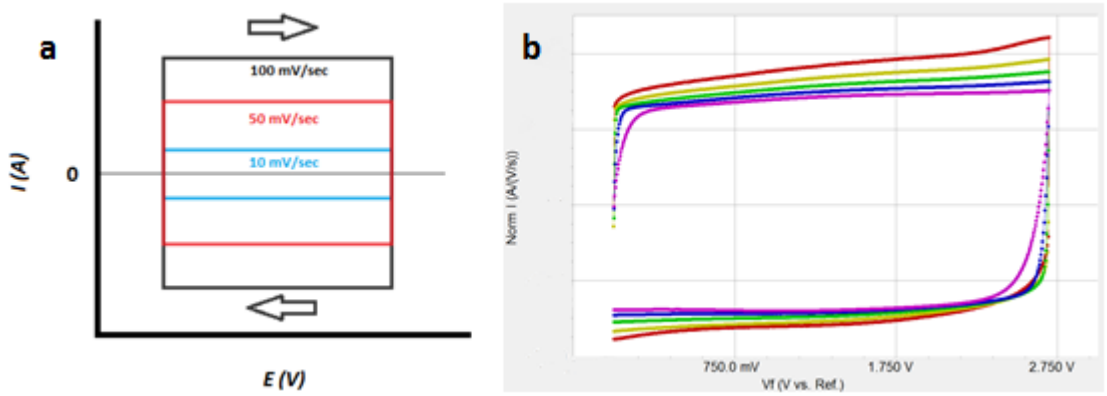

Figure 0.4 ***Theoretical (a) and actual (b) Cyclic Voltammograms for a Supercapacitor device*** **[121].**

Supercapacitors that store energy by the double layer effect tend to demonstrate such a performance and only a slight deviation from the theoretical graphs is observed (Figure 5.b) [121]. This small distortion from the rectangular shape is addressed to diffusion resistances in the initial charging and discharging process of the electrochemical double layer. In the case of a pseudo-capacitor such a performance is not expected, as the specific faradaic reactions are depicted by peaks of current due to reversible redox reactions.

In favor of capacitance (C) determination, Eq. 5.2 is employed:

$$C = \frac{\int i}{\Delta V * \frac{dV}{dt}} dV \qquad [5.2]$$

Where: ΔV is the voltage window and $\frac{dV}{dt}$ is the scan rate.

It should be noted that Eq. 5.2 provides the capacitance value for the whole electrochemical cell. In order to shift from this value to the specific capacitance provided by each electrode, Eq. 5.3 is introduced.

$$Csp = 4C/m \qquad [5.3]$$

Where: m is the mass of the total active material (in both electrodes) and the factor of 4 is introduced by the assumption of having two capacitors connected in series, each one of which is created on the electrodes' surface by the double layer formation.

A crucial point when performing the CV measurements is that the cell should be exposed to the cycling procedure for a specific number of cycles before any capacitance calculation, allowing at the system to reach its stabilization point. When a cell is cycled for the first time, increased current levels are observed due to reversing polarities [119], which can lead to capacitance miscalculation. The previous is shown on Figure 5.5, where a supercapacitor cell with commercial electrodes based on activated carbon and $TEABF_4$ were subjected to a CV measurement for 100 cycles at a scan rate of 50 mV/sec. Obviously the first cycle gives different result in calculation of the capacitance than the tenth or the hundredth cycle due to higher current values.

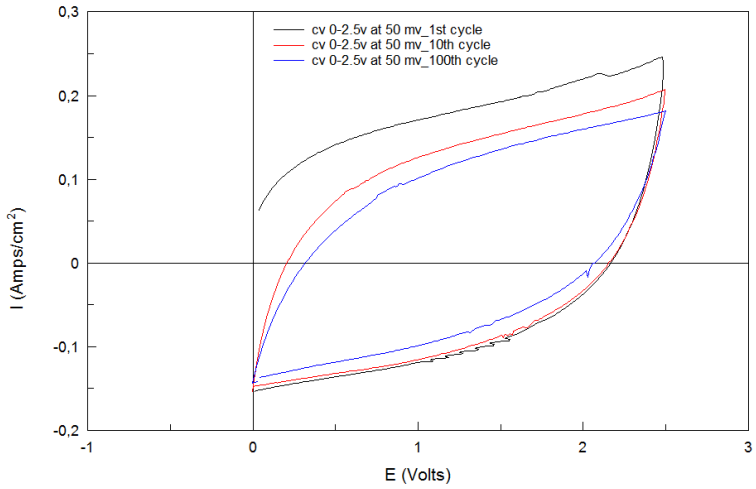

Figure 0.5 ***Cyclic voltammetry curves comparison between the 1st (black), 10th (red) and 100th (blue) cycle of a supercapacitor test cell.***

5.2.2 Capacitance performance by Galvanostatic charge-discharge (CD)

Despite that cyclic voltammetry provides a facile and relatively fast way for determining a cell's capacitance performance, galvanostatic charge and discharge is the accepted method from the supercapacitor and battery industry. That's because CD measurements express the circumstance of a supercapacitor acting as a power source to an external electrical load. Since constant currents are used in CD tests, the capacitance value is calculated by the Eq. 5.1.

Practically, this procedure involves the charging and subsequently discharging the electro-active material at constant current. So, an ideal supercapacitor electrode should be described by a constant linear potential increase and decrease (Eq. 5.1). The capacitance is calculated by the slope of the discharge curve. At the beginning of the discharge a sudden IR (vertical) drop in the voltage is frequently observed. This IR drop is called equivalent series resistance (ESR) of the cell and it represents the sum of the resistances attributed to the current collectors, electrode materials, electrolyte and the external connections (leads) of the setup.

Constrained by the electrolyte's dissociation voltage, any measurement should be performed within the specific electrochemical window mentioned earlier. Driving a cell over its maximum operating range can

mislead the capacitance calculation, giving an overestimated value. Stoller et al. reported significant errors in capacitance calculation could be introduced by the method used to fit the discharge slope (dV/dt). As stated [119], the capacitance varies with voltage, so it is important to calculate the capacitance using the voltage range of the application that the device will be used. Most of supercapacitors will be used from their full charge at V_{max} to the half of this value, ½ V_{max}. In this case, these two values can be used for fitting the curve which allows the capacitance determination. Additionally, low charge rates can also lead to large errors. For comparison purposes the charge rates are always measured in gravimetric current densities and the duration of the charge and discharge should match with the ones in typical supercapacitor applications.

5.2.3 Energy and Power density

Supercapacitors are devices which are mainly designed to be utilized in applications with high load requirements in short time intervals, due to their high power capabilities. Therefore the accurate evaluation of energy and power density provided by the capacitor is necessary for any relevant application. Opposing to batteries and fuel cells which are high energy density devices, supercapacitors are characterized as high power density devices. For proper comparison purposes between cells of different materials, gravimetric specific energy and specific power values are introduced. The specific energy density (Wh/Kg) gives the energy storage capacity of the device per unit mass, whereas the specific power density (W/Kg) denotes the rate at which the stored energy can be delivered, per unit mass. Should these two values be plotted together they yield to the Ragone plot which is often used to compare the respective performance of different electrochemical storage devices. As seen from Figure 5 for both supercapacitors and batteries, there is a tendency in a converse shift between the specific energy and power density. Particularly, an increase in the specific energy returns a decrease in specific power. As higher power requires higher currents densities, higher polarization losses are experienced. Eventually a reduction in the cell's voltage is observed. On the other hand, for low specific power the previous mechanism works towards the opposite direction.

The theoretical maximum stored energy in a device is given by the Gibbs energy required to develop an electrostatic charge. According to Eq. 5.4, the charge stored in a capacitor is given by its capacitance multiplied by the operating voltage. The equation which leads to the energy stored in any capacitor is the Eq. 5.5.

$$C = q/V \qquad [5.4]$$

$$Esp = \frac{1}{2}qV = \frac{1}{2}CV^2 \qquad [5.5]$$

From Eq. 5.5 it is clearly understood why in commercial supercapacitor devices with higher energy densities, organic based electrolytes are preferred (organic based electrolytes operate at 2.7V). Nonetheless

care must be taken when using such a device as only one part of the total energy described by Eq. 5.5 would be available for use. The rest is addressed to the IR drop due to ESR which was described before.

Energy's competitor on Ragone plot, the power density, defines the energy supply rate over time delivered by the device. The power density is mainly restricted by the resistances of the whole electrochemical cell. A simple modeling in a real supercapacitor device [122] is given by a capacitance in serial connection with a resistance. The capacitance represents the charge in storage and the resistance the ESR as seen in Figure 5.6.

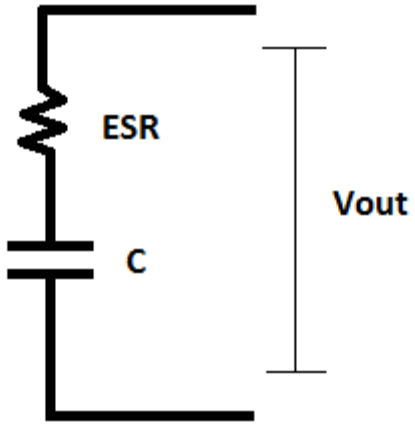

Figure 0.6 ***Simplified equivalent circuit of a real EDLC supercapacitor device.***

A simple electrical circuit analysis reveals that the maximum power available in a supercapacitor cell is mainly defined by its ESR and is given by the equation 5.6. The research of new EC electrode materials should involve the decrease of the respective ESR, as well.

$$P = \frac{V^2}{4\,ESR} \qquad [5.6]$$

The ratio between the energy and power density performance (Dt) provides the rate of discharge of the capacitor and is independent of any factors detrimental to both the power and energy densities and is given by Eq. 5.7.

$$Dt = \frac{Esp}{Psp} \qquad [5.7]$$

The electrochemical performance of the fabricated electrodes, mounted in a full cell (Fig. 5.2) was evaluated by means of cyclic voltammetry (CV) and constant-current charge/discharge measurements (CD) with an AMEL 500 potentiostat (Fig. 2.13) and the results are presented below.

5.3 Graphene based electrodes performance

5.3.1 Graphene nano-platelets

All materials characterized in this sub-section in terms of their electrochemical performance are based on graphene. Three types of stacked multi-layer graphene, 1) GNP (commercial Graphene Nano-Platelets), 2) MnO_2/GNP (Manganese functionalized GNP) and 3) eGNP (electrochemically exfoliated GNP), were engaged for the fabrication of electrodes in accordance to common industrial practices. Electrode preparation was done in the following manner. The graphene materials (10 w%) were dispersed in 1:1 (w/w) H_2O/2-propanol mix with the help of a rotor/stator homogeniser (Silent Crusher M, Heidolph Instruments) for 20 min at 20000 rpm. Thereafter, pre-prepared poly(vinylidenefluoride-hexafluoropropene) (PVDF-HFP 1% in 2-propanol) was added drop-wise as a binder (10% w/w ratio with respect to the amount of graphene materials) at a homogeniser rotation speed of 26000 rpm. The resulting ink was allowed to homogenise for a further 20 min at 26000 rpm. Once prepared, the inks were coated onto collectors, made of aluminium foil, with the bar-coating technique [123], allowing a wet coating thickness of 300 µm. The coatings were left to dry in air for 60 min at 70˚C before the dried mass loadings of the active electrode material were measured and reported as 1.93, 2.05 and 2.03 mg/cm^2, respectively for GNP, eGNP, MnO_2/GNP. Their thickness was measured by a Veeco dektak micro-profilometer to be around 200µm each. Active material loading should not be confused with the amount of carbonaceous materials. In the case of electrodes prepared with MnO_2/GNP, the mass of the electrode coating is shared between graphene nano-platelets and MnO_2.

The performance of graphene based electrodes was studied in order to determine the potential substitution of activated carbon with graphene based materials for supercapacitor applications. Graphene based electrodes have already proven [124] their value. However even if they offer exceptionally high values for gravimetric specific capacitance (F/g), their usually small mass loadings (<0.1 mg/cm^2) do not permit high actual capacitance values. For this reason, electrodes possessing larger mass loadings (thick electrodes) were prepared and studied to evaluate their capacitance properties in real case circumstances, in which an actual supercapacitor would operate.

Their electrochemical performance in terms of specific capacitance C_{sp}, equivalent series resistance R, specific power P_{sp}, and the specific energy E_{sp}, was evaluated by means of CV measurements at a scan rate of 25 mV/s and the CD graphs obtained at 0.25 A/g. The results of these analyses are summarized in Table 5.1. A column presenting the CV performances measured by a three electrodes cell is also included. The results verify the aforementioned statements in the correlation of two and three electrodes cells.

Table 5. 1 ***Electrochemical performance of the tested electrodes as a function of their active mass loading.***

Sample	Specific capacitance (C_{spec}) [F/g]			ESR	P_{spec}	E_{spec}
	3-ele CV (25 mV/s)	*2-ele CV (25 mV/s)*	*2-ele CD (25 mV/s)*	[Ω]	[kW/kg]	[Wh/kg]

GNP	120	70	61.6	21.5	5.45	13
eGNP	21	5.4	4.5	15.4	1.59	0.94
MnO_2/GNP	49	27.5	21.6	7.8	10.5	4.6

Interpretation of the obtained results requires CV data analysis as a function of the scanning rate ranging from 10 to 100 mV/s. The CV curves corresponding to each type of coating material, after stabilization process of ~60 charging/discharging cycles are depicted in Figure 5.7. A substantial capacitive behaviour was observed for all materials, as an appreciable area was formed between the charging and discharging curves of the CV scans. The almost ideal rectangular shape observed for all electrodes at low scan rates, indicates excellent charge propagation across the electrode's surface. The largest charge storage capability was observed from the electrode made by GNP. This result is in agreement with the specific surface measurements presented in section 4.2. However, the shape of the CV curves for GNP appears more elliptical with increasing scan rates, indicating a slow charging/discharging rate at higher scanning speeds. Such behaviour is attributed to the resistive contribution of the electrodes linked to the electron mobility as the rate in potential gain becomes quicker allowing less surface area to be successfully utilized for EDLC storage. In principle, high scanning rates cause rapid ion movement, which results in charging the external surface of the electrode in a faster rate. Such an action virtually decreases the electrode's available surface area as the double layer is formed only on the outer surface living the inner part inaccessible to the ions. This performance is mainly observed in electrodes exhibiting irregular pore structures and essentially limits the power a supercapacitor is able to deliver.

In Figure 5.8 the decrease in the specific capacitance for each electrode is presented. All three kinds of electrodes demonstrate a decrease in the specific capacitance value. The highest decrease is noticed for the GNP electrode (of about 67%) when shifting from 10 to 100 mV/sec, followed by the one of MnO_2GNP (56.5%) and finally the eGNP (35.5%). The decrease in the specific capacitance over the scan rate follows exactly the opposite pace than the one of specific surface area. The higher the irregularity and complexity in the porous structure, the higher would be the decrease in the specific capacitance. It is quite reasonable as in an electrode of high specific surface area, an available portion is found at the inner porous parts; the blocking of these interior complex porous structures lowers its capacitance properties. Adversely an electrode of low specific surface area lacking the high degree of complexity in its porous tends to sustain its capacitance values by increasing the scan rate.

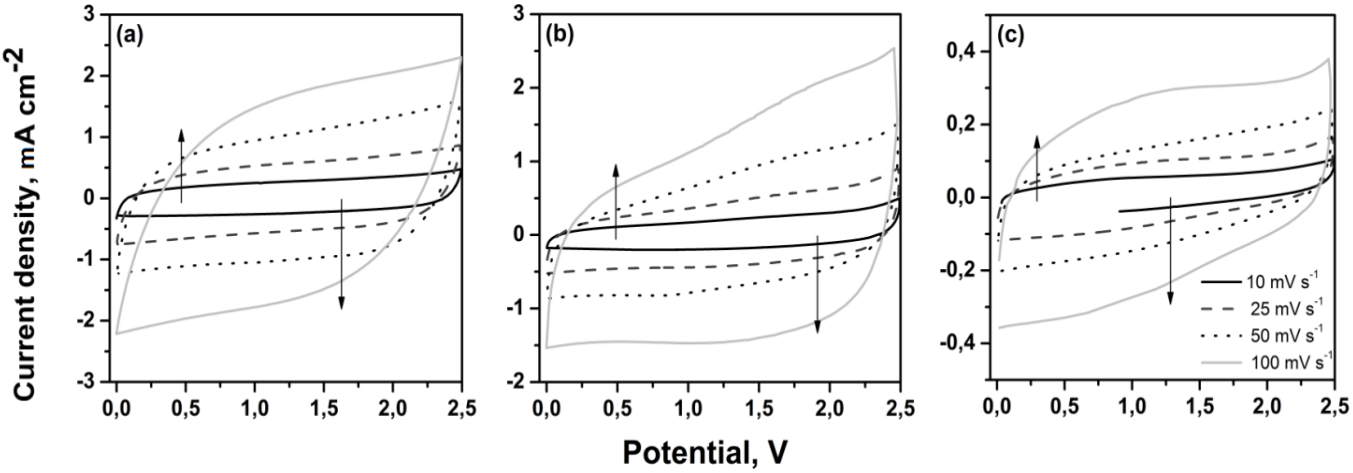

Figure 0.7 ***CV curves at various scan rates for Graphene nano-platelet based electrodes: (a) GNP, (b) MnO_2/GNP and (c) eGNP.***

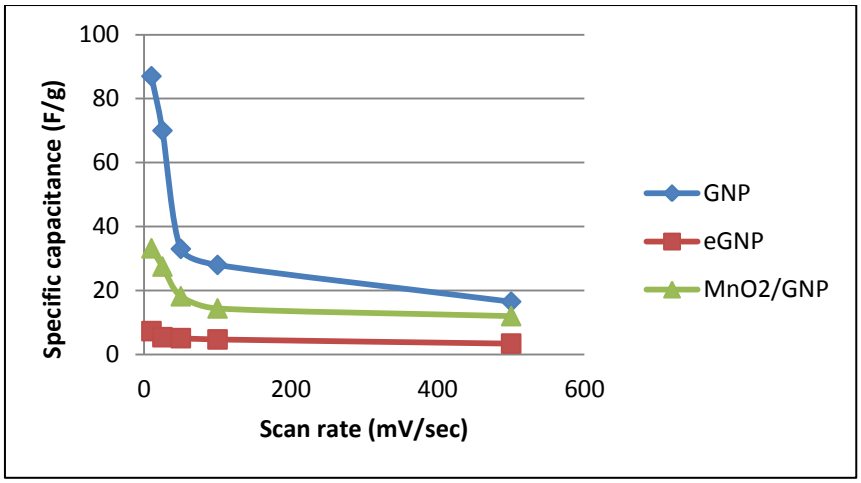

Figure 0.8 ***Specific capacitance in correlation with the scan rate for Graphene nano-platelet based electrodes.***

Yet as revealed in Figure 5.7(c) the eGNP is the less efficient in energy storage as it exhibits the lowest current densities (Eq. 5.2). Its CV response appears to be more rectangular than that of GNP, independently of the scan rate. The lower charge storage capacity for eGNP allows the electrode to reach its saturation current at each respective voltage due to the small change in equilibrium, and thus contributing to a more rectangular CV shape. However, it can be seen that the response of the discharge cycle has a higher gradient than the one during charge, indicating slow discharge rates and a higher resistance respectively.

In case of the electrode based on MnO_2 decorated GNP, Figure 5.7(b), the gradient of the charging cycle is observed to increase with the scan rate while no obvious oxidative peaks have been observed indicating the absence of the intended pseudo-capacitive effects with this aprotic electrolyte. The gentle gradient change detected between 1.2 and 2.2 V can be attributed to the interactions between the MnO_2 particles and the impurities in the electrolyte [125]. The steep initial gradient followed by a much flatter one

during the discharging cycle indicated a low resistance in the release of stored charges. It is acknowledged to MnO_2 nanoparticles presence that act as dividers between the GNP nano-particles and permit the release of the charge in an easy way. By comparing the performance of the electrodes in Figure 5.7(a) and 5.7(b), it is evident that MnO_2 decorated GNP resulted in a relatively lower resistance (steeper discharge slope), while the smaller CV area for the MnO_2/GNP indicated a lower charge storage capability. The lower amount of graphene nanoplatelets in the MnO_2/GNP electrode could have led to this observation.

Constant current charge/discharge tests (CD) were performed to further characterize the electrodes' performance and to determine the R_{ESR} of each capacitor cell. It is known that in CD measurements, the discharge slope indicates the rate at which equilibrium voltages are reached during the constant release of stored charges. Thus, a low slope indicates higher amounts of stored charges and higher capacitance, respectively. As depicted in Figure 5.9, GNP-based electrode exhibited the slowest rate in reaching the determined voltage and the highest specific capacitance, respectively. In terms of resistance, GNP showed the biggest voltage drop at the beginning of the discharge cycle. The R value was observed to increase in the order MnO_2/GNP <eGNP <GNP.

Since the electrochemical results showed lack of redox peaks in the CV curves for GNP and eGNP and linearity of corresponding CD curves, these results point out that the main contribution to the capacitance measured for these graphene nanoplatelet-based electrodes arise from electrochemical double layer effect. In case of MnO_2/GNP, the broad but small oxidative features were only observed in the CV curves but not the CD ones. However, the specific capacitance from both methods was similar, Table 5.1, indicating electrochemical double layer effect to have the main contribution in storing charge.

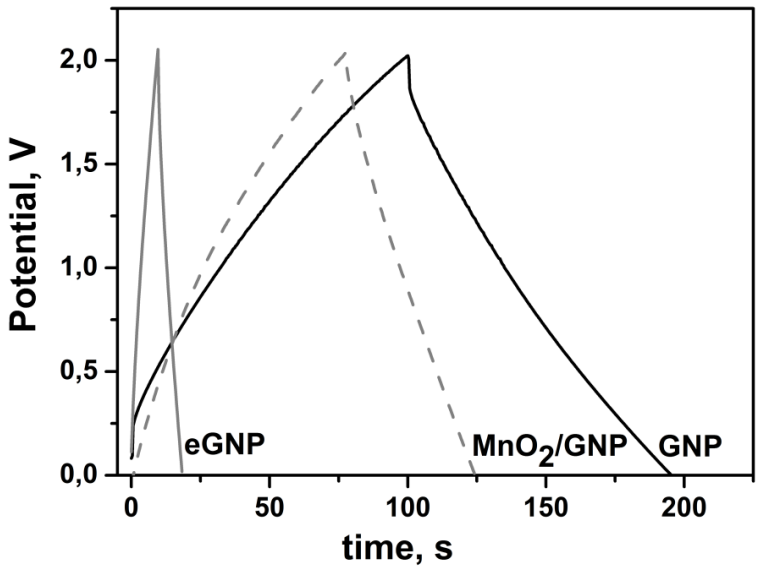

Figure 0.9 ***Galvanostatic charge/discharge (CD) curves for Graphene nano-platelet based electrodes.***

Further, Ragone plots (figure 5.10) for the three graphene based electrodes were plotted from CD measurements, by ranging the current density from 0.25A/g to 1A/g. As shown in Table 5.1, the cell exhibiting higher energy density is the GNP based, arriving close to 13 Wh/Kg at a current density of 0.25 A/g. Additionally, MnO_2/GNP with its low resistance was able to arrive at 6.5 kW/Kg in terms of power density, which is expected for any supercapacitor device, but still exhibits lower energy densities. Finally, eGNP was unable to demonstrate high specific values for energy densities due to really low capacitance properties.

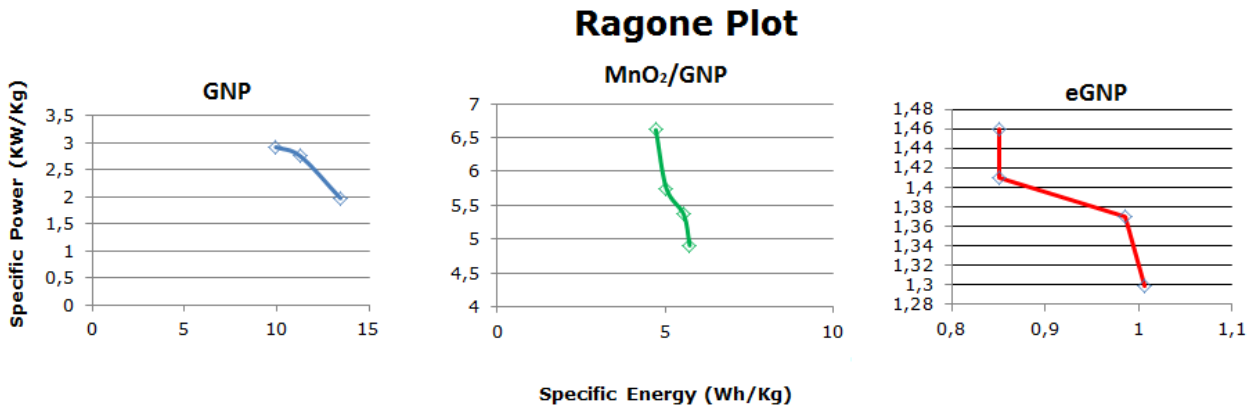

Figure 0.10 ***Ragone plots for Graphene nano-platelet based electrodes.***

In order to assess electrodes' efficiency in charge storage applications with regards to the utilization of the available specific surface (A_{sp}), the specific capacitance determined from the CD curves was compared to the A_{sp} value of the active material for each electrode. The values for this ratio are presented in Figure 5.11.

Although a correlation between high specific surface area and superior capacitance can be identified from the three GNP based samples, the corresponding ratios are not linear. In fact, GNP material that exhibited the highest specific surface area resulted in the lowest utility of the available active surface. By comparing the ratio for GNP and MnO_2/GNP based electrodes, it can be observed that the latter was much more efficient in utilizing the available surfaces. This indicates that the presence of MnO_2 particles in decorated GNP could have enhanced its surface utilization efficiency by facilitating the electrolyte's diffusion by lowering the resistance or ameliorating the electronic network. More significantly, the MnO_2/GNP ink coating contained lower carbonaceous loading than GNP that could allowed a higher percentage of the active material to be exposed to the electrolyte. Conversely, the higher carbonaceous material loading in GNP-based electrode could have led to a poorer electronic network and also higher amounts of unused surface. This finding is also supported by the higher resistance (R) measured for GNP electrode. In spite of the lowest A_{sp} and the low C_{sp}, the eGNP-based electrode exhibited higher C_{sp}/A_{sp} ratio than GNP one. This result could be explained by the larger pore size of the eGNP that increase the accessibility for the ions in the electrolyte. However, considering the high intrinsic resistance of eGNP, inherent from the anodic exfoliation process, the voltage drop across the electrode material could have led to a lower active surface utility compared to MnO2/GNP.

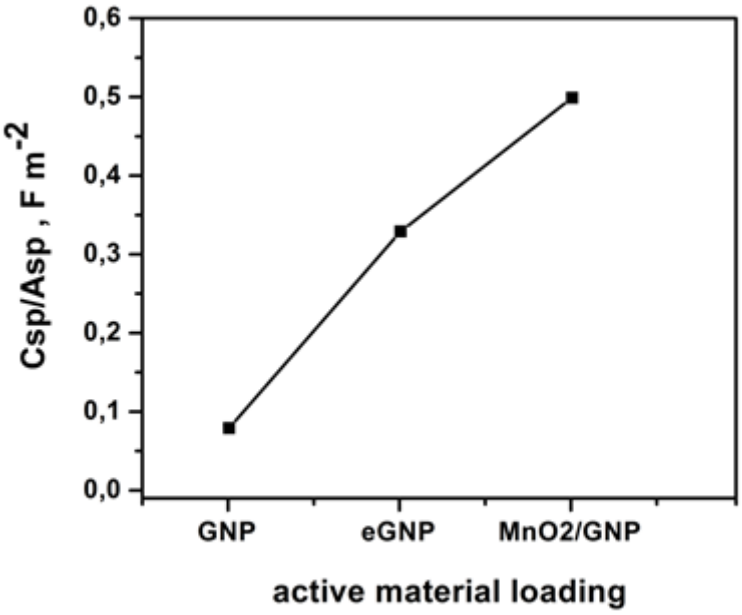

Figure 0.11 ***Surface area utilization ratio in function of active material loading.***

5.3.2 Reduced graphene oxide rGO

In addition to GNPs, reduced graphene oxide was studied for supercapacitor electrode fabrication. The electrodes were made by the same technique described for GNP but in this case rGO powder (described in 4.2.4 section) substituted graphene's platelets. Two separate cases were considered during the electrodes' preparation. The difference between them lies on the addition of carbon black at the second. Consequently, two different electrodes based on the same material were constructed in order to probe their performance for electrochemical charge storage. Herein the rGO based electrode is found as E1, while the rGO + carbon black as E2. Carbon black was introduced as an attempt to increase the overall electrode's conductivity. The active material loading was comparable for these two electrodes as well as their thickness. Table 5.2 presents the material loading for the two aforementioned electrodes.

Table 5. 2 ***Material preparation ratios and mass loadings, measured on dry electrode coatings.***

Electrode type	Electrode material	Preparation ratio (rGO: Binder: Carbon Black)	Active material loading [mg cm^{-2}]
E1	rGO	9:1:0	2.985
E2	rGO	8.5:1:0.5	2.625
Commercial	Activated carbon	9:1:0	7.26

The electrochemical analysis performed in a two electrodes cell, presented in Fig. 5.3. Figures 5.12 (a) and (b) present the CV graphs for these two electrodes. Cyclic voltammetry analysis at multiple scan rates, ranging from 10 to 500 mV/s exhibits fairly rectangular curves for both electrodes. The rectangular-shaped curve observed at 10 mV s^{-1} was maintained even at higher scan rates, indicating excellent charge propagation in the electrodes and electrical double layer capacitor of the electrode material.

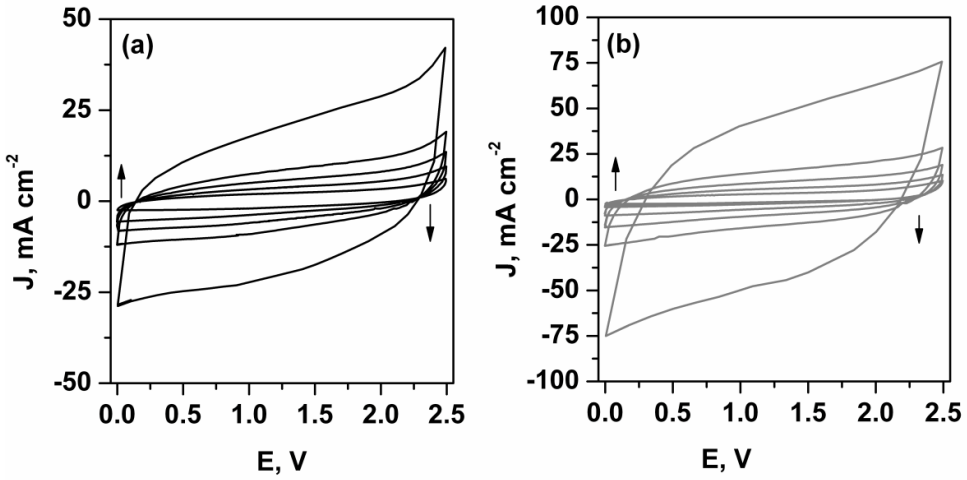

Figure 0.12 ***Cyclic voltammetry graphs for E1 (a) and E2 (b) electrodes.***

From the CV curves in Figure 5.12(a) and 5.12(b), it can be observed that the addition of carbon black in electrode E2 resulted in wider CV loops in comparison to E1 (almost the double), with larger current densities thus indicating higher capacitance values.

The increase in the capacitance suggests that the conductivity of rGO materials increased after embodiment of carbon black along with the electrochemical activity. The introduction of carbon black not only acts as the MnO_2 (spacer) in GNPs but in this case it offers the potential for charge storage and increases the

electrode's overall conductivity. Thus better charge dissipation is expected due to superior electronic network. The inclination in the CV curves with the increase of scan rate indicates the dominance of the double layer formation in the energy storage process at lower scan rates. Besides, the relatively linear increase of the current in all CV curves shows that the charge accumulation is primarily non-faradic in nature [126]. As in the case of GNPs a decrease of the C_{sp} with increasing scan rate was observed. Such a behavior can be accounted to the limited diffusion of electrolyte's ions in shorter time periods when only the outer active surface participates in storing charge.

The main storage properties calculated from CV curves recorded at 25mV/s and CD at a current density of 0.1A/g are presented in Table 5.3. With reference to the electrode, fabricated with commercial activated carbon (120F/g tested in the same conditions), rGO electrodes exhibit quite considerable performance. The potential of rGO upon the addition of carbon black for supercapacitor application was confirmed by the superiority in terms of specific capacitance and energy values in comparison with the bare rGO.

To further evaluate the electrochemical performance of the rGO electrodes, galvanostatic charge-discharge curves were measured at different current densities. The values obtained at 0.1 and 0.25 A/g, respectively, are depicted for exemplification in Figure 5.13. The electrode E1 presented for both current densities an approximately linear triangular shape of the variation of voltage as a function of time during charge and discharge, as expected from a double-layer capacitor [127]. Nonetheless, the deviation from the triangular shape increased for electrode E2 and with the increase in current density. Thus, the slight curvature visible in the charging curve and partially visible in the discharge curves confirmed the contribution of the carbon black to the capacitive behaviour. In the same time, the electrode E2 showed significantly higher charge and discharge times, due to the participation of a higher number of electrons and electrolyte ions in the charge and discharge processes with respect to the electrode E1.

It is known that intercalation depends on the chemical affinity of electrode materials to the ions adsorbed on the electrode surface as well as on the structure and dimension of the electrode pores. The decoration with carbon black particles resulted in a synergistic effect towards the spacing of rGO sheets as demonstrated by the increased porous morphology of the coating E2 in the SEM measurements. This effect led to a tailoring of the pores in the electrode coating that improved electrolyte accessibility as well as electrode conductivity, in agreement with earlier findings in [118].

Table 5. 3 ***Supercapacitor cell parameters as measured from CV curves recorded at 25 mV/s and CD curves at 0.1 A/g respectively*****.**

Electrode type	CV		CD			
	C_{sp} F g-1	*E*sp Wh Kg^{-1}	C_{sp} F g-1	P_{sp} kW Kg^{-1}	E_{sp} Wh Kg^{-1}	*ESR* Ω
E1	30	6.32	19.12	9	4.5	7.16
E2	50.2	10.5	29	10	6.1	7.2

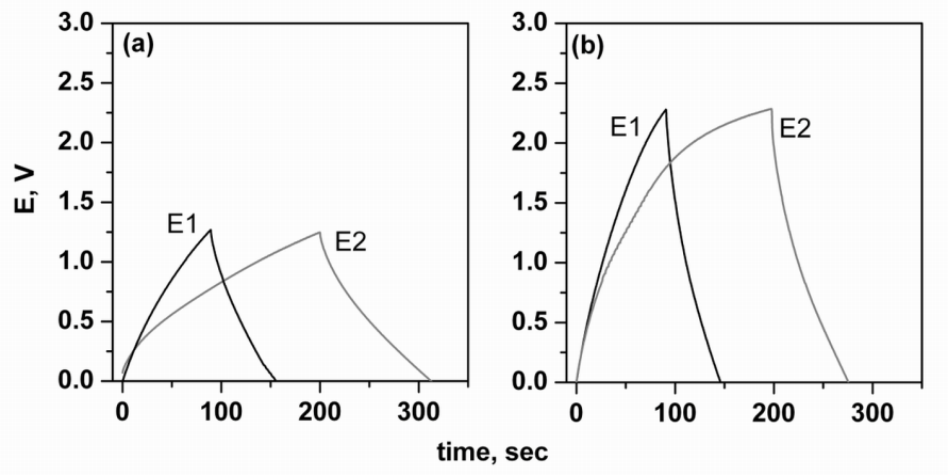

Figure 0.13 ***Galvanostatic charge/discharge (CD) plots for rGO-based electrodes at 0.1 A/g (a) and 0.25 A/g (b) per g of active loading.***

The calculated *ESR* values are presented in Table 5.3 and clearly indicate that, although being fairly large due to the resistance of rGO, the rGO electrodes possessed lower value than the commercial activated carbon. These *ESR* values are comparable with the results of other researchers reporting values ranging from 9.7 to 16.7 Ohm for carbon electrodes derived from activated carbon powder [128].

The decrease in capacitance that was observed with the increase in current density (lower discharge slope in Figure 5.13(a) may be attributed to the low penetration of the ions into the inner region of pores due to fast potential changes. The capacitance values presented in Table 5.3 follow the trend of the values obtained from CV curves, where the rGO with carbon black electrodes exhibited better performance from the plain rGO one and approached the one offered by the activated carbons. The capacitance for rGO electrode is ascribed to the residual oxygen species in rGO that acts as spacers, thus generating extra capacitance [129].

Conclusion

This study has been performed on Energy harvesting from waste by means of piezoelectric nano-generators and energy storage by means of supercapacitors. Both represent two of the main challenges in green energy research today. After having reviewed solar and thermal energies which are found among the most prominent ways of harvesting energy from the ambient, here it is proposed an emerging technology that can be used in converting vibrational mechanical energy to electrical. This kind of application could be employed in modern indoor manufacturing sites, where no sun or wind can arrive and the vibrations are abundant, in order to recover some parts of the energy that usually goes to waste. The abovementioned transformation was done by means of piezoelectric nano-materials.

Overall, it was described the synthesis of piezoelectric ZnO nano-structures in form of thin films, NR and NW. For the growth of ZnO thin films physical vapour deposition techniques have been employed. ZnO NRs are grown by a highly efficient chemical technique called electrochemical deposition and ZnO nanowires by hydrothermal growth. From all previously mentioned techniques, high quality materials were achieved. The most important growth parameters for every one of the earlier mentioned growth techniques were reviewed and their final impact on the as-grown structure was evaluated. Morphological characterization was done by scanning electron microscopy (SEM), atomic force microscopy (AFM) and transmission electron microscopy (TEM). Further characterization was performed in order to reveal the elemental distribution (EDS) as well as the lattice growth direction (XRD). The successful growth is the main part for conceiving and designing novel ZnO based piezoelectric devices. The plurality in the synthesis methods presented here, combined with the dissimilar physical properties offered by them, provide more possibilities for effective fabrication of piezoelectric energy harvesting devices.

Novel designs and materials for piezoelectric energy harvesting devices offer many potential benefits, but also challenges for testing and characterization. Devices using piezoelectric ceramics have been developed for over 15 years and as such a wide range of in-depth testing procedures have been established. There is therefore a great potential benefit for nanostructured piezoelectric energy harvesting (nano-generators) to draw on these testing techniques. The precise evaluation of energy harvesting performance of these devices implied a well-established technique, which provides reliable and repeatable results. It has been shown [83] that the output measured across a range of resistive loads is essential in order to establish the peak power, according to the optimal power transfer theorem.

As demonstrated from the experiments, the harvested energy from these nanostructured devices can arrive up to 2 $\mu J/cm^2$ for a piezoelectric device based on ZnO NWs at each peak. By proper introduction of power electronic circuits or by scaling up the nano-generator's dimensions, the harvesting of some Joules becomes feasible. However this form of energy would not be suitable for further use if not stored in appropriate devices, converted and delivered in a more exploitable form (DC). Based on this prerequisite, the study of novel conceptual devices for energy storage to be combined with energy harvesters was born.

Habitually this is done by means of batteries, which consist the conventional technology. In this study it is proposed a recent concept of energy storage: the electrochemical supercapacitors. These devices have the advantage of storing the energy in an electrostatic way by forming electrochemical double layers on the surface of high specific area electrodes. Graphene with its high surface area density (2600 m^2/g) and conductivity (10^6 S/cm) is proposed here for a supercapacitor electrode. For evaluating the performance of graphene based materials when used as supercapacitor electrodes, thick electrodes have been prepared following the standard industrial procedures. Electrochemical storage measurements like cyclic voltammetry and charge and discharge, as well as relevant material analysis reveal their performance when used for the aforementioned scope.

A wide range of carbon based materials for potential use in supercapacitor electrodes were investigated. A detailed analysis of the most wanted properties, granting their use in supercapacitor applications were revealed thought a series of tests. Morphological analysis was performed by means of optical and scanning electron microscopies. Structural characterization was done by X-Ray diffraction (XRD) to determine the materials' purity. Nitrogen adsorption/desorption isotherms were analyzed for the determination of available surface areas on GNPs. The study on GO and rGO involved the investigation of thermal behaviour and presence of oxygen functional groups in supercapacitor's operation. For this scope Thermogravimetric analysis was performed on these materials. In general, the presence of several required properties for supercapacitor electrode materials was marked.

In conclusion to this work, a rational and reproducible way for a test cell fabrication, in order to electrochemically characterize the performance of graphene based electrodes for supercapacitor applications was reviewed. These thick electrodes demonstrated a fairly capacitive behavior across a series of tests. Though electrochemical analysis utilizing various techniques an appreciable performance of 70F/g was obtained for electrodes based on graphene nano-platelets while 50F/g for reduced graphene oxide. Both of these values are comparable with the ones offered by the commercially available activated carbon electrodes (120 F/g). The electrolyte used in all experiments was the organic based $TEABF_4$ which offers an operational window of 2.7V.

The platelet form of the graphene was proven to make quite efficient use of the available surface for energy storage when compared with the coconut shell of the activated carbons. Even higher was the efficiency in surface area's utilization when GNPs were decorated with MnO_2. GNPs showed large ion accessibility with improved charge transport kinetics yielding high power and energy densities. On the other hand rGO material exhibited inferior performance compared to GNPs and activated carbon. Yet the addition of carbon black to the rGO based electrode leaded to better storage properties.

In this thesis it was achieved the fabrication, the testing and the evaluation of graphene based electrodes for actual supercapacitor applications. However it must not be neglected the fact that the higher mass loadings on the commercial electrodes will finally give higher capacitances as absolute values. For this reason thick graphene based electrodes were engaged for testing. The results revealed that the proper structure of the electrode material could enhance the storage properties; however careful design is necessary when moving to electrodes of larger mass loadings.

As a final remark it can be pointed out that passing from material itself to a functional device requires a rather intense study of its operating principle. Nano-materials can be fairly employed in electronic devices,

especially in the case of nano-electronic devices. However, the shift from nano to macro-scale devices involves the connection from nano to macro world in a proper manner, which was also one of the most crucial parts in this research. Decisive role has as well, the nano-materials structuring/positioning internally of the device which grants efficient exploitation of their unique properties. Nano-technology offers many unexplored potentials left for us to discover. It is only a matter of us being able to exploit them.

Bibliography

[1] European Commission. Eurostat. [Online]. http://epp.eurostat.ec.europa.eu/statistics_explained/index.php/Consumption_of_energy

[2] IEA Renewable energy working party. (2002) Renewable enrgy into the mainstream. [Online]. http://www.iea.org/

[3] D. Vasic, F. Costa E. Minazara, Piezoelectric Generator Harvesting Bike Vibrations Energy to Supply Portable Devices, March 2008.

[4] P.& Margolis, R.M. Denholm, "Evaluating the limits of solar photovoltaics (PV) in electric power systems utilizing energy storage and other enabling technologies.," *Energy Policy 35*, pp. 4424-4433, 2007.

[5] A., & DeDad, J. Kusko, "Stored energy- Short-term and long-term energy storage methods for stand by electric power systems.," *Industry Applications Magazine, IEEE,* pp. 66-72, 2007.

[6] D. J. Swider, "Compressed air energy storage in an electricity system with significant wind power generation.," *Energy Conversion, IEEE Transactions on, 22(1)*, pp. 95-102, 2007.

[7] U., Felderhoff, M., & Schueth, F. Eberle, "Chemical and physical solutions for hydrogen storage.," *Angewandte Chemie International Edition, 48(36)*, pp. 6608-6630, 2009.

[8] W., & Hassenzahl, W. V. Buckles, "Superconducting magnetic energy storage.," *Power Engineering Review, IEEE, 20(5)*, pp. 16-20, 2000.

[9] Z. L. Wang, "Ten years' venturing in ZnO nanostructures: from discovery to scientific understanding and to technology applications," *Chinese Science Bulletin, vol. 54*, pp. 4021–4034, 2009.

[10] Kathy Lu, "Nanomaterials: Bringing New Excitements to the Energy ," *Annals of Materials Science & Engineering*, p. 2, 2014.

[11] D.F. Crisler, J.J. Cupal, and A.R. Moore, "Dielectric, piezoelectric, and electromechanical coupling constants of zinc oxide crystals.," in *Proceedings of the IEEE* , 1968, pp. 225 - 226.

[12] Y. Qin, C. Xu, Y. Wei, R. Yang, and Z. L. Wang S. Xu, "Self-powered nanowire devices," *Nature Nanotechnology, vol. 5, pp*, pp. 366–373, 2010.

[13] K. Yu, D. Jiang, Z. Zhu, H. Geng, and L. Luo Y. Zhang, "Zinc oxide nanorod and nanowire for humidity sensor.," *Applied Surface Science*, pp. 212–217, 2005.

[14] X.-N. Yan, J. Yin, Y.-Q. Duan, and Z.-H. Yuan L.-J. Bie, "Nanopillar ZnO gas sensor for hydrogen and

ethanol," *Sensors and Actuators B: Chemical*, pp. 604–608, 2007.

[15] T.-J. Hsueh, I.-C. Chen, and B.-R. Huang S.-J. Chang, "Highly sensitive ZnO nanowire CO sensors with the adsorption of Au nanoparticles," *Nanotechnology, vol. 19*, p. 175502, 2008.

[16] B., Lee, C., Ho, G.W., Ong, W.L., Liu, J., Yang, C. Yang, "Modeling and experimental study of a low-frequency-vibration-based power generator using Zno nanowire arrays," *Journal of Microelectromechanical Systems 21 (4)*, pp. 776-778, 2012.

[17] R. Yang, J. Zhou, Y. Qin, C. Xu, Y. Hu, S. Xu Z. L. Wang, "Lateral nanowire/nanobelt based nano-generators, piezotronics and piezo-phototronics," *Materials Science and Engineering R*, vol. 70, no. 320-329, Sep. 2010. [Online].

[18] Z. L., & Song, J. Wang, "Piezoelectric nano-generators based on zinc oxide nanowire arrays.," *Science*, pp. 242-246, 2006.

[19] S. F., Şahin, D., Kompitsas, M., & Çankaya, G. Varol, "The impact of different ZnO growth methods on the electrical and optical properties of a n-ZnO/p-GaN: Mg/c-plane sapphire UV LED.," *RSC Advances, 4(26)*, pp. 13593-13600, 2014.

[20] B. E. Conway, *Electrochemical supercapacitors*. New York: Kluwer academic, 1999.

[21] S. W. Lee and H.R. Byon, P.T. Hammond and Y. Shao-Horn B.M. Gallant, "Nanostructured Carbon-Based Electrodes: Bridging the Gap between Thin-Film Lithium-ion Batteries and Electrochemical Capacitors.," *Energy & Environmental Science, 4 (6)*, pp. 1972-1985, 2011.

[22] Y., Jiang, Z., & Yu, X. Zhang, "Control strategies for battery/supercapacitor hybrid energy storage systems.," *In Energy 2030 Conference, 2008. ENERGY 2008. IEEE*, pp. 1-6, 2008.

[23] H. I. Becker, Low voltage electrolytic capacitor, 1957.

[24] Burt E., and Richard M. Peekema Hart, ELECTROCHEMICAL DOUBLE LAYER CAPACITOR, March 28, 1972.

[25] (2014, March) Wikipedia. [Online]. http://en.wikipedia.org/wiki/Supercapacitor

[26] V. Birss, and J. Wojtowicz B.E. Conway, "The role and utilization of pseudocapacitance for energy storage by supercapacitors," *J. Power Sources, vol. 66*, pp. 1-14, 1997.

[27] E. Gileadi, *Electrode kinetics for chemists, chemical engineers, and materials scientists.* New York: VCH. Publishers, 1993.

[28] G. L., Sierra-Alcazar, H. B., Lee, H. L., & Morris, J. L. Bullard, "Operating principles of the ultracapacitor.," *Magnetics, IEEE Transactions on*, pp. 102-106, 1989.

[29] Q., Tang, J., Ma, J., Zhang, H., Shinya, N., & Qin, L. C. Cheng, "Graphene and carbon nanotube composite electrodes for supercapacitors with ultra-high energy density.," *Physical Chemistry Chemical Physics, 13(39)*, pp. 7615-17624, 2011.

[30] A., Dugas, R., Taberna, P. L., Simon, P., Plee, D., Mastragostino, M., & Passerini, S. Balducci, "High temperature carbon–carbon supercapacitor using ionic liquid as electrolyte.," *Journal of power sources, 165(2)*, pp. 922-927, 2007.

[31] E. Frackowiak, "Supercapacitors based on carbon materials and ionic liquids.," *Journal of the Brazilian Chemical Society, 17(6)*, pp. 1074-1082, 2006.

[32] S. M. Lipka, "Electrochemical capacitors utilizing low surface area carbon fiber.," in *In Battery Conference on Applications and Advances*, 1997, pp. 245-248.

[33] J.Y. Li, and Y.P. Feng H. Pan, "Carbon Nanotubes for Supercapacitor," *Nanoscale Research Letters, vol. 5*, pp. 654-668, 2010.

[34] E., & Beguin, F. Frackowiak, "Carbon materials for the electrochemical storage of energy in capacitors.," *Carbon, 39(6)*, pp. 937-950, 2001.

[35] K Balasubramanian, M Jayalakshmi, "Simple Capacitors to Supercapacitors - An Overview," *Int. J. Electrochem. Sci., 3*, pp. 1196 - 1217, 2008.

[36] A. B., Zhou, M., WANG, X. L., SUN, Z. H., & WANG, Y. Q. YUAN, "Synthesis and characterization of nanostructured manganese dioxide used as positive electrode material for electrochemical capacitor with lithium hydroxide electrolyte.," *Chinese Journal of Chemistry, 26(1)*, pp. 65-69, 2008.

[37] A. F. Burke, "Batteries and ultracapacitors for electric, hybrid, and fuel cell vehicles.," *Proceedings of the IEEE, 95(4)*, pp. 806-820, 2007.

[38] Somnath Dasa and Sumit Ghosh, "Fabrication of different morphologies of ZnO superstructures in presence of synthesized ethylammonium nitrate (EAN) ionic liquid: synthesis, characterization and analysis," *Dalton Trans. 42*, pp. 1645-1656, 2013.

[39] W., Jeong, M. C., & Myoung, J. M. Lee, "Catalyst-free growth of ZnO nanowires by metal-organic chemical vapour deposition (MOCVD) and thermal evaporation.," *Acta Materialia.*, pp. 3949-3957, 2004.

[40] D., Pruna, A., Zanin, S., & Mataix, D. B. Pullini, "High-efficiency electrodeposition of large scale ZnO nanorod arrays for thin trasparent electrodes.," *Journal of the electrochemical society*, pp. 45-51, 2011.

[41] Y., Li, X., Wang, N., Quan, X., & Chen, Y. Wang, "Controllable synthesis of ZnO nanoflowers and their morphology-dependent photocatalytic activities.," *Separation and Purification Technology*, pp. 727-732, 2008.

[42] C., Gao, P. X., Ding, Y., Wang, Z. L., & Schwen, D. Ronning, "Manganese-doped ZnO nanobelts for spintronics.," *Applied physics letters, 84(5)*, pp. 783-785, 2004.

[43] W. Hirschwald E. Kaldis, "Current Topics in Materials Science vol.7," , 1981, p. 143.

[44] S. Maniv, "Aspects for the design of sputtering systems.," *Vacuum 33.4*, pp. 215-219, 1983.

[45] T., & Kawabata, A. Shiosaki, "Piezoelectric thin films for SAW applications.," *Ferroelectrics, 42(1)*, pp. 219-232, 1982.

[46] B.A. Movchan and A. V. Demchishin, "Investigation of the structure and properties of thick vacuum-deposited films of nickel, titanium, tungsten, alumina and zirconium dioxide.," *Phys. Met. Metallogr*, pp. 653-660, 1969.

[47] J. A. Thornton, "Influence of apparatus geometry and deposition conditions on the structure and topography of thick sputtered coatings.," *Journal of Vacuum Science & Technology, 11(4)*, pp. 666-670, 1974.

[48] A., Branzoi, V., & Branzoi, F. PRUNĂ, "Application of template-based polyaniline nanotubes synthesized in anodic porous alumina.," *Rev. Roum. Chim, 55(4)*, pp. 293-298, 2010.

[49] S., & Lincot, D. Peulon, "Cathodic electrodeposition from aqueous solution of dense or open-structured zinc oxide films.," *Advanced Materials, 8(2)*, pp. 166-170, 1996.

[50] D., & Busquets-Mataix, D. Pullini, "Electrodeposition efficiency of Co and Cu in the fabrication of multilayer nanowires by polymeric track-etched templates.," *ACS applied materials & interfaces, 3(3)*, pp. 759-764, 2011.

[51] Daniele Pullini and David Busquets Mataix Alina Pruna, "Influence of Deposition Potential on Structure of ZnO NanowiresSynthesized in Track-Etched Membranes.," *Journal of The Electrochemical Society, 159 (4)*, 2012.

[52] V. A., Mickan, M., Henry, F., Delamare, R., Gence, L., & Piraux, L. Antohe, "Self-seeded electrochemical growth of ZnO nanorods using textured glass/Al-doped ZnO substrates.," *Applied Surface Science, 313*, pp. 607-614, 2014.

[53] Diamond coatings. [Online]. http://www.diamondcoatings.co.uk/diamox-indium-tin-oxide.html

[54] D., Puippe, J. C., & Leaman, F. Landolt, *Theory and Practice of Pulse Plating.* Orlando: American Electroplaters and Surface Finishers Society, 1986.

[55] Loik Gence, Sandeep Kumar Srivastava and Luc Piraux Vlad Andrei Antohe, "Template-free electrodeposition of highly oriented and aspect-ratio controlled ZnO hexagonal columnar arrays.,"

Nanotechnology 23, p. 255602 (6pp), 2012.

[56] T. Pauporté, "Design of solution-grown ZnO nanostructures," in *In Toward Functional Nanomaterials*.: Springer US, 2009, pp. 77-125.

[57] A., Ribeiro, C., Al-Hajry, A., Masuda, Y., & Hahn, Y. B. Umar, "Growth of highly c-axis-oriented ZnO nanorods on ZnO/glass substrate: growth mechanism, structural, and optical properties. ," *The Journal of Physical Chemistry C, 113(33)*, pp. 14715-14720, 2009.

[58] G. Z., Yi, J. B., Tao, J. G., Liu, T., Wong, L. M., Zhang, Z.,. & Wu, T. Xing, "Comparative Study of Room-Temperature Ferromagnetism in Cu-Doped ZnO Nanowires Enhanced by Structural Inhomogeneity.," *Advanced Materials, 20(18)*, pp. 3521-3527, 2008.

[59] A. Pruna, S. Zanin, and D. Busquets Mataixd D. Pullini, "High-Efficiency Electrodeposition of Large Scale ZnO Nanorod Arrays for Thin Transparent Electrodes.," *Journal of The Electrochemical Society, 159 (2)*, pp. E45-E51, 2012.

[60] C., Capochichi-Gnambodoe, M., & Leprince-Wang, Y. Chevalier-César, "Growth mechanism studies of ZnO nanowire arrays via hydrothermal method.," *Applied Physics A, 115(3)*, pp. 953-960, 2014.

[61] H., Huang, X., Deng, C., Chen, X., & Qian, Y. Hu, "Hydrothermal synthesis of ZnO nanowires and nanobelts on a large scale.," *Materials Chemistry and Physics, 106(1)*, pp. 58-62, 2007.

[62] L. E., Law, M., Goldberger, J., Kim, F., Johnson, J. C., Zhang, Y.,. & Yang, P. Greene, "Low-temperature wafer-scale production of ZnO nanowire arrays.," *Angewandte Chemie International Edition, 42(26)*, pp. 3031-3034, 2003.

[63] S. Baruah and J. Dutta, "Hydrothermal growth of ZnO nanostructures.," *Science and Technology of Advanced Materials*, p. 013001, 2009.

[64] R. Doherty, N. Ndiforangwafor, D. Riley, and Y. Sun M. Ashfold, "The kinetics of the hydrothermal growth of ZnO nanostructures.," *Thin Solid Films vol. 515*, pp. 8679–8683, 2007.

[65] C. Lin and Y. Li, "Synthesis of ZnO nanowires by thermal decomposition of zinc acetate dihydrate.," *Materials Chemistry and Physics, vol. 113*, pp. 334–337, 2009.

[66] Jaejin Song and Sangwoo Lim, "Effect of Seed Layer on the Growth of ZnO Nanorods," *J. Phys. Chem. C, 111 (2)*, pp. 596–600, 2007.

[67] S. Jesse. Oak Ridge National Laboratory. [Online]. http://www.ornl.gov/

[68] A. L., Pertsev, N. A., & Goltsev, A. V. Kholkin, "Piezoelectricity and crystal symmetry.," in *Piezoelectric and Acoustic Materials for Transducer Applications.*: Springer US, 2008, pp. 17-38.

[69] S., Stewart, M., & Cain, M. G. Lepadatu, "Quantification of electromechanical coupling measured with piezoresponse force microscopy.," *Journal of Applied Physics, 116(6)*, 2014.

[70] N. W. Emanetoglu and Y. Chen. Y. Lu, " ," in *ZnO bulk, thin films and nanostructures*. Oxford: Elsevier, 2006, pp. 443-490.

[71] K., & Dormans, G. J. M. Lefki, "Measurement of piezoelectric coefficients of ferroelectric thin films.," *Journal of applied physics, 76(3)*, pp. 1764-1767, 1994.

[72] S. Lepadatu and M. Cain M. Stewart, *Appl. Phys. Lett.*, In press 2014.

[73] H., & Berlincourt, D. A. Jaffe, "Piezoelectric transducer materials.," *Proceedings of the IEEE, 53(10)*, pp. 1372-1386, 1965.

[74] K. K., Cicero, G., & Catellani, A. Korir, "Piezoelectric properties of zinc oxide nanowires: an ab initio study.," *Nanotechnology*, p. 475401, 2013.

[75] H. J., Yang, J., Hou, J. G., & Zhu, Q. Xiang, "Piezoelectricity in ZnO nanowires: A first-principles study.," *Applied physics letters, 89(22)*, pp. 223111-223111, 2006.

[76] E., Soomro, M. Y., Lu, J., Willander, M., & Hultman, L. Broitman, "Nanoscale piezoelectric response of ZnO nanowires measured using a nanoindentation technique.," *Physical Chemistry Chemical Physics, 15(26)*, pp. 11113-11118, 2013.

[77] S., Baddorf, A. P., & Kalinin, S. V. (2006). Jesse, "Switching spectroscopy piezoresponse force microscopy of ferroelectric materials.," *Applied physics letters, 88(6)*, p. 062908, 2006.

[78] M. H., Wang, Z. L., & Mao, S. X. Zhao, "Piezoelectric characterization of individual zinc oxide nanobelt probed by piezoresponse force microscope.," *Nano Letters, 4(4)*, pp. 587-590, 2004.

[79] A. L., Wütchrich, C., Taylor, D. V., & Setter, N. Kholkin, "Interferometric measurements of electric field-induced displacements in piezoelectric thin films.," *Review of scientific instruments, 67(5)*, pp. 1935-1941, 1996.

[80] D. A., Sounart, T. L., Simmons, N. C., & Hsu, J. W. Scrymgeour, "Polarity and piezoelectric response of solution grown zinc oxide nanocrystals on silver.," *Journal of applied physics, 101(1)*, p. 014316, 2007.

[81] H. J., Lee, W., Hauschild, R., Alexe, M., Le Rhun, G., Scholz, R.,. & Gösele, U. Fan, "Template-Assisted Large-Scale Ordered Arrays of ZnO Pillars for Optical and Piezoelectric Applications.," *Small*, pp. 561-568, 2006.

[82] Ronan, et al. Hinchet, "Performance Optimization of Vertical Nanowire-based Piezoelectric Nano-generators.," *Advanced Functional Materials 24.7* , pp. 971-977, 2014.

[83] J., Stewart, M., Vopson, M., Cain, M., Weaver, P. M., & Dunn, S. Briscoe, "Nanostructured p-n Junctions for Kinetic-to-Electrical Energy Conversion.," *Advanced Energy Materials, 2(10)*, pp. 1261-1268, 2012.

[84] P., & Batra, I. P. Wurfel, "Depolarization-field-induced instability in thin ferroelectric films—experiment and theory.," *Physical Review B, 8(11)*, p. 5126, 1973.

[85] Florian Auras, Paolo Motto, Stefano Stassi, Giancarlo Canavese, Edvige Celasco, Thomas Bein, Barbara Onida and Valentina Cauda Vivian Farias Rivera, "Length-Dependent Charge Generation from Vertical Arrays of High-Aspect-Ratio ZnO Nanowires," *Chem. Eur. J.*, pp. 14665 – 14674, 2013.

[86] J., Yushin, G., Dash, R., & Gogotsi, Y. Chmiola, "Effect of pore size and surface area of carbide derived carbons on specific capacitance.," *Journal of Power Sources, 158(1)*, pp. 765-772, 2006.

[87] E Frackowiak, "Carbon materials for supercapacitor application," *Physical Chemistry Chemical Physics, 9(15)*, pp. 1774-1785, 2007.

[88] M. J., Tung, V. C., & Kaner, R. B. Allen, "Honeycomb carbon: a review of graphene.," *Chemical reviews, 110(1)*, pp. 132-145, 2009.

[89] J., Llaguno, M. C., Nemes, N. M., Johnson, A. T., Fischer, J. E., Walters, D. A.,. & Smalley, R. E. Hone, "Electrical and thermal transport properties of magnetically aligned single wall carbon nanotube films.," *Applied Physics Letters, 77(5)*, pp. 666-668, 2000.

[90] A., Laurent, C., Flahaut, E., Bacsa, R. R., & Rousset, A. Peigney, "Specific surface area of carbon nanotubes and bundles of carbon nanotubes.," *Carbon, 39(4)*, pp. 507-514, 2001.

[91] M., Šmíd, B., & Veltruská, K. Pumera, "Influence of nitric acid treatment of carbon nanotubes on their physico-chemical properties.," *Journal of nanoscience and nanotechnology, 9(4)*, pp. 2671-2676, 2009.

[92] E. K. Sichel, R. Hoch, D. Moy, H. Tennent C. Niu, "High power electrochemical capacitors based on carbon nanotube electrodes.," *Appl. Phys. Lett., 70 (11)*, pp. 1480-1482, 1997.

[93] W. S. Kim, Y. S. Park, J.-M. Moon, D. J. Bae, S. C. Lim, Y. S. Lee, Y. H. Lee K. H. An, "Electrochemical Properties of High-Power Supercapacitors Using Single-Walled Carbon Nanotube Electrodes.," *Adv. Funct. Mater., 11 (5)*, pp. 387-392, 2001.

[94] A. Patil, X. Gong, Z. Guo, L. Liu, Y. Liu, D. Zhu L. Dai, "Aligned Nanotubes.," *ChemPhysChem, 4 (11)*, pp. 1150-1169, 2003.

[95] L. L., & Zhao, X. S. Zhang, "Carbon-based materials as supercapacitor electrodes.," *Chemical Society Reviews, 38(9)*, pp. 2520-2531, 2009.

[96] Y., Zhang, X., Zhang, D., Yu, P., & Ma, Y. Chen, "High performance supercapacitors based on reduced

graphene oxide in aqueous and ionic liquid electrolytes.," *Carbon, 49(2)*, pp. 573-580, 2011.

[97] M. D., Park, S., Zhu, Y., An, J., & Ruoff, R. S. Stoller, "Graphene-based ultracapacitors.," *Nano letters, 8(10)*, pp. 3498-3502, 2008.

[98] J. H., Jang, C., Adam, S., Fuhrer, M. S., Williams, E. D., & Ishigami, M. Chen, "Charged-impurity scattering in graphene.," *Nature Physics, 4(5)*, pp. 377-381, 2008.

[99] C., Wei, X., Kysar, J. W., & Hone, J. Lee, "Measurement of the elastic properties and intrinsic strength of monolayer graphene.," *Science, 321(5887)*, pp. 385-388, 2008.

[100] XG Sciences. [Online]. http://xgsciences.com/wp-content/uploads/2012/10/10-15-13_xGnP-C_Data-Sheet.pdf

[101] F., & Koenig, J. L. Tuinstra, "Raman spectrum of graphite.," *The Journal of Chemical Physics, 53(3)*, pp. 1126-1130, 1970.

[102] F., & Centeno, T. A. Stoeckli, "On the determination of surface areas in activated carbons. ," *Carbon, 43(6)*, pp. 1184-1190, 2005.

[103] A. Sy, A. Davies. A. Yu, "Graphene nanoplatelets supported MnO2 nanoparticles for electrochemical supercapacitor.," *Synth. Met. 161*, pp. 2049-2054, 2011.

[104] M. Matis, U. Kosidlo, F. Tonner, C. Glanz, and I. Kolaric, *Graphite, Graphene and Their Polymer Nanocomposites*. Florida; New York; Oxfordshire: CRC Press, 2013, pp. 139-168.

[105] A. C. Ferrari et al., *Physical Review Letters*, vol. 97, pp. 187401(1) -187401(4), 2006.

[106] A. Kaniyoor and S. Ramaprabhu, *AIP Advances*, vol. 2, pp. 032183(1) - 032183(13), 2012.

[107] O., & Ghaderi, E. Akhavan, "Escherichia coli: bacteria reduce graphene oxide to bactericidal graphene in a self-limiting manner.," *Carbon 50(5)*, pp. 1853-1860, 2012.

[108] H., Zhao, W., Hu, H., & Chen, G. Wu, "One-step in situ ball milling synthesis of polymer-functionalized graphene nanocomposites.," *Journal of Materials Chemistry 21(24)*, pp. 8626-8632, 2011.

[109] X., & Ouyang, J. Mei, "Ultrasonication-assisted ultrafast reduction of graphene oxide by zinc powder at room temperature.," *Carbon, 49(15)*, pp. 5389-5397., 2011.

[110] S., An, J., Jung, I., Piner, R. D., An, S. J., Li, X.,. & Ruoff, R. S. Park, "Colloidal suspensions of highly reduced graphene oxide in a wide variety of organic solvents.," *Nano letters, 9(4)*, pp. 1593-1597, 2009.

[111] Y., Bai, H., Lu, G., Li, C., & Shi, G. Xu, "Flexible graphene films via the filtration of water-soluble noncovalent functionalized graphene sheets.," *Journal of the American Chemical Society, 130(18)*, pp.

5856-5857, 2008.

[112] F., & Seo, T. S. Liu, "A Controllable Self-Assembly Method for Large-Scale Synthesis of Graphene Sponges and Free-Standing Graphene Films.," *Advanced Functional Materials, 20(12)*, pp. 1930-1936, 2010.

[113] D. Q., & Sacher, E. Yang, "Carbon 1s X-ray photoemission line shape analysis of highly oriented pyrolytic graphite: the influence of structural damage on peak asymmetry.," *Langmuir, 22(3)*, pp. 860-862, 2006.

[114] D., Velamakanni, A., Bozoklu, G., Park, S., Stoller, M., Piner, R. D.,. & Ruoff, R. S. Yang, "Chemical analysis of graphene oxide films after heat and chemical treatments by X-ray photoelectron and Micro-Raman spectroscopy.," *Carbon, 47(1)*, pp. 145-152, 2009.

[115] W., Alemany, L. B., Ci, L., & Ajayan, P. M. Gao, "New insights into the structure and reduction of graphite oxide.," *Nature Chemistry, 1(5)*, pp. 403-408, 2009.

[116] D. W., & Katsnelson, M. I. Boukhvalov, "Modeling of graphite oxide.," *Journal of the American Chemical Society, 130(32)*, pp. 10697-10701, 2008.

[117] M. A., Dresselhaus, G., Dresselhaus, M. S., Cancado, L. G., Jorio, A., & Saito, R. Pimenta, "Studying disorder in graphite-based systems by Raman spectroscopy.," *Physical Chemistry Chemical Physics, 9(11)*, pp. 1276-1290, 2007.

[118] T. Wei, B. Shao, F. Ma, Z. Fan, M. Zhang J. Yan, "Electrochemical properties of graphene nanosheet/carbon black composites as electrodes for supercapacitors.," *Carbon, 48(6)*, pp. 1731-1737, 2010.

[119] M. D., & Ruoff, R. S. Stoller, "Best practice methods for determining an electrode material's performance for ultracapacitors.," *Energy & Environmental Science, 3(9)*, pp. 1294-1301, 2010.

[120] Oxford University. Oxford university. [Online]. http://compton.chem.ox.ac.uk/index.php?title=research&topic=fund

[121] Garmy instruments. Garmy instruments. [Online]. http://www.gamry.com/application-notes/testing-electrochemical-capacitors-part-1-cyclic-voltammetry-and-leakage-current/

[122] D. A., & Miller, J. R. Evans, "Hybrid electrolytic/electrochemical capacitor for electric vehicles.," in *In Proceedings of the Symposium on Electrochemical Capacitors*, 1997, pp. 253-257.

[123] www.mtixtl.com. [Online]. http://www.mtixtl.com/LargeAutomaticFilmCoaterwith12Wx24LVacuumChuck-MSK-AFA-II-VC.aspx

[124] A., Roes, I., Davies, A., & Chen, Z. Yu, "Ultrathin, transparent, and flexible graphene films for supercapacitor application.," *Applied physics letters, 96(25)*, p. 253105, 2010.

[125] W., Fan, Z., Gu, L., Bao, X., & Wang, C. Chen, "Enhanced capacitance of manganese oxide via confinement inside carbon nanotubes.," *Chemical Communications, 46(22)*, pp. 3905-3907, 2010.

[126] S., Piner, R. D., Nguyen, S. T., & Ruoff, R. S. Stankovich, "Synthesis and exfoliation of isocyanate-treated graphene oxide nanoplatelets.," *Carbon, 44(15)*, pp. 3342-3347, 2006.

[127] X. Y., Liu, X. X., Diamond, D., & Lau, K. T. Peng, "Synthesis of electrochemically-reduced graphene oxide film with controllable size and thickness and its use in supercapacitor.," *Carbon, 49(11)*, pp. 3488-3496, 2011.

[128] K. M., Hur, J. W., Jung, S. I., & Kang, A. S. Kim, "Electrochemical characteristics of activated carbon/Ppy electrode combined with P (VdF-co-HFP)/PVP for EDLC.," *Electrochimica acta, 50(2)*, pp. 863-872, 2004.

[129] Y., Zhang, X., Zhang, D., Yu, P., & Ma, Y. Chen, "High performance supercapacitors based on reduced graphene oxide in aqueous and ionic liquid electrolytes.," *Carbon, 49(2)*, pp. 573-580, 2011.

Acknowledgements

I would like to thank all the people assisted me to develop my PhD work: first Daniele Pullini and Giancarlo Cicero who have been my supervisors and mentors during my PhD period. I would like to express them my honest thanks for the fruitful discussions we had throughout all these years that assisted me to settle my own research approach.

In addition I would like to thank all scientific staff of Fiat research center, which helped me perform my research in a pleasant and effective atmosphere. Specifically I would like to thank: Valentina Grasso, Antonio Veca, Mauro Sgroi, Brunetto Martorana, Alessandro Ziggioti, Mauro Brignone and Davide Roncato. I would like to give my special thanks to Nello Li Pira and Luca Belforte who have been my laboratory managers and introduced me to all appropriate instrumentation used for my thesis.

Moreover I would like to thank my cousin and close collaborator Dr. Athanasios Tamvakos for his moral support and help in the accomplishment of my doctoral studies. My truthful thanks are addressed also to all other colleagues from CRF with whom I have spent many hours together in the laboratory. I similarly appreciate my colleagues from Nanowiring and Electrograph projects whose ideas helped me in shaping up the research discussion. Many thanks also go to the research stuff of NPL (National Physical Laboratory), IIT (Italian Institute of Technology), Fraunhofer IPA, and UCL (Catholic University of Louvain) for their crucial participation in my research project. Distinct thanks to Dr. Alina Pruna for her supervision and her guidance as Post-doc.

Last but not least I would like to thank my family for their aid and support during all periods of my life and all of my friends that stand always by my side.